DESIGN OF HYBRID (DE)MULTIPLEXERS FOR OPTICAL INTERCONNECTS ON SOI PLATFORM

A

Thesis submitted

in partial fulfilment of the requirements

for the dual degree of

Master of Science (Eng.) and Doctor of Philosophy

by

Manoranjan Minz

Department of Electronics and Electrical Engineering
Indian Institute of Technology Guwahati
Guwahati - 781039, Assam, India
November 2021

Dedicated to

My Beloved Parents

Mrs. Fagni Minz & Mr. Baiju Minz

My Teachers, Friends

and

My Loving Wife

Mrs. Prerana Priyadarshini Minz

Certificate

This is to certify that the thesis entitled “**Design of hybrid (de)multiplexers for optical interconnects on SOI Platform**", submitted by **Manoranjan Minz** (Registration Number: 156302009), a research scholar in the *Department of Electronics and Electrical Engineering, Indian Institute of Technology Guwahati*, for the award of the dual degree of **Master of Science (Eng.) and Doctor of Philosophy**, is a record of an original research work carried out by him under my supervision and guidance. The thesis has fulfilled all requirements as per the regulations of the institute and in my opinion has reached the standard needed for submission. The results embodied in this thesis have not been submitted to any other University or Institute for the award of any degree or diploma.

Date:

Place: Guwahati

Dr. Ramesh Kumar Sonkar
Associate Professor
Dept. of Electronics and Electrical Engg.
Indian Institute of Technology Guwahati
Guwahati - 781039, Assam, India.


भारतीय प्रौद्योगिकी संस्थान गुवाहाटी
Indian Institute of Technology Guwahati

Acknowledgements

First and foremost, I would like to extend my deepest and most sincere gratitude to my supervisor Dr. Ramesh Kumar Sonkar, for the continuous support during my Ph.D. research, for his patience, motivation, enthusiasm, and guidance. His kindness, dedication, hard work, and attention to detail helped me enormously in publishing research papers as well as writing of this thesis. I could not have imagined having a better advisor and mentor for my Ph.D. study. Besides my supervisor, I am also thankful to my doctoral committee members Prof. Rakhesh Singh Kshetrimayum, Dr. Tamarapalli Venkatesh, and Dr. Arun Tej Mallajosyula for their encouragement, suggestions, and valuable feedback.

My sincere thanks also go to the Head of the Department and other faculty members including all the members of the research and technical staff of the department for providing all the necessary facilities to carry out the research work. I thank my fellow labmates Dr. Darpan Mishra, Dr. Jitendra Prajapati, Dr. Niladri Das, Dr. Dibyajyoti Das, Dr. Dhiman Kakati, Dr. Mrinmoy Bhardwaj, Dr. Gaurav Kumar Bharti, Aruna, Mansoor Sir, Manish, Sumanth, Manish Gour, and Aayushi for maintaining a suitable research atmosphere in the lab. I would also like to thank my friends Darpan, Bikash, Chandan, Prabhakar, Vineeta, Atanu, Birjit, Mohit, Rahul, Satyajit, and Pralay for making my stay in the campus joyous and playful. I express gratitude to all the members of Research Scholar Forum EEE (2017-18 and 2018-19) and SPIE IIT Guwahati Student Chapter (2017-18) which I was a part of.

I extend my utmost gratitude to my parents and my wife for supporting me in every step of this journey and bearing all the pain which may have ensued due to my prolonged absence. This thesis would not have been completed without their love, support, and blessings. It is impossible for me to address every individual who has helped me directly or indirectly during my Ph.D., and for that, I apologize.

Manoranjan Minz

(Manoranjan Minz)

Abstract

The ever increasing data traffic due to technological advancements as well as increase in the number of users has ignited tremendous interest in the research and development of high performing computing systems. However, the performance increase is limited by the usage of electrical interconnects, as it suffers from high power dissipation and propagation delay. To overcome these issues optical interconnect has emerged as a viable solution owing to its low power consumption and potential for link capacity improvement by employing various multiplexing techniques such as wavelength division multiplexing (WDM), polarization division multiplexing (PDM), and mode-division multiplexing (MDM). Silicon photonics platform has attracted a lot of attention as it has enabled monolithic integration of photonics and microelectronics due to its compatibility with the standard complementary metal oxide semiconductor technology. Considering the demands of high-link capacity in the future, research is in progress to combine multiple multiplexing schemes to realize a multi-dimensional hybrid multiplexing technology. This thesis explores the design of such hybrid (de)multiplexers, which are based on the contra-directional coupling principle using periodic grating structures. To the best of our knowledge, for the first time, a grating assisted collaterally contra-directional coupled TE and TM MDMs are introduced using silicon slab waveguides. Then by cascading the TE and TM MDMs, a hybrid MDM-PDM device has been reported on silicon-on-insulator platform. The theory of supermodes has been utilized to determine a suitable gap between the waveguides such that contra-directional coupling occurs with low reflection at the input. Mathematical models of the proposed devices are presented with coupled-mode equations and their solutions. A hybrid MDM-WDM device is demonstrated using the buried strip waveguides and silicon grating structures by integrating the wavelength and mode division multiplexing schemes. To further increase the link capacity, PDM is combined with the MDM-WDM structure to realize a hybrid MDM-PDM-WDM device. The devices are designed and analyzed using the numerical finite-difference time-domain method.

Contents

List of Figures

List of Tables

List of Acronyms

ADC	Asymmetric Directional Coupler
AWG	Arrayed Waveguide Grating
CMOS	Complementary Metal-Oxide-Semiconductor
CT	Crosstalk
CWDM	Coarse Wavelength Division Multiplexing
DC	Directional Coupler
DEMUX	Demultiplexer
DPWA	Densely Packed Waveguide Arrays
DWDM	Dense Wavelength Division Multiplexing
EIM	Effective Index Method
ENIAC	Electronic Numerical Integrator And Computer
FDTD	Finite-Difference Time-Domain
FPR	Free Propagation Region
GAC	Grating Assisted Coupler
IL	Insertion Loss
MDM	Mode-division Multiplexing
MMI	Multimode Interferometer
MRM	Microring Modulator
MRR	Microring Resonator
MUX	Multiplexer
MZI	Mach-Zehnder Interferometer
PBS	Polarization Beam Splitter

PDM	Polarization-division Multiplexing
PML	Perfectly Matched Layer
PR	Polarization Rotator
RL	Return Loss
SOI	Silicon-on-Insulator
SWG	Subwavelength Grating
TE	Transverse Electric
TM	Transverse Magnetic
WDM	Wavelength-division Multiplexing

List of Symbols

β	Propagation Constant
E	Electric Field
H	Magnetic Field
ω	Optical Frequency
Λ	Grating Period
κ	Coupling Coefficient
Δn^2	Dielectric Profile
λ	Wavelength of Light
n	Refractive Index
n_{eff}	Effective Index
R	Radius of Microring Resonator
w	Width of the Waveguide
N_Λ	Number of Grating Periods
L	Device Length
n_{core}	Core Refractive Index
n_{clad}	Cladding Refractive Index
Ψ	Cross-sectional Field Profile

List of Publications

Journal Publications

1. **Manoranjan Minz** and Ramesh Kumar Sonkar, “Design of a hybrid silicon mode, polarization, and wavelength division (de)multiplexer on SOI platform,” *IEEE Photonics Technology Letters*. **(submitted)**
2. Darpan Mishra, **Manoranjan Minz**, and Ramesh Kumar Sonkar, “A compact three-mode division multiplexer in silicon using subwavelength gratings,” *Applied Optics*. **(submitted)**
3. **Manoranjan Minz** and Ramesh Kumar Sonkar, “Hybrid mode and wavelength division multiplexing on silicon-on-insulator platform,” *Applied Optics*, Volume 60, Issue 9, March 2021, Pages 2640-2646.
4. Dhiman Kakati, **Manoranjan Minz**, and Ramesh Kumar Sonkar, “Performance Analysis of Grating-Assisted Passive MDM using Silicon Photonics for High-Speed RoF/RoFSO Communication,” *Optical Engineering*, Volume 60, Issue 1, January 2021, Pages 016102.
5. **Manoranjan Minz** and Ramesh Kumar Sonkar, “Numerical Modeling and Analysis of a TM Mode-Division (De)multiplexer Based on Grating Assisted Couplers,” *Optical and Quantum Electronics*,Volume 52, Issue 9, September 2020, Pages 1-19.
6. **Manoranjan Minz** and Ramesh Kumar Sonkar, “Design and Analysis of a Grating Assisted Hybrid Mode and Polarization Division (De)multiplexer,” *Applied Optics*, Volume 59, Issue 3, January 2020, Pages 785-794.
7. **Manoranjan Minz** and Ramesh Kumar Sonkar, “Numerical Design and Analysis of a 3-channel Grating Assisted Mode-Division (De)multiplexer,” *Optik*, Volume 187, June 2019, Pages 272-277.

Conference Publications

1. Darpan Mishra, **Manoranjan Minz**, and Ramesh Kumar Sonkar, “Performance of a Pre-amorphized Traveling-wave Silicon Optical Modulator,” *Asia Communications and Photonics Conference 2021 (ACP 2021)*, Sanghai, China, 24-27 October 2021.
2. **Manoranjan Minz**, Darpan Mishra, and Ramesh Kumar Sonkar, “SWG-based compact broadband two-mode multiplexer on SOI platform,” *2021 IEEE Region 10 Symposium (TENSYMP)*, Grand Hyatt Jeju, Republic of Korea, 23-25 August 2021.
3. Darpan Mishra, **Manoranjan Minz**, and Ramesh Kumar Sonkar, “Effect of Pre-amorphization and Annealing on the Performance of a Silicon Optical Phase Shifter,” *Frontiers in Optics 2020*, Washington, DC United States, 14-17 September 2020.
4. **Manoranjan Minz**, Darpan Mishra, and Ramesh Kumar Sonkar, “Compact Polarization Beam Splitter Using Contra-Directional Gratings on SOI platform,” *14th Pacific Rim Conference on Lasers and Electro-Optics 2020*, Australia, 3-5 August 2020.
5. Darpan Mishra, **Manoranjan Minz**, and Ramesh Kumar Sonkar, “Performance Evaluation of a Quasi-TM Mode Silicon Optical Modulator,” *2020 IEEE Region 10 Symposium (TENSYMP)*, Dhaka, Bangladesh, 5-7 June 2020.
6. Darpan Mishra, **Manoranjan Minz**, and Ramesh Kumar Sonkar, “A 2D Optimization Model for Silicon Optical PN Phase Shifter Simulation,” *2020 IEEE 8th International Conference on Photonics (ICP)*, Kota Bharu, Malaysia, 12 May-30 June 2020.
7. **Manoranjan Minz**, Darpan Mishra, and Ramesh Kumar Sonkar, “Design of a Hybrid Mode and Polarization Division Multiplexer,” *2019 Asia Communications and Photonics Conference*, Chengdu, China, 2-5 November 2019.
8. **Manoranjan Minz**, Darpan Mishra, and Ramesh Kumar Sonkar, “Grating assisted MDM-PDM hybrid (de)multiplexer for optical interconnect applications,” *SPIE/COS Photonics Asia 2019*, Hangzhou, China, 20 - 23 October 2019.

9. Darpan Mishra, **Manoranjan Minz**, and Ramesh Kumar Sonkar, "Bandwidth optimization of germanium-doped silicon optical modulator for high-speed applications," *SPIE/COS Photonics Asia 2019*, Hangzhou, China, 20 - 23 October 2019.
10. **Manoranjan Minz**, Darpan Mishra, and Ramesh Kumar Sonkar, "Mode-Division Multiplexer with Contra-directional Couplers," *24th Optoelectronics and Communications Conference/Photonic in Switching and Computing Conference (OECC/PSC 2019)*, Fukuoka, Japan, 7-11 July 2019.
11. **Manoranjan Minz**, Darpan Mishra, and Ramesh Kumar Sonkar, "Design of a 3-channel Mode-division Multiplexer Based on Grating Assisted Couplers," *41st Photonics & Electromagnetics Research Symposium PIERS 2019*, Rome, Italy, 17 - 20 June 2019.
12. Darpan Mishra, **Manoranjan Minz**, and Ramesh Kumar Sonkar, "Effect of Germanium Doping on the Performance of a Silicon Optical Modulator," *41st Photonics & Electromagnetics Research Symposium PIERS 2019*, Rome, Italy, 17 - 20 June 2019.
13. **Manoranjan Minz**, Darpan Mishra, and Ramesh Kumar Sonkar, "Design of a Grating Assisted Mode-Division Multiplexer," *7th IEEE International Conference on Photonics*, Langkawi, Malaysia, 9-11 April 2018.
14. Darpan Mishra, **Manoranjan Minz**, and Ramesh Kumar Sonkar, "Mode and Loss Analysis of an Ultra-Small Graded-Index Strip Waveguide for Multimode Datacenter Applications," *7th IEEE International Conference on Photonics*, Langkawi, Malaysia, 9-11 April 2018.

1

Introduction

Contents

1.1 Silicon Photonics

Silicon is considered to be the workhorse of the semiconductor industry because of its versatility and availability in abundance. When a material or process is not compatible with the standard practices involved in the semiconductor industry, the total cost of the fabrication process becomes huge [1]. The compatibility of silicon photonics with the standard complementary metal-oxide-semiconductor (CMOS) technology enables monolithic integration of photonics and microelectronics [2–4]. With years of development in the microprocessor industry, mass production cost has been minimized. Since the first introduction of silicon photonics platform in 1985 by Soref and Lorenzo [5], a phenomenal progress has been made in developing various integrated optoelectronic devices which include modulators [6–11], photodetectors [12–15], light sources [16–20], optical amplifiers [21–24], biosensors [25–29], optical filters [30–34], multiplexers [35–38], etc. This is made possible due to the advantages offered by silicon photonics which are absent in other photonic platforms.

The silicon-on-insulator (SOI) platform has high refractive index contrast between the silicon core (n_{Si} = 3.473 at 1550 nm) and the silicon dioxide cladding (n_{SiO_2} = 1.444 at 1550 nm) [39]. This high index contrast provides better confinement of the guided optical modes, which makes it possible to have tighter waveguide bends and hence smaller device footprint is achievable. Moreover, its birefringence property helps in developing polarization handling devices. Silicon has high third-order optical nonlinear properties and high thermo-optic coefficient of $1.8 \times 10^{-4}/^{\circ}C$, which makes it a suitable material for implementation in photonic devices. The Kerr effect in silicon is about 100 times stronger than that of silica fiber, whereas the Raman effect is about 1000 times stronger [40, 41]. These nonlinear optical interactions in chip-scale devices enable optical amplification, lasing action, and wavelength conversion, which were thought to be beyond the reach of silicon until recently. Silicon shows low-loss characteristic in the wavelength window extending from 1.1 to 7 μm. Silicon is not only limited to the near-infrared (IR) telecommunication band of 1.3 to 1.55 μm but also an excellent material for being used in mid-IR range [42]. Silicon photonics offers a promising platform for developing high-performance optoelectronic devices which hold the potential to be a genuinely disruptive technology, and it is entering into a phase of increased commercialization in the data center and high-performance computing systems.

1.2 Motivation

In the year of 1946, Electronic Numerical Integrator And Computer (ENIAC), the first electronic general-purpose computer was introduced, which contained about 7200 crystal diodes, 20,000 vacuum tubes, 1500 relays, 10,000 capacitors, 70,000 resistors, and approximately 5,000,000 hand-soldered joints (see Fig. 1.1(a)). It could execute 50,000 instructions per second, and it used to take the space of a large room [43]. Whereas in 1971, the first general-purpose commercial microprocessor, i.e., Intel 4004 built with 2300 transistors, was of a fingernail size (see Fig. 1.1(b)), which was used in a pocket-sized calculator and had the same computing power as the ENIAC [44]. It is all because of the transistors that revolutionized the whole electronics industry. As the semiconductor fabrication facilities were improved, the computing performance of the computing systems was also increased. It can be noted that devices started becoming more compact and more powerful at the same time.

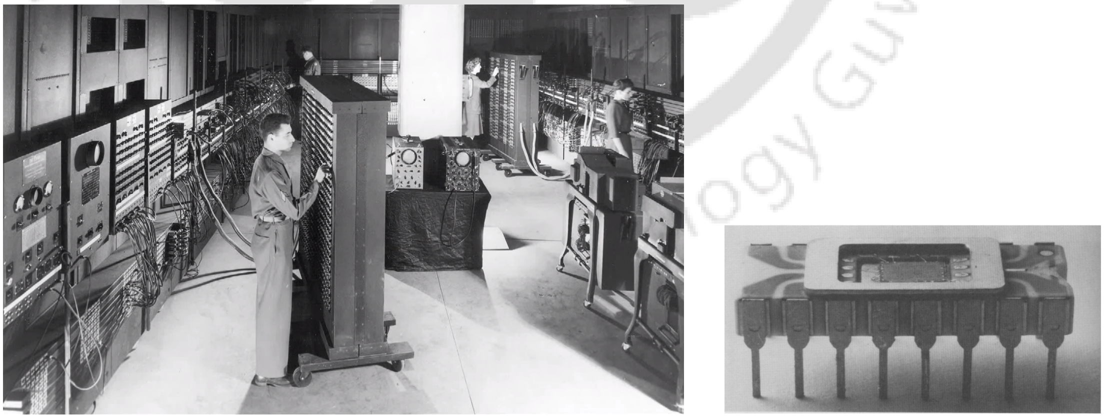

(a) **(b)**

Fig. 1.1: (a) ENIAC, the first electronic general-purpose computer [45]; (b) Intel 4004, the first general-purpose commercial microprocessor [46].

As per Moore's law the number of transistors in the electronic integrated circuit doubles in every 18-24 months [47]. For the processor to perform more computation per second or to achieve higher clock frequency, the minimum feature size has been decreasing. Due to a decrease in the minimum feature size and dense packing of wires, the parasitic resistance and capacitance increase, causing propagation delay which is known as interconnect bottleneck [48]. Higher clock frequency also results in more power dissipation, which creates a practical limit on clock frequency to be used without an advanced cooling system. Furthermore, the scaling of clock frequency and the growth in the number of transistors made designing, developing, and debugging such systems more challenging.

To overcome these challenges and continue performance improvement, attention was shifted to multi-threaded and multi-core processors since parallel code execution via multiple cores increased the number of computations [49]. This is still continuing to be the case; for example, the Corona architecture, which consists of 256 cores, requires a bandwidth of 10 TBps for on-chip/off-chip communication [50]. The only viable solution to meet such bandwidth requirements and avoid the electrical interconnect issues is to use optical interconnect networks [51,52]. Optical interconnects provide bandwidth transparency and low power consumption per bit or per distance as compared to their electrical counterpart [53]. Taking into account the trend of increase in number of cores, it is expected that in the coming years, the number of cores will increase to more than 1000. Thus the link capacity of the optical interconnect must be improved further, which can be achieved by utilizing different multiplexing technologies, including mode-division multiplexing (MDM) [54–57], polarization-division multiplexing (PDM) [58,59], and wavelength-division multiplexing (WDM) [60–66].

WDM technology enables the transmission of optical signals on multiple channels with different wavelengths in long-haul optical communication systems and data centers. However, in a WDM system, multiple light sources of different wavelengths require precise alignment, tuning, and stabilization with temperature control, making the device costlier and more power-consuming. Such expense is justified for data center application and long-haul communication; however, it is highly expensive and power-hungry for on-chip optical networks. That is why researchers started focusing their attention on enhancing the link capacity even with a single wavelength light source. In such cases, PDM and MDM technologies are found to be very useful. These two techniques require only one source of a particular wavelength where different data are transmitted on different polarizations or waveguide eigenmodes. Research is going on to improve WDM, MDM, and PDM technologies; however, as the demand for high-link capacity is growing exponentially, each multiplexing technology individually will not be sufficient to meet the high demands in the future. One solution is to combine different multiplexing schemes to actualize a multi-dimensional hybrid multiplexer for significant improvement in the total capacity (up to peta-bits per second) [52,67,68]. Although considerable research efforts have been taken to enhance the above individual technologies in the past decades, at present, developing hybrid multiplexing technology is still in its early stage. Hybrid multiplexers have become highly crucial for faster optical interconnects, and thus the motivation of this thesis work is to explore different multiplexing techniques, design hybrid (de)multiplexers, and establish their analytical and numerical models.

1.3 Grating Assisted Couplers

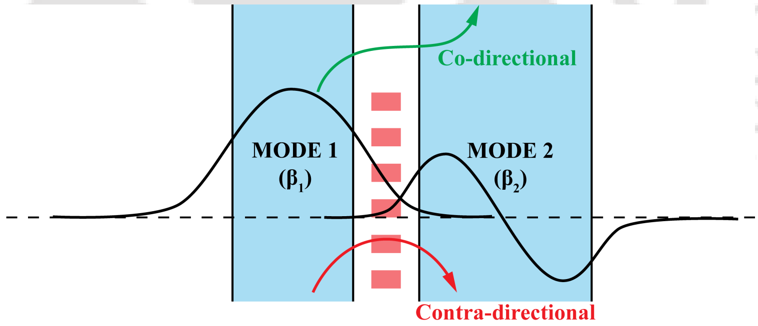

Fig. 1.2: Composite structure with grating structures and two waveguides

The grating structures are periodic variations of dielectric media in only one direction, which may cause energy transfer between the unperturbed waveguide modes of a composite structure, provided the required phase-matching conditions are satisfied. When energy transfer can occur between two modes, the modes are said to be coupled. Figure 1.2 shows a composite structure consisting of two waveguides and grating structures. The fundamental mode (MODE 1) of the first waveguide and first-order mode (MODE 2) of the second waveguide are assumed to be coupled. Let the two coupled modes are represented as $E_1(x,y)e^{j(\omega t-\beta_1 z)}$ and $E_2(x,y)e^{j(\omega t-\beta_2 z)}$.

The governing coupled-mode equations can be written as [69]:

$$\frac{dA_1}{dz} = -j\frac{\beta_1}{|\beta_1|}\kappa A_2(z)e^{j\Delta\beta z} \tag{1.1a}$$

$$\frac{dA_2}{dz} = -j\frac{\beta_2}{|\beta_2|}\kappa^* A_1(z)e^{j\Delta\beta z} \tag{1.1b}$$

where

$$\Delta\beta = \beta_1 - \beta_2 - m\frac{2\pi}{\Lambda}, \ m \text{ is an integer} \tag{1.2}$$

where A_1, A_2 (β_1, β_2) are the field amplitudes (propagation constants) of the two coupled modes, Λ is the period of the perturbation, κ is the coupling coefficient, and z is the propagation direction.

Energy exchange between two modes is possible if the phase-matching condition is satisfied and there is physical overlapping between the mode field profiles. Depending on the direction of the propagation of the modes, it can be categorized as co-directional coupling or contra-directional coupling. The phase-matching conditions for both categories are shown below [69].

$$\text{Co-directional coupling:} \qquad \beta_1 - \beta_2 = \frac{2\pi}{\Lambda} \tag{1.3a}$$

$$\text{Contra-directional coupling:} \qquad \beta_1 + \beta_2 = \frac{2\pi}{\Lambda} \tag{1.3b}$$

The coupling coefficient is a measure of the coupling strength between the two coupled modes, which is defined as:

$$\kappa = \frac{\omega\epsilon_0}{4}\iint E_1^*(x,y)\, \Delta n^2(x,y)\, E_2(x,y)\, dx\, dy \tag{1.4}$$

where ω is the optical frequency of operation, ϵ_0 is the permittivity of vacuum, and E_1, E_2 are the electric field mode profiles. Δn^2 denotes the refractive index profile of the grating structure. The coupling coefficient reflects the magnitude of the coupling. Higher the value of coupling coefficient, the lesser length will be required for complete power transfer.

The grating-assisted silicon photonic devices show promising coupling characteristics, which have played a pivotal role in developing many novel applications. In [70], an integrated grating-assisted coupler based tunable optical delay line is demonstrated with an ultra-compact reflector. A phase-modulated grating-assisted coupler based narrow-band add-drop filter is proposed in [71]. Grating-assisted contra-directional couplers have been utilized in SiN rib waveguides to realize on-chip pump rejection filter with high free spectral range [72]. A grating-assisted compact hybrid silicon photonic multimode resonator has been presented in [73], where the proposed device is resonant at the fundamental and first-order guided TE modes.

1.4 Subwavelength Grating Waveguides

Subwavelength gratings (SWGs) have gained a lot of interest recently for developing compact and high-performance photonic integrated devices for optical interconnect applications [74]. Figure 1.3 shows the structure of a subwavelength grating based waveguide structure, which consists of periodic high (n_1) and low (n_2) refractive index media, where the grating period is very small compared to the operating wavelength ($\Lambda << \lambda$). Due to this, the diffraction effect is suppressed, and the grating structures can be treated as a homogeneous medium with an equivalent refractive index. The refractive index can be engineered by changing the period and duty cycle of the gratings. Rytov has given an equivalent refractive index formula for the subwavelength grating structures, which is given as [75]

$$n_{\|}^2 = \frac{a}{\Lambda} n_1^2 + \left(1 - \frac{a}{\Lambda}\right) n_2^2 \tag{1.5a}$$

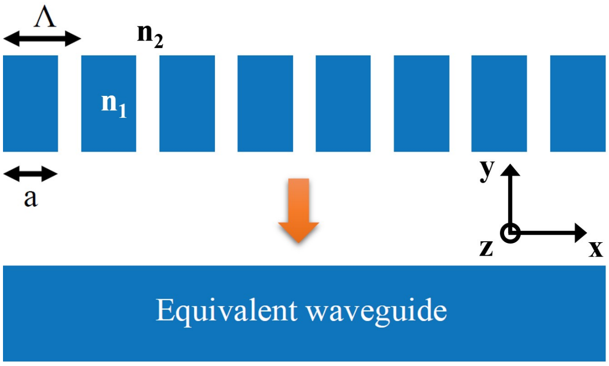

Fig. 1.3: Subwavelength grating waveguide structure

$$\frac{1}{n_{\perp}^2} = \frac{a}{\Lambda}\frac{1}{n_1^2} + \left(1 - \frac{a}{\Lambda}\right)\frac{1}{n_2^2} \tag{1.5b}$$

where || indicates that the field polarization is along z-direction and $\perp$ corresponds to x-directed field. The demerit of the above expression is that it is only applicable when the gratings are infinite along y- and z-direction. So to find the supported Bloch modes of the subwavelength grating waveguide, numerical tools such as Lumerical FDTD or OptiFDTD can be used. The numerical tools help in analyzing the band structure, and the necessary frequency versus wave vector plots can be obtained for different supported modes.

Due to the delocalized field and substantial penetration of the evanescent field in the cladding region, the coupling strength increases, and hence low coupling length is required, resulting in less device footprint [76]. In addition, reduced sidewall field interaction in SWG results in better loss performance than the channel waveguides. The above advantages have led to the realization of SWG-based asymmetric directional couplers (ADCs), which have much lower coupling lengths than the conventional strip waveguide-based ADCs [76]. Thus SWG-based waveguides show great potential for the realization of compact multiplexers. SWG structures have been employed in many different applications such as waveguide crossing [77], fiber-to-chip coupler [78], polarization splitter and rotator [79], MMI coupler [80], filter [81], and directional coupler [82].

1.5 Thesis Organization

The thesis has been organized in seven chapters. The content of the individual chapters are as follows:

Chapter 1 introduces to the field of silicon photonics and its applications. The motivation behind this thesis work has been discussed along with the basic theory of grating assisted couplers and subwavelength grating waveguides.

Chapter 2 discusses various multiplexing techniques utilized in optical interconnect applications. A literature review on optical multiplexer is presented including the current national and international research scenario.

Chapter 3 presents two MDMs, one based on TE polarization and the other based on TM polarization. The TE and TM MDMs are designed using silicon slab waveguides and gratings. The devices are analyzed using the 2D FDTD simulation method. The aspect of supermodes for determining the suitable gap between the waveguides has been introduced in order to minimize the return loss. In addition, the designs of SWG-based TE and TM MUXs have been discussed.

Chapter 4 introduces a grating-assisted hybrid mode and polarization division multiplexer, which is based on cascading a TE MDM and a TM MDM together. The device is designed on the SOI platform with buried strip waveguides. The performance of the device is determined by the 2.5D FDTD technique, which is the combination of EIM and 2D FDTD.

Chapter 5 demonstrates a 6-channel hybrid mode and wavelength division multiplexer with 3 quasi-TE modes and two wavelengths employing contra-directional coupling principle, which is simulated using the 2.5D FDTD method.

Chapter 6 proposes a hybrid (de)multiplexer by incorporating three degrees of freedom: mode, polarization, and wavelength. The design is based on cascaded grating-assisted contra-directional couplers. The device analysis has been performed using 3D FDTD.

Chapter 7 concludes the thesis by describing its contributions and provides scope for future work.

2

On-chip Optical Multiplexing: A Literature Survey

Contents

2.1 Introduction

Silicon photonics has emerged as a promising platform for integration of various optical components to be used in telecom and datacom applications. By leveraging CMOS fabrication technology, silicon photonics enables manufacturing of low cost, low power, compact, and high volume photonic integrated circuits (PICs). The multiplexer is one of the fundamental building blocks of such PICs, which can combine optical signal from multiple sources and transmit the data simultaneously over a single bus waveguide. On the other hand, a demultiplexer essentially reverses the multiplexing operation and distributes the multiplexed data signal from a single bus waveguide to the respective output access waveguides.

2.2 Types of Multiplexing schemes

On-chip optical data communication can leverage various physical attributes of an optical guided wave such as wavelength, mode, and polarization for scaling up the transmission capacity. Depending on the physical attribute, the on-chip optical multiplexing can be broadly divided into

(i) Wavelength-division multiplexing (WDM)
(ii) Mode-division multiplexing (MDM)
(iii) Polarization-division multiplexing (PDM)
(iv) Hybrid multiplexing (combination of multiple multiplexing schemes)

2.2.1 Wavelength Division Multiplexing

In a WDM system, different data signals are transmitted through multiple wavelength channels. It has been in use very widely for more than a decade in long-haul optical networks. WDM systems have been extensively studied using various structures, however, there are two key representatives of WDM, namely arrayed waveguide grating (AWG) [83–87] and microring resonator (MRR) [88–98].

Arrayed waveguide grating consists of an input waveguide array, input star coupler, arrayed waveguides, output star coupler, and an output waveguide array, as shown in Fig. 2.1. Input

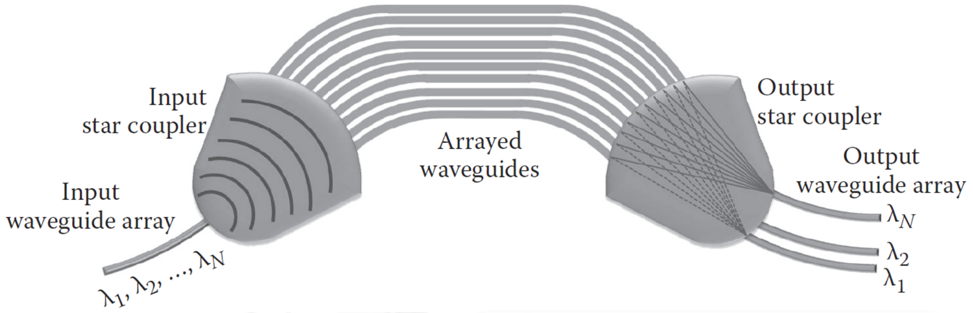

Fig. 2.1: Arrayed Waveguide Grating [99]

star coupler and output star coupler are also known as free propagation region (FPR). Input signal carrying data at different wavelengths enters into the input star coupler, and power is divided into arrayed waveguides. Each consecutive arrayed waveguides have a constant path length difference of ΔL, due to which optical signal in each arrayed waveguide gets delayed by a particular amount. Because of the path difference, the light waves interfere constructively or destructively in the output star coupler in such a way that only a particular wavelength of light is received at the output waveguide arrays, which are located at specific locations.

On the other hand, a microring resonator is a ring-shaped optical waveguide which can either work as a notch filter when coupled with a single straight waveguide or as an add-drop filter when coupled with two parallel straight waveguides. The two configurations are shown in Fig. 2.2. The resonant condition is satisfied when the optical path length of a light beam becomes integer multiple of 2π. In the case of a notch filter, when the light beam with multiple wavelengths enters through the input port, the wavelengths that satisfy the phase-matching condition and the resonant condition get coupled to the ring waveguide and start resonating inside the structure because of the constructive interference with the incoming light. The remaining

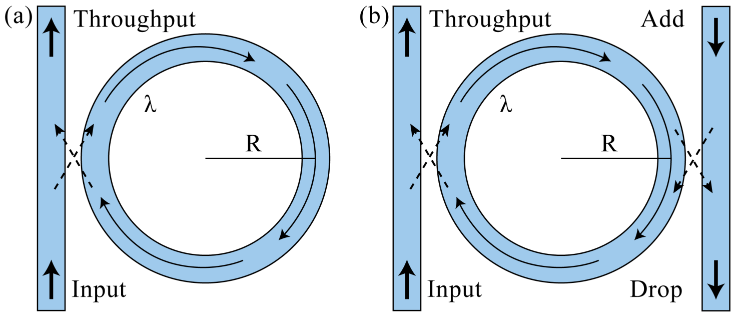

Fig. 2.2: Microring Resonator based (a) Notch Filter, (b) Add-drop filter [99]

wavelengths which do not satisfy the phase-matching condition exit at the throughput port. In the case of the add-drop filter, resonant wavelengths are dropped at the drop port when the two parallel waveguides are identical. The phase-matching and resonant conditions are defined as follows.

Phase matching condition:

$$n_{eff_1} = n_{eff_2} \tag{2.1}$$

Resonant condition:

$$n_{eff_2} \times (2\pi R) = m \times \lambda_{res} \tag{2.2}$$

where n_{eff_1} and n_{eff_2} are the effective refractive indices of fundamental modes supported by the straight waveguide and ring waveguide respectively. R is the radius of the ring waveguide and λ_{res} is the resonant wavelength.

A compact 18-channel wavelength-division multiplexer based on AWG and an MZI optical interleaver is proposed in [100]. The fabricated device has shown channel crosstalk below –15 dB for a 200 GHz channel spacing with a footprint of 520 μm × 190 μm. In [88], multiple rings are cascaded to obtain a box-like response with excess loss less than 1 dB, an extinction ratio of ~36 dB, and sharp rising and falling edges of 48 dB/nm.

From the literature it has been observed that realizing a ultrasmall high-performing WDM based on AWG for dense wavelength division multiplexing application is difficult. WDM requires multiple light sources of different wavelengths (lasers) to be integrated on the chip with precise alignment, tuning, and stabilization with proper temperature control, which makes the device costlier. Moreover, wavelength conversion, switching, and routing make the system more complicated and power-consuming. High cost is acceptable for long-haul networks but for on-chip optical interconnects, it becomes very expensive.

2.2.2 Mode-division Multiplexing

Mode-division multiplexing has been attracting more attention in recent years because of its simplicity and capability to send and receive data on different eigenmodes of the multimode waveguide. Mode-division multiplexer has been demonstrated using various structures such as ADC [101–105], asymmetric Y-junction [106–109], multimode interferometers (MMIs) [110–114], adiabatic tapers [115–122], adiabatic couplers and micro Y-junction [123], SWG [124], densely packed waveguide arrays (DPWA) [125], asymmetric plasmonic dielectric couplers [126], etc. The number of mode channels of an MDM system is equal to the number of eigenmodes supported by the waveguide; however as the number of modes increases, it becomes complicated to regulate each mode separately. It has been found that MMI based structures are very complicated and inconvenient to use for multiple mode channels. Mode evolution structure based designs require precise fabrication, and therefore it is relatively difficult. Adiabatic design enables ultra-wide bandwidth but at the cost of a large device length.

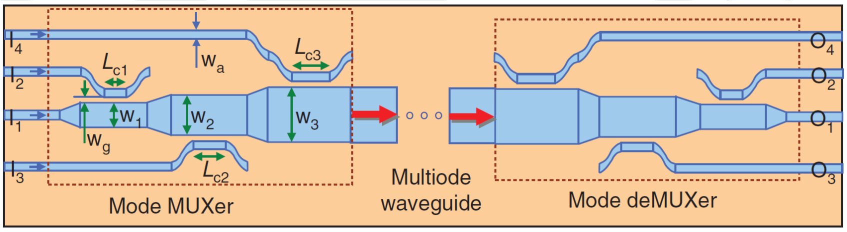

Fig. 2.3: Asymmetrical directional coupler based MDM [36]

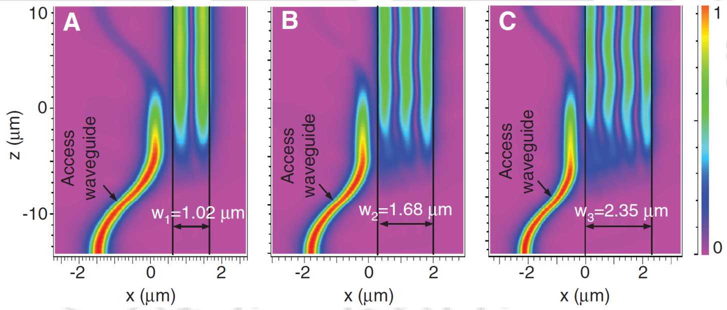

Fig. 2.4: Power coupling between the modes of two different waveguides [36]

An asymmetrical directional coupler based 4-channel mode-division multiplexer [36] is shown in Fig. 2.3. The widths of the three wide multimode waveguide portions and the single-mode waveguides are such that the effective refractive index of the fundamental TM mode in the single-mode is matched with the first, second, and third-order TM modes at the three coupling regions. As the co-directional phase-matching conditions are satisfied, power coupling occurs between respective modes, shown in Fig. 2.4. Power from the single-mode waveguides are transferred to the higher-order modes and are multiplexed into a multimode bus waveguide which carries all the data. Then all these signals are demultiplexed by the demultiplexer at the receiver end. At the demultiplexer, power from higher-order modes is also coupled to fundamental modes of respective single-mode waveguides due to the phase-matching. The fundamental mode remains unaffected the whole time. Tapers used at the junction of two waveguides with different widths help in discarding unwanted higher-order modes at the output. Devendra Chack et al. [127] have demonstrated a compact and broadband silicon on-chip mode converter and demultiplexer using MMI for mode-division multiplexing on SOI platform with IL < 0.36 dB and CT < –24.4 dB at 1550 nm. Jyoti Prasad Nath et al. [128] have utilized collaterally coupled waveguides to realize a compact 5-channel MDM operating at 1550 nm with a device length of 38.89 μm, IL < 0.24 dB, and CT < –33 dB.

The challenge with the MDM system is that only a limited number of modes can be effectively controlled. As the number of modes increases, it becomes tough to regulate each mode separately. Generating different modes independently in a multimode waveguide has been an issue from the beginning. Radii of the curvatures have to be large to avoid mode mixing, which translates to a larger footprint. Higher inter-modal crosstalk occurs because of difficulty in selective high-order mode coupling.

2.2.3 Polarization-division Multiplexing

PDM is another low-cost technique to improve the link capacity of optical interconnect. Planar optical waveguides are very good at maintaining the polarization state of light. Polarization handling devices such as polarization beam splitter (PBS) and polarization rotator (PR) are two primary components of a polarization multiplexing system, as shown in Fig.2.5. It is often desired to achieve broadband PBS and PR so that it can be integrated with WDM for hybridization.

PBS is the multiplexing unit of the PDM system. There are many PBSs that are realized by using MMI [129], directional couplers (DC) [130], Mach-Zehnder interferometer (MZI) [131], etc. Among them, DC-based PBS is the simplest. Devices built on the SOI platform are highly birefringent, which means TE and TM polarization waves experience different effective refractive indices. Symmetrical DC has two identical waveguides, and the coupling length

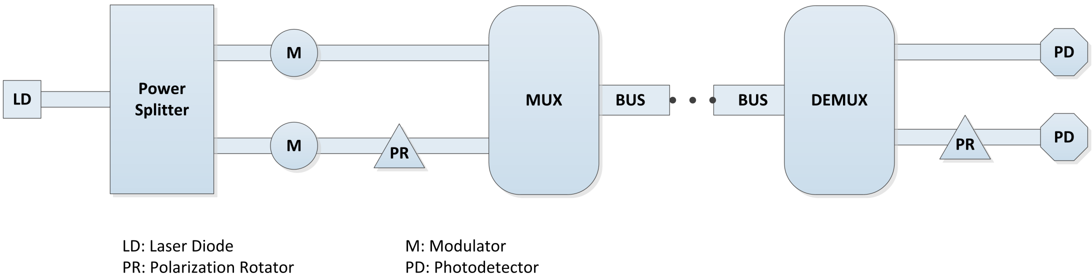

Fig. 2.5: Polarization Division Multiplexing System

is chosen such that it is equal to even multiple of the beat length of one polarization and odd multiple of the other polarization. In this way power of one polarization is coupled to the nearby waveguide and the other polarization wave remains in the same waveguide.

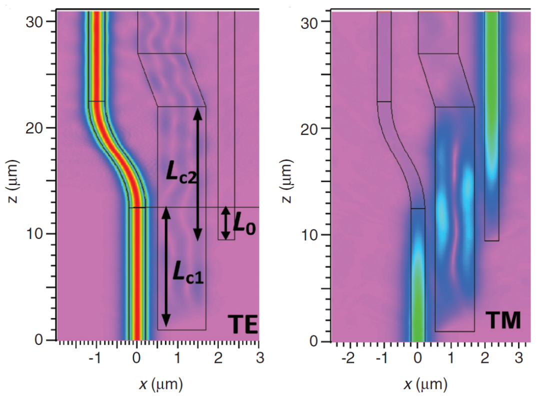

Fig. 2.6: Asymmetrical Directional Couplers based Polarization beam splitter [132]

A PBS based on an asymmetrical directional coupler [132] is shown in Fig. 2.6. Widths of the single-mode waveguide and multimode waveguide are chosen in such a way that phase is matched for fundamental TM mode (TM_0) of single-mode waveguide and first-order TM mode (TM_1) of multimode waveguide i.e., $n_{TM_0} = n_{TM_1}$. So there is power coupling between TM_0 to TM_1 and finally to fundamental mode of another single-mode waveguide. Since phase is not matched for TE_0 mode with any of the higher-order modes of the multimode waveguide, TE_0 continues to propagate in the same single-mode waveguide and exits at its output.

The polarization rotator for higher order modes has been demonstrated on SOI platform [133, 134]. In [133], the authors have been able to convert first order TE mode of a 220 nm thick Si strip waveguide to first-order TM mode by using bi-level mode converter and asymmetric directional coupling with 90% conversion efficiency. Whereas in [134], a square cross-section waveguide with each side of 1 μm and a cut corner is used to convert the higher-order mode E_{22} (TE) to E_{22} (TM) with a polarization conversion efficiency of 96%. The conventional PBS mostly work for fundamental modes. Polarization beam splitter that can deal with higher-order modes of both polarizations is still not available. It is complicated to manufacture PBSs with high fabrication tolerance, high extinction ratio, and low excess loss [52].

2.2.4 Hybrid Multiplexing

Demands for high link capacity are increasing exponentially, whereas the present individual multiplexing technologies can only handle on an average of up to 10 channels. So to satisfy the future demands of huge link capacity, a combination of multiple multiplexing schemes can be used to form a hybrid multiplexing scheme. For example, PDM and MDM can be used to achieve more than 10 channels (5 TE mode channels and 5 TM mode channels) to handle ~1 Tbps with a single wavelength assuming the bit rate for a single channel is 100 Gbps. Further enhancement can be done by using it together with WDM to reach a single waveguide capacity of about ~100 Tbps. Capacity can be further improved to ~1 Pbps by adding multicore space-division multiplexing [52].

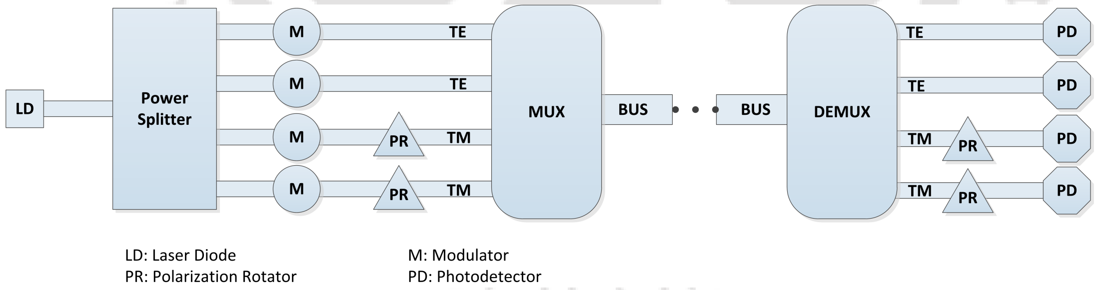

Fig. 2.7: Hybrid MDM-PDM System

There are two polarization eigenmodes in a waveguide, TE and TM. Thus, designing an MDM device for both TE and TM modes doubles the channel capacity of an MDM with a single wavelength. There have been many devices capable of hybrid multiplexing reported recently. A schematic of a typical hybrid MDM-PDM system is given in Fig. 2.7. MDM-PDM hybrid multiplexers are developed by using densely packed waveguide arrays and adiabatic taper [135], asymmetrical Y-junction [136], ADCs [137]. Figure 2.7 shows a hybrid MDM-PDM system, where the MUX is an essential component that combines the dual-polarization of multiple modes. Similarly, the total channel capacity of a WDM system can be doubled by combining it with the PDM scheme such that for each wavelength channel there are two polarization modes. PDM-WDM hybrid multiplexers based on bi-directional AWG, PBS and PR [100], AWGs and 2D grating coupler [138] have also been reported. When the MDM system has a broad bandwidth characteristic, multiple wavelength channels separated by a few nanometers (depending upon the bandwidth and the usage of CWDM or DWDM scheme) could be sent in a specific mode, and hence the total number of channels of a particular MDM-WDM system becomes the number of mode channels multiplied by the number of wavelength channels. MDM-WDM systems have been reported using structures like Asymmetric Y-junction [68], MMI and Y-junction [139], MRM matrix and ADC [140], ADCs and AWGs [141], asymmetrical Y-junction [142], tapered DC [143], ADCs and microring resonators [144], etc.

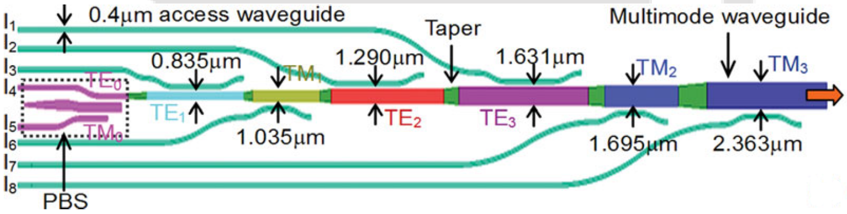

Fig. 2.8: 8-channel ADC based Hybrid MDM-PDM multiplexer [137]

An example of an 8-channel ADC-based Hybrid MDM-PDM multiplexer [137] is shown in Fig. 2.8. The widths of each multimode waveguide section are chosen such that phase-matching conditions are satisfied and power from the fundamental mode of the narrow single-mode waveguides is coupled to higher-order modes of the respective wide multimode waveguide sections. There are eight coupling sections where four sections are used to couple TE modes and the remaining four sections to couple TM modes separately. Table 2.1 shows a performance comparison of a few reported (de)multiplexers in terms of the number of channels, insertion loss, and crosstalk.

Table 2.1: Performance of different (de)multiplexers from the literature

References	**Structure**	**Number of Channels**	**IL (dB)**	**CT (dB)**
[145]	Adiabatic couplers, micro Y-junction	2 TE modes	<1.5	<–19
[76]	Subwavelength grating	2 TE modes	<1	<–10
[112]	Symmetric Y-junction, MMI	2 TE modes	<0.3	<–31
[146]	Asymmetric Y-junction	2 TE modes	<0.56	<–12.8
[147]	MRM	2 TE modes	<1.2	<–22.2
[148]	DPWA	16 TE modes	<0.1	<–30
[149]	Multimode grating assisted couplers	4 TE modes	<0.34	<–22.6
[140]	ADC and MRM matrix	16 (4 modes and 4 wavelengths)	<1	<–20
[143]	Tapered directional coupler and MMI	4 (2 modes and 2 wavelengths)	<1.2	<–18
[67]	MRR	6 (2 modes and 3 wavelengths)	<26 (including fiber-to-chip coupling loss)	<–22
[135]	DPWA and Adiabatic taper	5 (3 TE and 2 TM modes)	<0.05 (theoretical) <0.6 (experimental)	<–20 (theoretical) <–15 (experimental)
[116]	ADCs	5 (3 TE and 2 TM modes)	<1.1	<–24
[137]	ADCs	8 (4 TE and 4 TM modes)	<10 (TM) <20 (TE)	<–10
[100]	AWG, PBS and PR	18 (9 TE and 9 TM modes)	<10	<–13
[138]	AWGs and 2D grating coupler	16 (8 TE and 8 TM modes)	<2.6	<–21.5

2.3 Major Challenges in SOI Platform

Silicon is a promising material platform for guiding optical signal, however it is highly challenging to develop light sources due to its indirect bandgap. Various attempts have been made to realize lasing action in silicon by implementing quantum confinement effect [150, 151], Raman scattering [152, 153], blackbody radiation [154, 155], etc. However, efficiency of these silicon laser sources are low and due to which they are not suitable for optical interconnects. Therefore, III-V semiconductor lasers with direct bandgap are heterogeneously integrated to silicon chips [156–159]. The high index contrast in silicon photonic waveguides results in compact device footprint but makes the device very sensitive to variations in the geometry, which is incurred due to lithography effect and wafer thickness variation. The nanometer scale roughness in the silicon waveguide can lead to undesired reflections and scattering losses [160, 161]. This reflected or scattered light may interfere with the source signal and give erroneous output. Thus, high-fidelity geometries are required for better device performance. In multiplexing systems involving higher-order waveguide modes, it is challenging to develop sharp bends in multimode waveguides while avoiding mode mismatch and exhibiting low modal crosstalk and low loss [162, 163]. Subwavelength grating structures are suitable for realizing such waveguide bends [164]. The electrical interconnects suffer from high heat dissipation, whereas optical interconnects do not have heating issue. However, the heat generated from other sources (e.g. atmosphere, electronic components, and metal heaters) can affect the optical signal since silicon has a high thermo-optic coefficient [161]. Taking leverage of this effect, in wavelength-selective photonic devices, temperature variation can be utilized to cause a spectral shift such that the fabrication variation is compensated. At present, most of the photonic circuits are defined on a single layer, thus waveguide crossings are certainly unavoidable. The SOI waveguides do not suffer from excessive crosstalk and loss at the crossings, however the routing algorithm should be implemented such that the number of waveguide crossings are minimized. For multi-layer circuits, it becomes difficult to realize efficient optical vias in high-index contrast platform such as SOI [165].

2.4 Key Parameters of On-chip Multiplexer

The key performance metrics of a multiplexer are

(i) Insertion loss:

When an optical device is inserted into a setup, total power transfer may not occur from the input port of the device to the desired output port due to some losses. This power loss is called insertion loss (IL) and is given by,

$$IL = 10\log\left(\frac{Input\ power}{Power\ at\ the\ desired\ output\ port}\right) \tag{2.3}$$

(ii) Return loss: The return loss (RL) is defined as the amount of power reflected back at the input port and is given by,

$$RL = -10\log\left(\frac{Input\ power}{Power\ reflected\ at\ the\ input\ port}\right) \tag{2.4}$$

(iii) Crosstalk:

Crosstalk (CT) is defined as the undesired power flow from input port to an output port which can be expressed as,

$$CT = -10\log\left(\frac{Power\ at\ the\ desired\ output\ port}{Power\ at\ the\ undesired\ output\ port}\right) \tag{2.5}$$

(iv) Number of channels:

Data can be transmitted over different types of channels such as mode-channel, wavelength channel, or polarization channel. It refers to the number of users that can send data at a given time instant. The higher number of channels ensures a higher aggregate data rate.

(v) Footprint:

Footprint refers to the amount of physical space occupied by a device. Photonics devices with a large footprint make the whole system bulky and sometimes incompatible for photonic-electronic integration.

(vi) Fabrication tolerance:

Fabrication tolerance is the permissible limit of deviation from the actual physical dimension of the device. It is an essential factor in determining the performance of a device. It is crucial to find the minimum variation in dimension for which the outcome of the system is not affected.

The positive sign convention is taken for insertion loss, whereas the negative sign convention for return loss, and crosstalk has been used in this thesis.

2.5 International Status

Several groups, all around the world, are actively contributing towards improvement in the domain of photonics. Some of them are the Silicon Integrated Nanophotonics Group (SING) of Zhejiang Univesity, China; the Physical Optics and Electronics Group of Massachusetts Institute of Technology, United States of America; Valencia Nanophotonics Technology Centre, Spain; DTU FOTONIK, Department of Photonics Engineering, at the Technical University of Denmark, Denmark; the Australian National University, Australia; the Alexandria University, Egypt; and the Hebrew University of Jerusalem, Israel.

2.6 National Status

There are many universities/institutes in India which are working in the field of photonics, namely the Indian Institute of Technology (IIT) Bombay, IIT Delhi, IIT Kanpur, IIT Madras, Indian Institute of Science (IISc) Bangalore etc. Their research area focuses on Fibre lasers, Fibre Bragg Gratings, Integrated Optics and Plasmonics, Optical Communication and Networks, nonlinear optics, Organic LEDs and devices, Photonics of liquid crystals, Light-matter interactions in Photonic architectures, etc. The research groups from the Delhi University and IIT (ISM) Dhanbad are actively involved in developing on-chip multiplexers.

2.7 Summary

This chapter presented a brief overview of various (de)multiplexing schemes which can be utilized for capacity improvement of on-chip optical interconnects. The key parameters for analyzing the multiplexer performance have been defined. A brief description of the international and national status has been provided, including the recent research work in the on-chip multiplexer domain.

3

Mode-division (De)multiplexers

Contents

3.1 Introduction

The architecture of processors has been shifted to multi-threaded and multi-cores to achieve higher performance while executing more computations per second, as the clock frequency of the processors has reached its practical limit due to high power dissipation [1]. Parallel code execution via multiple cores increases computation speed and thus, the number of cores has been increasing to satisfy high bandwidth demand [49]. However, the traditional electrical interconnects will not be able to meet future demands due to the interconnect bottleneck [166]. Complementary metal-oxide-semiconductor (CMOS) compatible optical interconnect has emerged as a promising solution that can provide high bandwidth and low power consumption per bit or per unit distance as compared to the electrical counterpart [167]. The capacity of the optical interconnects can be improved by employing different multiplexing techniques, such as Wavelength Division Multiplexing (WDM), Mode-Division Multiplexing (MDM), and Polarization Division Multiplexing (PDM) [168]. WDM technology is widely used in datacenters and long haul communication systems, where different wavelengths act as individual data channels. However, for on-chip optical interconnects, WDM becomes highly expensive since it requires multiple wavelength sources with precise alignment, stabilization, and tuning [52]. Therefore, multiplexing scheme like MDM that requires only a single wavelength source has garnered much attention recently. MDM scheme enables data transfer via different eigenmodes of the waveguide [168]. MDM systems have been demonstrated using various structures such as, asymmetrical directional couplers (ADC) [36, 67, 144, 147, 169, 170], Y-junctions [107, 145], multimode interference waveguides (MMI) [112], mode evolution counter tapered couplers [122, 162], sub-wavelength gratings (SWG) [76], tilted-branch bus structure [171], plasmonic-dielectric waveguide-based directional coupler [126, 172], densely packed waveguide arrays (DPWA) [148], etc. The previously reported MDM [149], which is based on grating assisted couplers, tend to have large device length due to cascaded grating structures. It is also possible to realize an MDM by employing co-directional and contra-directional coupling simultaneously, as given in [173, 174]; however, this leads to unwanted coupling between the modes resulting in high return loss. To reduce the device length and minimize the return loss, periodic perturbations can be placed in between the waveguides on both sides of the bus waveguide, where different modes are simultaneously reflected back using contra-directional coupling.

3.2 TE mode-division (de)multiplexer

In this chapter, a device structure which is able to (de)multiplex three TE modes at 1550 nm wavelength has been proposed and numerically analyzed using 2D-FDTD. The proposed device is bi-directional and can also be used to multiplex three TE modes. To achieve this, two gratings with different grating periods are used to separate two higher order TE modes of the multimode waveguide to fundamental modes of the two identical single mode waveguides, whereas the fundamental mode of the multimode waveguide keeps propagating in the same direction. The performance of the proposed MDM device has been analyzed by observing insertion loss, return loss, and crosstalk exhibited by the device.

3.2.1 Proposed Device Structure

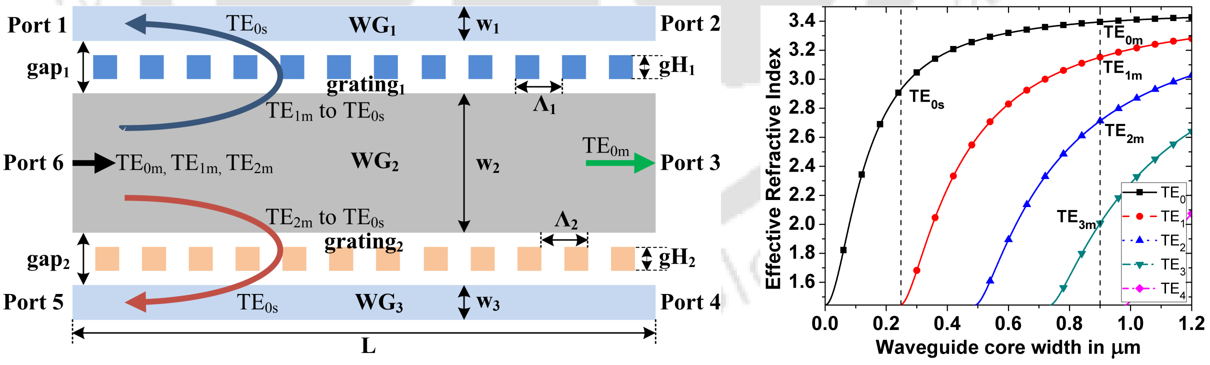

(a) (b)

Fig. 3.1: (a) Proposed device structure (b) Mode Chart of slab waveguide at 1550 nm wavelength.

Figure 3.1(a) shows the proposed device structure consisting of three waveguides (viz. WG_1, WG_2, and WG_3) and two gratings (viz. $grating_1$ and $grating_2$), where WG_1 and WG_3 support single mode and WG_2 supports multiple modes. The definitions of different symbols used in designing the proposed device structure is given in Table 3.1. Si and SiO_2 are the materials for waveguide core and cladding respectively. Si (SiO_2) has a refractive index of 3.473 (1.444) at

Table 3.1: Definition of Symbols

Symbol	Definition	Symbol	Definition	Symbol	Definition
w_1	Width of WG_1	gap_1	Gap between WG_1 and WG_2	Λ_2	Grating period of $grating_2$
w_2	Width of WG_2	gap_2	Gap between WG_2 and WG_3	gH_1	Grating width of $grating_1$
w_3	Width of WG_3	Λ_1	Grating period of $grating_1$	gH_2	Grating width of $grating_2$
N_{Λ_1}	Number of periods of $grating_1$	N_{Λ_2}	Number of periods of $grating_2$	L	Device length

a wavelength of 1550 nm [39, 175]. Figure 3.1(b) shows the mode chart of a slab waveguide as function of waveguide core width at 1550 nm wavelength. The width of the waveguides are selected such that WG_1 and WG_3 support only single TE mode (TE_{0s}) and WG_2 supports four TE modes (such as TE_{0m}, TE_{1m}, TE_{2m}, and TE_{3m}).

The proposed device is designed to demultiplex three TE modes simultaneously at 1550 nm, which is achieved when forward propagating TE_{1m} (TE_{2m}) couples to backward propagating TE_{0s} of WG_1 (WG_3). TE_{0m} keeps propagating in WG_2 as it is not coupled to any other mode at the operating wavelength. The contra-directional coupling between TE_{1m} (TE_{2m}) and TE_{0s} of WG_1 (WG_3) is realized by employing grating structure $grating_1$ ($grating_2$) with grating period Λ_1 (Λ_2) to satisfy the phase matching conditions given as [69]:

$$\beta_{1m} + \beta_{0s} = \frac{2\pi}{\Lambda_1} \tag{3.1}$$

$$\beta_{2m} + \beta_{0s} = \frac{2\pi}{\Lambda_2} \tag{3.2}$$

where β_{1m}, β_{2m}, and β_{0s} are propagation constants for TE_{1m}, TE_{2m}, and TE_{0s} respectively. The propagation constants of the different supported modes depend on the wavelength of light, thus for different operating wavelength the grating periods will vary as per Eqs. (3.1) and (3.2).

The width of the single mode waveguide is $w_1 = w_3 = 246$ nm and multimode waveguide is $w_2 = 900$ nm, as obtained from the mode chart shown in Figure 3.1(b). The width of the waveguide WG_2 is selected such that it supports four TE modes even though the MDM is designed for multiplexing/demultiplexing three channels. It is done so in order to have a considerable difference between the effective refractive indices of TE_{1m} and TE_{0s}. The effective refractive

Table 3.2: Supported Modes of the Waveguides

Waveguide	**Supported Modes**	**Effective Refractive Indices of the Modes**
WG_1	TE_{0s}	2.924
WG_2	TE_{0m}	3.395
	TE_{1m}	3.152
	TE_{2m}	2.713
	TE_{3m}	2.008
WG_3	TE_{0s}	2.924

indices of the modes supported by the three waveguides are listed in Table 3.2. The period of the gratings are found to be $\Lambda_1 = 255.10$ nm and $\Lambda_2 = 274.96$ nm using Eqs. (3.1) and (3.2) respectively.

3.2.2 Simulation Results

The proposed device has 6 ports as shown in Figure 3.1(a). TE_{0m}, TE_{1m}, and TE_{2m} are fed as inputs at Port 6. To determine the required gap between the waveguides (gap_1 and gap_2) which will ensure efficient coupling between TE_{1m} (TE_{2m}) and TE_{0s} of WG_1 (WG_3) with low return loss, the device structure is decomposed into two separate 4-port structures as shown in Figure 3.2(a) and 3.2(b).

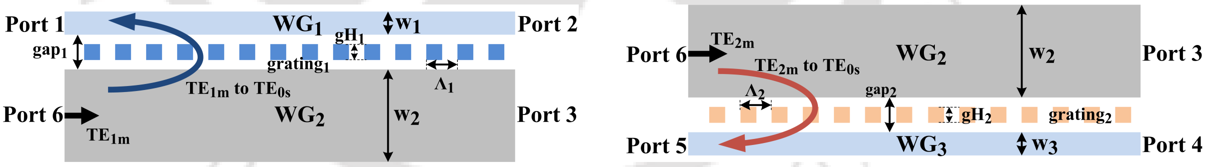

(a) (b)

Fig. 3.2: (a) 4-port structure with WG_1 and WG_2, (b) 4-port structure with WG_2 and WG_3.

When two waveguides are brought close to each other such that the mode of one waveguide penetrates into the other waveguide, the composite structure supports a new set of modes known as supermodes with different propagation constants and mode profiles as compared to the unperturbed isolated waveguides. The mode field profile and propagation constant of the supermode depend on spatial overlapping of the mode of one waveguide over the region where the other waveguide is present. When the separation distance between the two waveguides is decreased up to a certain distance at which isolated mode profile of one waveguide overlaps onto the other waveguide, the composite structure starts supporting supermode that contains power in both the waveguides.

Let the supermode supported by the composite structure is $E(x, y)$ with propagation constant β, then the field profile of the supermode can be written as [176]:

$$E(x, y) \approx E_1(x, y) + rE_2(x, y) \tag{3.3}$$

where $E_1(x, y)$ and $E_2(x, y)$ are the electric field mode profiles of the isolated unperturbed waveguides WG$_1$ and WG$_2$ respectively. r is the constant that can be calculated by solving the equations below [176]:

$$\frac{\kappa_{11} + r\kappa_{21}}{1 + rc} = \beta - \beta_1 \tag{3.4}$$

$$\frac{\kappa_{12} + r\kappa_{22}}{r + c} = \beta - \beta_2 \tag{3.5}$$

where β is the propagation constant of the supermode, β_1 (β_2) is the propagation constant of the supported eigenmode of the unperturbed waveguide WG$_1$ (WG$_2$). κ_{11}, κ_{12}, κ_{21}, κ_{22}, and c are defined as follows [69, 176]:

$$\kappa_{11} = \frac{\omega\epsilon_0}{4} \iint E_1^*(x, y)\ \Delta n_2^2(x, y)\ E_1(x, y)\ dx\, dy \tag{3.6}$$

$$\kappa_{12} = \frac{\omega\epsilon_0}{4} \iint E_1^*(x, y)\ \Delta n_1^2(x, y)\ E_2(x, y)\ dx\, dy \tag{3.7}$$

$$\kappa_{21} = \frac{\omega\epsilon_0}{4} \iint E_2^*(x, y)\ \Delta n_2^2(x, y)\ E_1(x, y)\ dx\, dy \tag{3.8}$$

$$\kappa_{22} = \frac{\omega\epsilon_0}{4} \iint E_2^*(x, y)\ \Delta n_1^2(x, y)\ E_2(x, y)\ dx\, dy \tag{3.9}$$

$$c = \iint E_1(x, y)\ E_2(x, y)\ dx\, dy \tag{3.10}$$

where ω is the optical frequency of operation and ϵ_0 is the permittivity of vacuum. Δn_1^2 and Δn_2^2 denote the presence of WG$_1$ and WG$_2$ respectively, having the value (n_{core}^2 - n_{clad}^2), where n_{core} = 3.473 and n_{clad} = 1.444.

Using Eqs. (3.4) and (3.5), propagation constants of the supermodes supported by the composite structure can be expressed as:

$$\beta = \left(\frac{\beta_1 + \beta_2}{2}\right) \pm \sqrt{\kappa_{12}\kappa_{21}\left[1 + \left(\frac{\beta_1 - \beta_2}{2\sqrt{\kappa_{12}\kappa_{21}}}\right)^2\right]} \tag{3.11}$$

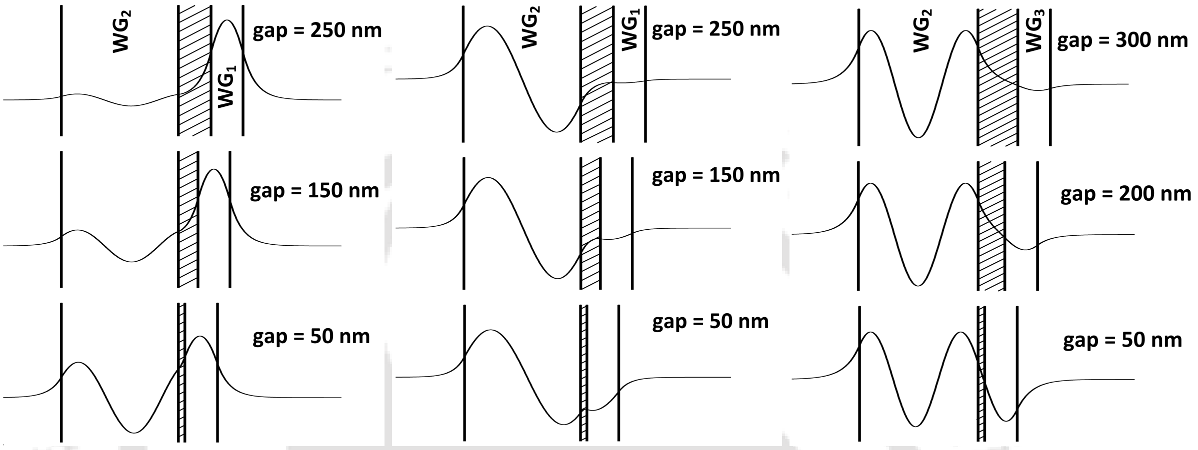

(a) (b) (c)

Fig. 3.3: Mode profile variation with gap for (a) TE_{0s}, (b) TE_{1m}, and (c) TE_{2m}; The dashed region represents the inter waveguide gap.

Figure 3.3(a), 3.10(d), and 3.3(c) show the variation of normalized electric field profile of TE_{0s}, TE_{1m}, and TE_{2m} modes at different gaps between the waveguides. It can be observed from Figure 3.3(a) that as the inter waveguide gap decreases, TE_{0s} mode power of WG_1 leaks into WG_2 which results in the formation of a supermode with different mode profile and effective refractive index. Similar observations can be seen for the TE_{1m} and TE_{2m} modes. The change in

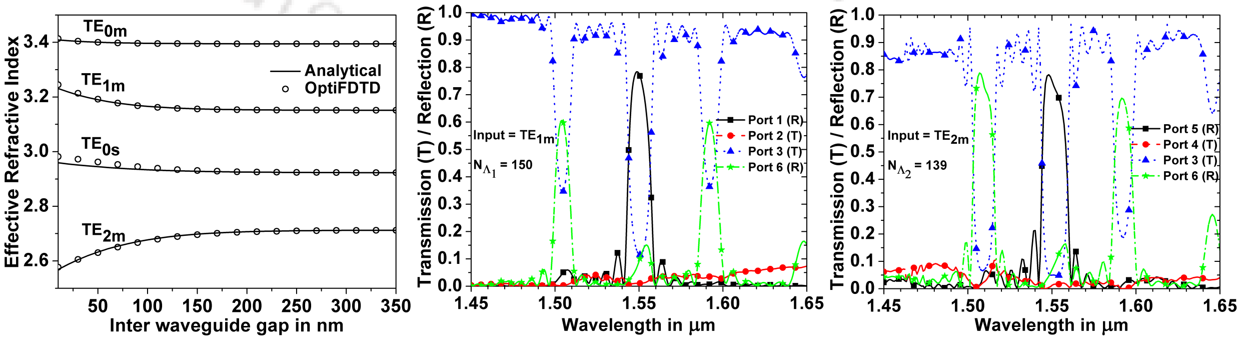

(a) (b) (c)

Fig. 3.4: (a) Variation of effective index of the supermode with change in inter waveguide gap, (b) Transmission and reflection spectrum of the 4-port structure with WG_1 and WG_2 for TE_{1m} input, (c) Transmission and reflection spectrum of the 4-port structure with WG_2 and WG_3 for TE_{2m} input; 'T' and 'R' represent transmission and reflection respectively.

effective refractive index of the modes with variation of inter waveguide gap is given in Figure 3.4(a). The separation distance between the waveguides below which the composite structure starts supporting supermode can be observed from the Figure 3.4(a) when the effective refractive index of the supported modes diverge from the effective refractive index of the isolated waveguide mode. The desired result for demultiplexing operation is to obtain TE_{0s} mode as reflection at Port 1 (Port 5) when TE_{1m} (TE_{2m}) is given as input at Port 6. Similarly for multiplexing operation, the desired result is to obtain TE_{1m} (TE_{2m}) as reflection at Port 6 when TE_{0s} is given as input at Port 1 (Port 5). Thus, to reduce reflection at the input port (return loss), the inter waveguide gap should be chosen in such a way that the reflected mode is confined to the target output waveguide with negligible mode confinement in the input waveguide. Considering this design condition, the gaps are chosen as gap_1 = 250 nm and gap_2 = 300 nm to minimize supermode formation. The number of grating periods of $grating_1$ (N_{Λ_1}) and $grating_2$ (N_{Λ_2}) are taken as 150 and 139 respectively in order to have same grating length and to obtain sufficient reflection. For undistored outputs, the widths of the gratings are taken as gH_1 = 125 nm and gH_2 = 150 nm. The 4-port structures shown in Figure 3.2(a) and 3.2(b) are simulated using 2D-FDTD. The transmission and reflection spectrum of the corresponding 4-port structures are shown in Figure 3.4(b) and Figure 3.4(c) for TE_{1m} and TE_{2m} input respectively. Coupling of TE_{1m} to TE_{0s} of WG_1 and TE_{2m} to TE_{0s} of WG_3 are observed as reflection peaks around 1550 nm.

The proposed device structure with 6 ports as shown in Figure 3.1(a) is numerically simulated using 2D-FDTD technique with all the design parameters obtained above. The length of the proposed device structure L is 38.5 μm. To examine the demultiplexing operation TE_{0m}, TE_{1m}, and TE_{2m} are given as inputs to Port 6 while transmission is observed at Port 2, 3, and 4 and reflection is monitored at Port 1, 5, and 6.

Figure 3.5(a) shows the transmission and reflection spectrum at the output ports when TE_{0m} is given as input to Port 6. It can be observed that the TE_{0m} propagates along the forward direction without being coupled to any other modes as there are no reflection peaks at the operating wavelength of 1550 nm. The TE_{1m} mode, when given as input, is coupled to backward prop-

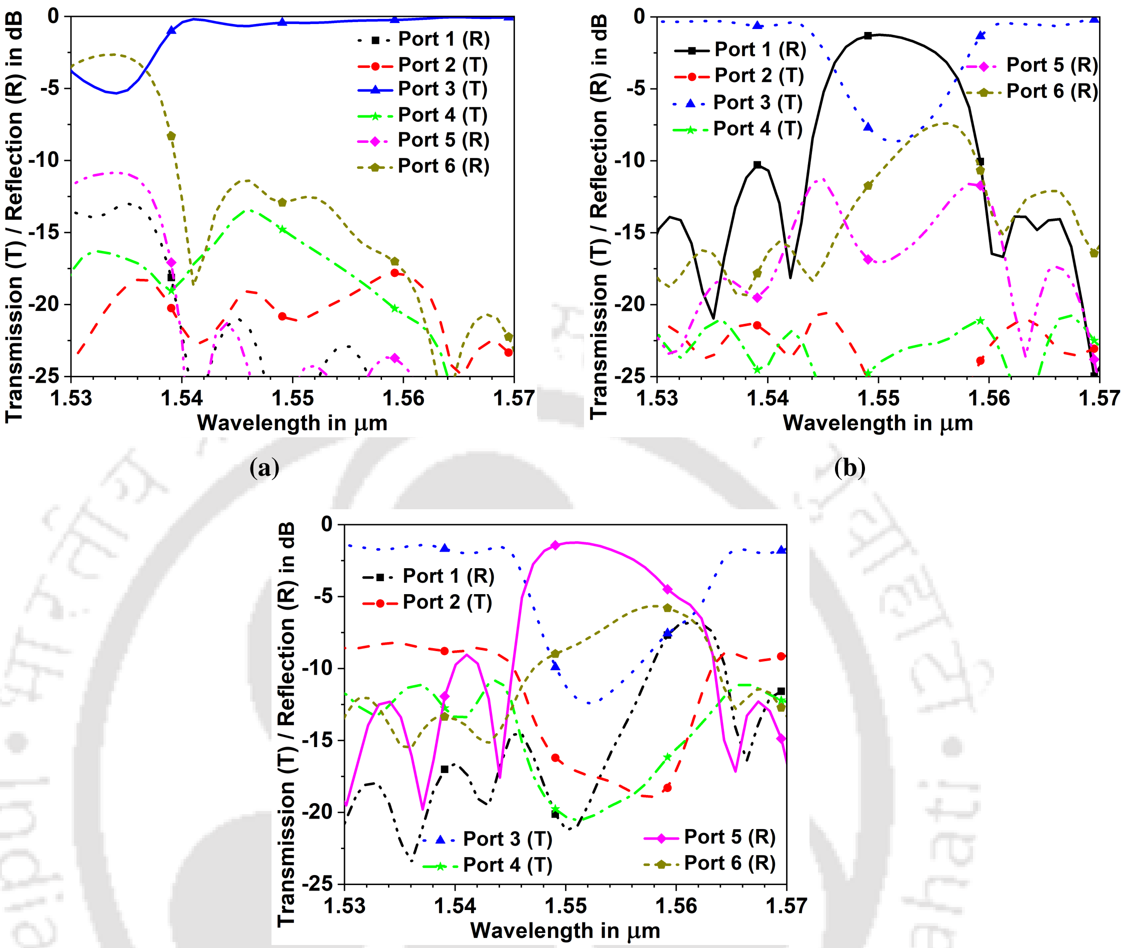

(a)

(b)

(c)

Fig. 3.5: (a) Transmission or Reflection at all ports when input is TE$_{0m}$, (b) Transmission or Reflection at all ports when input is TE$_{1m}$, (c) Transmission or Reflection at all ports when input is TE$_{2m}$

agating TE$_{0s}$ mode of WG$_1$ at Port 1, which is observed by the presence of reflection peak at 1550 nm from the Figure 3.5(b). Similarly, when TE$_{2m}$ is fed as input, it is coupled to the backward propagating TE$_{0s}$ mode of WG$_3$ at Port 5, which is confirmed by the presence of reflection peak at 1550 nm wavelength as shown in Figure 3.5(c). Crosstalks are calculated by observing output power at each of the ports for different input TE modes. When TE$_{1m}$ (TE$_{2m}$) is given as input at Port 6, due to the presence of grating$_1$ (grating$_2$) its power is coupled to TE$_{0s}$ of WG$_1$ (WG$_3$) propagating in the backward direction. In spite of the power coupling between the coupled modes, some of the mode power still remains in the multimode waveguide that propagates towards Port 3, this results in higher crosstalk at Port 3. Because of the supermode formation, for TE$_{1m}$ and TE$_{2m}$ inputs, some of the power is reflected in the input multimode waveguide which gives return loss. The resulting values of insertion loss and return loss are given in Table 3.3. The crosstalks at different output ports are shown in Table 3.4.

Table 3.3: Insertion loss and return loss during demultiplexing

Input Mode	Insertion Loss	Return Loss
TE_{0m}	0.43 dB	–12.73 dB
TE_{1m}	1.25 dB	–10.85 dB
TE_{2m}	1.27 dB	–8.65 dB

Table 3.4: Crosstalk during demultiplexing

Input Mode	Port 2	Port 1	Port 6	Port 5	Port 4
TE_{0m}	–31.20 dB	–21.13 dB	–	–15.31 dB	–25.80 dB
TE_{1m}	–	–27.14 dB	–8.38 dB	–23.97 dB	–27.09 dB
TE_{2m}	–21.24 dB	–16.80 dB	–11.31 dB	–20.34 dB	–

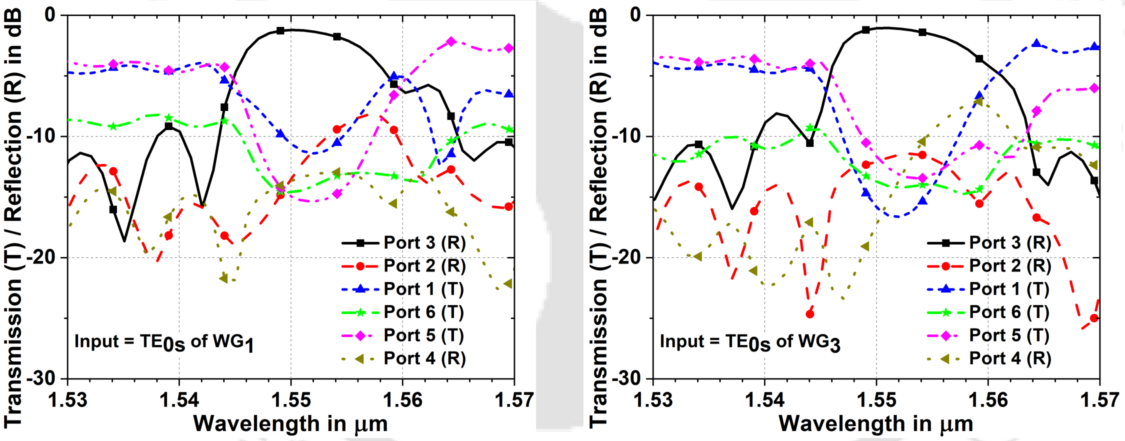

(a) (b)

Fig. 3.6: (a) Transmission or Reflection at all ports when input is TE_{0s} of WG_1 at Port 2, (b) Transmission or Reflection at all ports when input is TE_{0s} of WG_3 at Port 4

To investigate the multiplexing operation TE_{0s} of WG_1 and TE_{0s} of WG_3 are separately excited at Port 2 and Port 4 respectively. The resulting transmission/reflection spectrum at all the ports for each individual mode excitation has been shown in Fig. 3.6. In Fig. 3.6(a) it can be observed that, when TE_{0s} of WG_1 is excited at Port 2 to propagate along -z direction, its power is coupled to TE_{1m} in the +z direction which is shown as a reflection peak around 1550 nm at Port 3. Similarly, when TE_{0s} of WG_3 is excited at Port 4, a reflection peak at 1550 nm in the reflection spectrum of Port 3 is observed as shown in Fig. 3.6(b), indicating that its mode power is transferred to the TE_{2m} mode propagating in the +z direction.

The insertion loss and return loss exhibited by the proposed device structure is listed in Table 3.5, whereas Table 3.6 lists crosstalks occurred at other ports during the multiplexing operation.

Table 3.5: Insertion loss and return loss during multiplexing

Input Mode	Insertion Loss	Return Loss
TE_{0s} of WG_1	1.21 dB	–13.41 dB
TE_{0s} of WG_3	1.07 dB	–17.11 dB
TE_{0m}	0.43 dB	–12.73 dB

Table 3.6: Crosstalk during multiplexing

Input Mode	Port 2	Port 1	Port 6	Port 5	Port 4
TE_{0s} of WG_1	–	–10.66 dB	–14.62 dB	-14.99 dB	
TE_{0s} of WG_3	–12.05	–15.91 dB	–13.76 dB	–11.72 dB	–
TE_{0m}	–21.13 dB	–31.20 dB	–	–25.80 dB	–15.31 dB

3.2.3 Discussions

The proposed device structure is able to demultiplex three transverse electric modes by coupling forward propagating TE_{1m} (TE_{2m}) of WG_2 to backward propagating TE_{0s} of WG_1 (WG_3) and by keeping the fundamental mode TE_{0m} in WG_2. The return loss is mainly due to the formation of supermodes in the composite structure. It can be minimized by increasing the gap between the waveguides, but at the cost of device length, since a larger coupling length is required to reflect same amount of power for a particular grating width, and thus a trade off arises between return loss and the device length. In this work, crosstalks at Port 3 are not considered for performance analysis of the device as the crosstalk due to higher order mode inputs i.e. TE_{1m} and TE_{2m} can be reduced by connecting a single mode waveguide at Port 3 with an adiabatic taper which will eliminate the higher order modes and only keep the required fundamental mode [177]. The insertion loss of the proposed device structure ranges from 0.43 to 1.27 dB during the demultiplexing operation and 0.43 to 1.21 dB during the multiplexing operation, which is better as compared to 0.2 to 6.6 dB in [177] for the three TE mode case, whereas the crosstalk is comparable in the range of –31.20 to –15.31 dB. The conventional method of cascading grating structures one after another for the multiplexing purpose [149] where power of the different modes of the multimode waveguide are reflected with the use of different gratings placed consecutively in a cascaded arrangement thereby the device length increases. However, in the proposed device structure, gratings are placed on both sides of the multimode waveguide which reflect two modes simultaneously and thus helps in reducing the overall device length.

3.2.4 Conclusions

A grating assisted slab waveguide structure has been designed to (de)multiplex three TE modes at a wavelength of 1550 nm . Two gratings with different periods have been placed at both sides of the multimode waveguide to contra-directionally couple first order and second order modes to the fundamental mode of two single mode waveguides. The fundamental mode of the multimode waveguide is not coupled to any other mode. The waveguide widths are obtained from the mode chart and the inter waveguide gaps have been determined such that return loss is minimized, which occurs mainly due to the supermode formation. During demultiplexing (multiplexing) operation, the proposed device structure has shown insertion loss ranging from 0.43 to 1.27 dB (0.43 to 1.21 dB), return loss from –12.73 to –8.65 dB (–17.11 to –12.73 dB), and crosstalk from –31.20 to –15.31 dB (–31.20 to –10.66 dB) with a device length of 38.5 μm. This mode-division multiplexer can be integrated with polarization division multiplexer or wavelength division multiplexer for further increase in the link capacity.

3.3 TM mode-division (de)multiplexer

Similar to the TE mode-division (de)multiplexer, a slab waveguide based TM mode-division (de)multiplexer with Si core and SiO_2 cladding is proposed. The device is able to (de)multiplex three transverse magnetic (TM) modes at 1550 nm. The (de)multiplexing operation is ensured by coupling the higher order multimode waveguide modes to the fundamental modes of two single-mode waveguides through grating structures that are placed at each side of the multimode waveguide. It simultaneously reflects two higher-order modes when it works as a demultiplexer and combines them during multiplexing, whereas the fundamental mode of the multimode waveguide continues forward propagation in the same waveguide since it is not coupled to any other mode. The aspect of supermodes for determining the suitable gap between the waveguides has been introduced to minimize the return loss. The dimension of the proposed MDM device has been found to be compact compared to the PLC-based mode-division multiplexers [178, 179]. The performance analysis of the device is carried out numerically using 2D Finite Difference Time Domain (2D FDTD). The bi-directional characteristic of the proposed device has been validated by demonstrating both the demultiplexing and multiplexing operations.

3.3.1 Proposed Device Structure and Mathematical Model

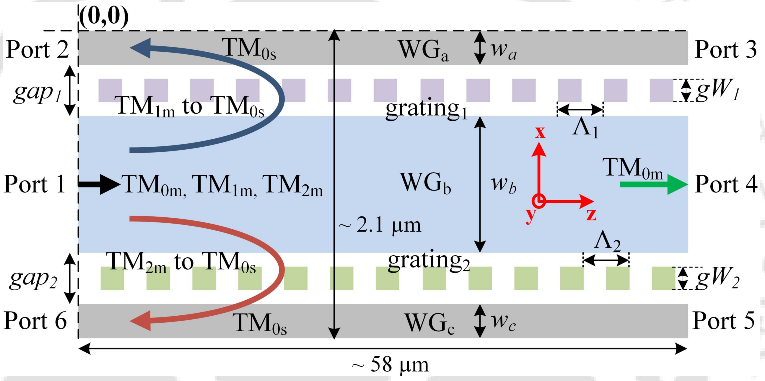

Fig. 3.7: Schematic diagram of the proposed MDM structure

The schematic diagram of the proposed MDM structure is shown in Fig. 3.7, which is designed using slab waveguides. The device is comprised of two single mode waveguides (WG$_a$ and WG$_c$) and one multimode waveguide (WG$_b$). The width of waveguides WG$_a$, WG$_b$, and WG$_c$ are denoted as w_a, w_b, and w_c respectively. grating$_1$ (grating$_2$) is a grating structure placed in the gap between WG$_a$ and WG$_b$ (WG$_b$ and WG$_c$), denoted as gap_1 (gap_2) with grating period Λ_1 (Λ_2) and number of grating periods N_{Λ_1} (N_{Λ_2}). gW_1 and gW_2 are the widths of grating$_1$ and grating$_2$ respectively. The multimode waveguide WG$_b$ supports three modes namely TM$_{0m}$ (fundamental mode), TM$_{1m}$ (first order mode), and TM$_{2m}$ (second order mode), whereas WG$_a$ and WG$_c$ are two identical waveguides each supporting a single mode denoted as TM$_{0s}$ (fundamental mode).

The proposed MDM structure shown in Fig. 3.7 has 6 ports, out of which Port 1 acts as the input port where TM$_{0m}$, TM$_{1m}$, and TM$_{2m}$ are fed by exciting each mode separately. TM$_{1m}$ (TM$_{2m}$) is coupled as contra-propagating TM$_{0s}$ in WG$_a$ (WG$_c$) at Port 2 (Port 6), using grating$_1$

(grating$_2$). The fundamental mode of the multimode waveguide TM$_{0m}$ propagates towards Port 4 as it is not coupled to any other waveguide modes. Thus, (de)multiplexing of two higher-order modes and a fundamental mode is realized.

Refractive index profile of the proposed structure shown in Fig. 3.7 is defined as [69]:

$$\epsilon(x) = \epsilon_0[n_{clad}^2 + \Delta n_a^2(x) + \Delta n_b^2(x) + \Delta n_c^2(x) + \Delta n_{\Lambda_1}^2(x) + \Delta n_{\Lambda_2}^2(x)] \tag{3.12}$$

where

$$\Delta n_a^2(x) = \begin{cases} n_{core}^2 - n_{clad}^2, & \text{waveguide } \ WG_a \\ 0, & \text{elsewhere} \end{cases} \tag{3.13}$$

$$\Delta n_b^2(x) = \begin{cases} n_{core}^2 - n_{clad}^2, & \text{waveguide } \ WG_b \\ 0, & \text{elsewhere} \end{cases} \tag{3.14}$$

$$\Delta n_c^2(x) = \begin{cases} n_{core}^2 - n_{clad}^2, & \text{waveguide } \ WG_c \\ 0, & \text{elsewhere} \end{cases} \tag{3.15}$$

$$\Delta n_{\Lambda_1}^2(x) = \begin{cases} (n_{core}^2 - n_{clad}^2) \times S_1(z), & \text{grating}_1 \\ 0, & \text{elsewhere} \end{cases} \tag{3.16}$$

$$\Delta n_{\Lambda_2}^2(x) = \begin{cases} (n_{core}^2 - n_{clad}^2) \times S_2(z), & \text{grating}_2 \\ 0, & \text{elsewhere} \end{cases} \tag{3.17}$$

where

$$S_1(z) = \sum_{p=-\infty}^{\infty} e^{ip\pi/2}\Big[\frac{sin(p\pi/2)}{p\pi}\Big]e^{-ip(2\pi/\Lambda_1)z} \tag{3.18}$$

$$S_2(z) = \sum_{q=-\infty}^{\infty} e^{iq\pi/2}\Big[\frac{sin(q\pi/2)}{q\pi}\Big]e^{-iq(2\pi/\Lambda_2)z} \tag{3.19}$$

Here $\Delta n_a^2(x)$, $\Delta n_b^2(x)$, $\Delta n_c^2(x)$, $\Delta n_{\Lambda_1}^2(x)$, and $\Delta n_{\Lambda_2}^2(x)$ represent the presence of WG$_a$, WG$_b$, WG$_c$, grating$_1$, and grating$_2$ respectively. The refractive indices of core and cladding are denoted as n_{core} and n_{clad}.

Let the y directed magnetic field profiles of the modes supported by the three unperturbed waveguides WG$_a$, WG$_b$, and WG$_c$ are denoted as: $H_{ya}(x)$ (fundamental mode TM$_{0s}$ of WG$_a$), $H_{yb_0}(x)$ (fundamental mode TM$_{0m}$ of WG$_b$), $H_{yb_1}(x)$ (1st order mode TM$_{1m}$ of WG$_b$), $H_{yb_2}(x)$ (2nd order mode TM$_{2m}$ of WG$_b$), and $H_{yc}(x)$ (fundamental mode TM$_{0s}$ of WG$_c$).

The magnetic field in the proposed device structure can be expressed in terms of unperturbed waveguide modes as:

$$\begin{aligned} H_y(x,z,t) = A^+(z)H_{ya}(x)e^{j(\omega t-\beta_{0s}z)} + \sum_{r=0}^{2} B_r^+(z)H_{yb_r}(x)e^{j(\omega t-\beta_{rm}z)} + \\ C^+(z)H_{yc}(x)e^{j(\omega t-\beta_{0s}z)} + A^-(z)H_{ya}(x)e^{j(\omega t+\beta_{0s}z)} + \\ \sum_{r=0}^{2} B_r^-(z)H_{yb_r}(x)e^{j(\omega t+\beta_{rm}z)} + C^-(z)H_{yc}(x)e^{j(\omega t+\beta_{0s}z)} \end{aligned} \tag{3.20}$$

where $A(z)$, $B_r(z)$, and $C(z)$ are the z dependent amplitudes of the corresponding modes. The signs $^+$ and $^-$ denote forward and backward propagation in the z direction respectively. β_{0s} is the propagation constant of the fundamental mode of WG$_a$, WG$_c$ and β_{rm} is the propagation constant of the r^{th} mode of WG$_b$.

$H_{ya}(x)$, $H_{yb_r}(x)$, and $H_{yc}(x)$ are normalized such that each of them contains 1 W power, i.e. [180]:

$$\int_{-\infty}^{\infty} \frac{|H_{ya}(x)|^2}{n_{clad}^2 + \Delta n_a^2(x)} dx = \frac{2\omega\epsilon_0}{\beta_{0s}} \tag{3.21}$$

$$\int_{-\infty}^{\infty} \frac{|H_{yb_r}(x)|^2}{n_{clad}^2 + \Delta n_b^2(x)} dx = \frac{2\omega\epsilon_0}{\beta_{rm}}, \quad r = 0, 1, 2 \tag{3.22}$$

$$\int_{-\infty}^{\infty} \frac{|H_{yc}(x)|^2}{n_{clad}^2 + \Delta n_c^2(x)} dx = \frac{2\omega\epsilon_0}{\beta_{0s}} \tag{3.23}$$

3.3.1.1 Mode Profiles

The magnetic field mode profiles supported by the three waveguides are expressed as [181]:

$$H_{ya}(x) = \begin{cases} P_a e^{-\gamma_{ea}x}, \; x > 0 \\ P_a m_{1a}(x), \; -w_a < x < 0 \\ P_a m_{2a}(w_a) e^{\gamma_{ea}(x+w_a)}, \; x < -w_a \end{cases} \tag{3.24}$$

$$H_{yb_r}(x) = \begin{cases} P_{b_r} e^{-\gamma_{eb_r}(x+k)}, \; x > -k, \\ P_{b_r} m_{1b}(x), \; -k < x < -(k+w_b) \\ P_{b_r} m_{2b}(w_b) e^{\gamma_{eb_r}(x+k+w_b)}, \; x < -(k+w_b) \end{cases} \tag{3.25}$$

$$H_{yc}(x) = \begin{cases} P_c e^{-\gamma_{ec}(x+l)}, \; x > -l, \\ P_c m_{1c}(x), \; -l < x < -(l+w_c) \\ P_c m_{2c}(w_c) e^{\gamma_{ec}(x+l+w_c)}, \; x < -(l+w_c) \end{cases} \tag{3.26}$$

where

$$m_{1a}(x) = cos(\gamma_{fa}x) - \frac{\gamma_{ea}}{\gamma_{fa}} \frac{n_{core}^2}{n_{clad}^2} sin(\gamma_{fa}x) \tag{3.27}$$

$$m_{2a}(x) = cos(\gamma_{fa}x) + \frac{\gamma_{ea}}{\gamma_{fa}} \frac{n_{core}^2}{n_{clad}^2} sin(\gamma_{fa}x) \tag{3.28}$$

$$m_{1b}(x) = cos(\gamma_{fb_r}(x+k)) - \frac{\gamma_{eb_r}}{\gamma_{fb_r}} \frac{n_{core}^2}{n_{clad}^2} sin(\gamma_{fb_r}(x+k)) \tag{3.29}$$

$$m_{2b}(x) = cos(\gamma_{fb_r}x) + \frac{\gamma_{eb_r}}{\gamma_{fb_r}} \frac{n_{core}^2}{n_{clad}^2} sin(\gamma_{fb_r}x) \tag{3.30}$$

$$m_{1c}(x) = cos(\gamma_{fc}(x+l)) - \frac{\gamma_{ec}}{\gamma_{fc}} \frac{n_{core}^2}{n_{clad}^2} sin(\gamma_{fc}(x+l)) \tag{3.31}$$

$$m_{2c}(x) = cos(\gamma_{fc}x) + \frac{\gamma_{ec}}{\gamma_{fc}} \frac{n_{core}^2}{n_{clad}^2} sin(\gamma_{fc}x) \tag{3.32}$$

where

$$k = w_a + gap_1, \; l = w_a + w_b + gap_1 + gap_2, \; r = 0, \; 1, \; 2$$

$$
\begin{aligned}
\gamma_{ea},\ \gamma_{ec} &= \sqrt{\beta_{0s}^2 - \Big(\frac{2\pi n_{clad}}{\lambda_0}\Big)^2} \\
\gamma_{fa},\ \gamma_{fc} &= \sqrt{\Big(\frac{2\pi n_{core}}{\lambda_0}\Big)^2 - \beta_{0s}^2} \\
\gamma_{eb_r}\Big|_{r=0,1,2} &= \sqrt{\beta_{rm}^2 - \Big(\frac{2\pi n_{clad}}{\lambda_0}\Big)^2} \\
\gamma_{fb_r}\Big|_{r=0,1,2} &= \sqrt{\Big(\frac{2\pi n_{core}}{\lambda_0}\Big)^2 - \beta_{rm}^2}
\end{aligned}
$$

Here, λ_0 is the operating wavelength. P_a, P_{b_0}, P_{b_1}, P_{b_2}, and P_c represent the magnitude of the mode profiles which are defined as [69]:

$$
P_u\Big|_{u=a,b_r,c} = 2 \times \sqrt{\frac{\omega\epsilon_0}{\beta_u t_u}},\ r = 0, 1, 2 \tag{3.33}
$$

where

$$
t_u\Big|_{u=a,b_r,c} = \frac{\{(\frac{n_{core}}{n_{clad}})^2\gamma_{eu}\}^2 + \gamma_{fu}^2}{\{(\frac{n_{core}}{n_{clad}})^2\gamma_{eu}\}^2} \times \Big[\frac{w_u}{n_{clad}^2} + \frac{\gamma_{eu}^2 + \gamma_{fu}^2}{\{(\frac{n_{core}}{n_{clad}})^2\gamma_{eu}\}^2 + \gamma_{fu}^2}\Big],\ w_{b_r} = w_b,\ r = 0, 1, 2 \tag{3.34}
$$

3.3.1.2 Coupled Mode Equations

To analyze the light propagation in the proposed device, coupled-mode theory has been used. By using coupled-mode analysis, the coupling between different modes in the composite structure has been investigated including all the phase mismatched terms. The coupled-mode equations for the proposed device shown in Fig. 3.7 are given as:

$$
\frac{\partial A^+}{\partial z} = -j[A^+(z)\kappa_{aa} + A^-(z)\kappa_{aa}e^{j2\beta_{0s}z} + \sum_{r=0}^{2} B_r^+(z)\kappa_{ab_r}e^{j(\beta_{0s}-\beta_{rm})z} + \sum_{r=0}^{2} B_r^-(z)\kappa_{ab_r}e^{j(\beta_{0s}+\beta_{rm})z} + C^+(z)\kappa_{ac} + C^-(z)\kappa_{ac}e^{j2\beta_{0s}z}] \tag{3.35}
$$

$$\left.\frac{\partial B_r^+}{\partial z}\right|_{r=0,1,2} = -j[A^+(z)\kappa_{b_r a}e^{j(\beta_{rm}-\beta_{0s})z} + A^-(z)\kappa_{b_r a}e^{j(\beta_{rm}+\beta_{0s})z} + \\ \sum_{p=0}^{2} B_p^+(z)\kappa_{b_r b_p}e^{j(\beta_{rm}-\beta_{pm})z} + \sum_{p=0}^{2} B_p^-(z)\kappa_{b_r b_p}e^{j(\beta_{rm}+\beta_{pm})z} + \\ C^+(z)\kappa_{b_r c}e^{j(\beta_{rm}-\beta_{0s})z} + C^-(z)\kappa_{b_r c}e^{j(\beta_{rm}+\beta_{0s})z}] \quad (3.36)$$

$$\frac{\partial C^+}{\partial z} = -j[A^+(z)\kappa_{ca} + A^-(z)\kappa_{ca}e^{j2\beta_{0s}z} + \sum_{r=0}^{2} B_r^+(z)\kappa_{cb_r}e^{j(\beta_{0s}-\beta_{rm})z} + \\ \sum_{r=0}^{2} B_r^-(z)\kappa_{cb_r}e^{j(\beta_{0s}+\beta_{rm})z} + C^+(z)\kappa_{cc} + C^-(z)\kappa_{cc}e^{j2\beta_{0s}z}] \quad (3.37)$$

$$\frac{\partial A^-}{\partial z} = j[A^+(z)\kappa_{aa}e^{-j2\beta_{0s}z} + A^-(z)\kappa_{aa} + \sum_{r=0}^{2} B_r^+(z)\kappa_{ab_r}e^{-j(\beta_{0s}+\beta_{rm})z} + \\ \sum_{r=0}^{2} B_r^-(z)\kappa_{ab_r}e^{-j(\beta_{0s}-\beta_{rm})z} + C^+(z)\kappa_{ac}e^{-j2\beta_{0s}z} + C^-(z)\kappa_{ac}] \quad (3.38)$$

$$\left.\frac{\partial B_r^-}{\partial z}\right|_{r=0,1,2} = j[A^+(z)\kappa_{b_r a}e^{-j(\beta_{rm}+\beta_{0s})z} + A^-(z)\kappa_{b_r a}e^{-j(\beta_{rm}-\beta_{0s})z} + \\ \sum_{p=0}^{2} B_p^+(z)\kappa_{b_r b_p}e^{-j(\beta_{rm}+\beta_{pm})z} + \sum_{p=0}^{2} B_p^-(z)\kappa_{b_r b_p}e^{-j(\beta_{rm}-\beta_{pm})z} + \\ C^+(z)\kappa_{b_r c}e^{-j(\beta_{rm}+\beta_{0s})z} + C^-(z)\kappa_{b_r c}e^{j-(\beta_{rm}-\beta_{0s})z}] \quad (3.39)$$

$$\frac{\partial C^-}{\partial z} = j[A^+(z)\kappa_{ca}e^{-j2\beta_{0s}z} + A^-(z)\kappa_{ca} + \sum_{r=0}^{2} B_r^+(z)\kappa_{cb_r}e^{-j(\beta_{0s}+\beta_{rm})z} + \\ \sum_{r=0}^{2} B_r^-(z)\kappa_{cb_r}e^{-j(\beta_{0s}-\beta_{rm})z} + C^+(z)\kappa_{cc}e^{-j2\beta_{0s}z} + C^-(z)\kappa_{cc}] \quad (3.40)$$

where κ_{aa}, κ_{ab_r}, κ_{ac}, $\kappa_{b_r a}$, $\kappa_{b_r b_p}$, $\kappa_{b_r c}$, κ_{ca}, κ_{cb_r}, and κ_{cc} are the coupling coefficients, expressed as:

$$\kappa_{ua}\Big|_{u=a,b_r,c} = \frac{\omega\mu_0}{4}\int_{-\infty}^{\infty}\frac{H_{ya}(x)H_{yu}^*(x)}{n_{clad}^2+\Delta n_u^2(x)}\{\Delta n_b^2(x)+ \Delta n_{\Lambda_1}^2(x)+\Delta n_c^2(x)+\Delta n_{\Lambda_2}^2(x)\}dx,\ r=0,1,2 \quad (3.41)$$

$$\kappa_{ub_p}\Big|_{u=a,b_r,c} = \frac{\omega\mu_0}{4}\int_{-\infty}^{\infty}\frac{H_{yb_r}(x)H_{yu}^*(x)}{n_{clad}^2+\Delta n_u^2(x)}\{\Delta n_a^2(x)+ \Delta n_{\Lambda_1}^2(x)+\Delta n_c^2(x)+\Delta n_{\Lambda_2}^2(x)\}dx,\ r,p=0,1,2 \quad (3.42)$$

$$\kappa_{uc}\Big|_{u=a,b_r,c} = \frac{\omega\mu_0}{4}\int_{-\infty}^{\infty}\frac{H_{yc}(x)H_{yu}^*(x)}{n_{clad}^2+\Delta n_u^2(x)}\{\Delta n_a^2(x)+ \Delta n_{\Lambda_1}^2(x)+\Delta n_b^2(x)+\Delta n_{\Lambda_2}^2(x)\}dx,\ r=0,1,2 \quad (3.43)$$

Here, $\Delta n_{b_r}^2(x) = \Delta n_b^2(x)$ for $r = 0, 1, 2$. The integration terms for different regions are defined as:

$$\int\limits_{-(w_a+w_b+gap_1)}^{-(w_a+gap_1)} |H_{ya}(x)|^2dx = P_a^2\{cos(\gamma_{fa}w_a)+\frac{\gamma_{ea}}{\gamma_{fa}}\frac{n_{core}^2}{n_{clad}^2}sin(\gamma_{fa}w_a)\}^2\times \frac{1}{2\gamma_{ea}}e^{-2\gamma_{ea}gap_1}(1-e^{-2\gamma_{ea}w_b}) \quad (3.44)$$

$$\int\limits_{-(w_a+gap_1/2+gW_1/2)}^{-(w_a+gap_1/2-gW_1/2)} |H_{ya}(x)|^2dx = P_a^2\{cos(\gamma_{fa}w_a)+\frac{\gamma_{ea}}{\gamma_{fa}}\frac{n_{core}^2}{n_{clad}^2}sin(\gamma_{fa}w_a)\}^2\times \frac{1}{2\gamma_{ea}}e^{-\gamma_{ea}(gap_1-gW_1)}(1-e^{-\gamma_{ea}gW_1}) \quad (3.45)$$

$$\int_{-(w_a+gap_1/2+gW_1/2)}^{-(w_a+gap_1/2-gW_1/2)} H_{yb_r}(x)H_{ya}^*(x)dx\Big|_{r=0,1,2} = P_aP_{b_r}\{cos(\gamma_{fa}w_a)+ \frac{\gamma_{ea}}{\gamma_{fa}}\frac{n_{core}^2}{n_{clad}^2}sin(\gamma_{fa}w_a)\}^2 \times \frac{e^{\gamma_{ea}w_a-\gamma_{eb_r}(w_a+gap_1)}}{\gamma_{ea}-\gamma_{eb_r}}\times e^{-(\gamma_{ea}-\gamma_{eb_r})(w_a+gap_1/2-gW_1/2)} \times \{1-e^{-(\gamma_{ea}-\gamma_{eb_r})gW_1}\} \tag{3.46}$$

$$\int_{-w_a}^{0} |H_{yb_r}(x)|^2dx\Big|_{r=0,1,2} = P_{b_r}^2\{\frac{e^{-2\gamma_{eb_r}(w_a+gap_1)}}{(-2\gamma_{eb_r})}\}(1 - e^{2\gamma_{eb_r}w_a}) \tag{3.47}$$

$$\int_{-(w_a+w_b+gap_1+gap_2)}^{-(w_a+w_b+w_c+gap_1+gap_2)} |H_{yb_r}(x)|^2dx\Big|_{r=0,1,2} = P_{b_r}^2\{cos(\gamma_{fa}w_b)+ \frac{\gamma_{eb_r}}{\gamma_{fb_r}}\frac{n_{core}^2}{n_{clad}^2}sin(\gamma_{fa}w_b)\}^2 \times \frac{e^{-2\gamma_{eb_r}gap_2}}{2\gamma_{eb_r}}(1-e^{-2\gamma_{eb_r}w_c}) \tag{3.48}$$

$$\int_{-(w_a+gap_1/2+gW_1/2)}^{-(w_a+gap_1/2-gW_1/2)} |H_{yb_r}(x)|^2dx\Big|_{r=0,1,2} = P_{b_r}^2\{\frac{e^{-2\gamma_{eb_r}(gap_1/2+gW_1/2)}}{(2\gamma_{eb_r})}\}\times (e^{2\gamma_{eb_r}gW_1}-1) \tag{3.49}$$

$$\int_{-(w_a+gap_1+w_b+gap_2/2+gW_2/2)}^{-(w_a+gap_1+w_b+gap_2/2-gW_2/2)} |H_{yb_r}(x)|^2dx\Big|_{r=0,1,2} = P_{b_r}^2\{cos(\gamma_{fa}w_b)+ \frac{\gamma_{eb_r}}{\gamma_{fb_r}}\frac{n_{core}^2}{n_{clad}^2}sin(\gamma_{fa}w_b)\}^2 \times \frac{1}{2\gamma_{eb_r}}\times e^{-2\gamma_{eb_r}(gap_2/2-gW_2/2)}\{1-e^{-2\gamma_{eb_r}gW_2}\} \tag{3.50}$$

$$\int_{-(w_a+w_b+gap_1)}^{-(w_a+gap_1)} |H_{yc}(x)|^2 dx = \frac{P_c^2}{2\gamma_{ec}} e^{-2\gamma_{ec}(w_b+gap_2)} \times (e^{2\gamma_{ec}w_b} - 1) \tag{3.51}$$

$$\int_{-(w_a+gap_1+w_b+gap_2/2+gW_2/2)}^{-(w_a+gap_1+w_b+gap_2/2-gW_2/2)} |H_{yc}(x)|^2 dx = \frac{P_c^2}{2\gamma_{ec}} e^{-\gamma_{ec}(\frac{3gap_2}{2}+\frac{gW_2}{2})}(e^{2\gamma_{ec}gW_2} - 1) \tag{3.52}$$

$$\int_{-(w_a+w_b+gap_1+gap_2)}^{-(w_a+w_b+w_c+gap_1+gap_2)} |H_{ya}(x)|^2 dx = 0 \tag{3.53}$$

$$\int_{-(w_a+gap_1+w_b+gap_2/2+gW_2/2)}^{-(w_a+gap_1+w_b+gap_2/2-gW_2/2)} |H_{ya}(x)|^2 dx = 0 \tag{3.54}$$

$$\int_{-(w_a+gap_1/2+gW_1/2)}^{-(w_a+gap_1/2-gW_1/2)} |H_{yc}(x)|^2 dx = 0 \tag{3.55}$$

$$\int_{-w_a}^{0} |H_{yc}(x)|^2 dx = 0 \tag{3.56}$$

$$\begin{aligned}\int_{-(w_a+gap_1+w_b+gap_2/2+gW_2/2)}^{-(w_a+gap_1+w_b+gap_2/2-gW_2/2)} H_{yb_r}(x)H_{yc}^*(x)dx = P_{b_r}P_c\{cos(\gamma_{fb_r}w_b)+ \\ \frac{\gamma_{eb_r}}{\gamma_{fb_r}}\frac{n_{core}^2}{n_{clad}^2}sin(\gamma_{fb_r}w_b)\} \times \frac{e^{-\gamma_{ec}gap_2}}{\gamma_{eb_r}-\gamma_{ec}} \times e^{-(\gamma_{eb_r}-\gamma_{ec})(\frac{gap_2-gW_2}{2})} \times \\ \{1-e^{-(\gamma_{eb_r}-\gamma_{ec})gW_2}\}, r = 0, 1, 2\end{aligned} \tag{3.57}$$

In (3.42)–(3.45), the integration terms are zero as the mode profiles do not have any magnetic field components in the corresponding spatial regions. To obtain a solution, the coupled-mode equations can be converted into a form of linear differential equations by assuming the following:

$$
\begin{aligned}
A^{+}(z)e^{-j\beta_{0s}z} &= q_1(z), & B_0^{+}(z)e^{-j\beta_{0m}z} &= q_2(z),\\
B_1^{+}(z)e^{-j\beta_{1m}z} &= q_3(z), & B_2^{+}(z)e^{-j\beta_{2m}z} &= q_4(z),\\
D^{+}(z)e^{-j\beta_{0s}z} &= q_5(z), & A^{-}(z)e^{j\beta_{0s}z} &= q_6(z),\\
B_0^{-}(z)e^{j\beta_{0m}z} &= q_7(z), & B_1^{-}(z)e^{j\beta_{1m}z} &= q_8(z),\\
B_2^{-}(z)e^{j\beta_{2m}z} &= q_9(z), & D^{-}(z)e^{j\beta_{0s}z} &= q_{10}(z)
\end{aligned}
$$

The corresponding linear differential equations are expressed in the matrix form as:

$$\frac{dQ}{dz} = K\,Q \tag{3.58}$$

where

$$Q = \begin{bmatrix} q_1 & q_2 & q_3 & q_4 & q_5 & q_6 & q_7 & q_8 & q_9 & q_{10} \end{bmatrix}^T \tag{3.59}$$

and

K is the matrix comprised of all the coupling coefficients, expressed as:

$$K = \begin{bmatrix}
\kappa_{aa} - j\beta_{0s} & \kappa_{ab_0} & \kappa_{ab_1} & \kappa_{ab_2} & \kappa_{ac} & \kappa_{aa} & \kappa_{ab_0} & \kappa_{ab_1} & \kappa_{ab_2} & \kappa_{ac}\\
\kappa_{b_0a} & \kappa_{b_0b_0} - j\beta_{0m} & \kappa_{b_0b_1} & \kappa_{b_0b_2} & \kappa_{b_0c} & \kappa_{b_0a} & \kappa_{b_0b_0} & \kappa_{b_0b_1} & \kappa_{b_0b_2} & \kappa_{b_0c}\\
\kappa_{b_1a} & \kappa_{b_1b_0} & \kappa_{b_1b_1} - j\beta_{1m} & \kappa_{b_1b_2} & \kappa_{b_1c} & \kappa_{b_1a} & \kappa_{b_1b_0} & \kappa_{b_1b_1} & \kappa_{b_1b_2} & \kappa_{b_1c}\\
\kappa_{b_2a} & \kappa_{b_2b_0} & \kappa_{b_2b_1} & \kappa_{b_2b_2} - j\beta_{2m} & \kappa_{b_2c} & \kappa_{b_2a} & \kappa_{b_2b_0} & \kappa_{b_2b_1} & \kappa_{b_2b_2} & \kappa_{b_2c}\\
\kappa_{ca} & \kappa_{cb_0} & \kappa_{cb_1} & \kappa_{cb_2} & \kappa_{cc} - j\beta_{0s} & \kappa_{ca} & \kappa_{cb_0} & \kappa_{cb_1} & \kappa_{cb_2} & \kappa_{cc}\\
\kappa_{aa} & \kappa_{ab_0} & \kappa_{ab_1} & \kappa_{ab_2} & \kappa_{ac} & \kappa_{aa} + j\beta_{0s} & \kappa_{ab_0} & \kappa_{ab_1} & \kappa_{ab_2} & \kappa_{ac}\\
\kappa_{b_0a} & \kappa_{b_0b_0} & \kappa_{b_0b_1} & \kappa_{b_0b_2} & \kappa_{b_0c} & \kappa_{b_0a} & \kappa_{b_0b_0} + j\beta_{0m} & \kappa_{b_0b_1} & \kappa_{b_0b_2} & \kappa_{b_0c}\\
\kappa_{b_1a} & \kappa_{b_1b_0} & \kappa_{b_1b_1} & \kappa_{b_1b_2} & \kappa_{b_1c} & \kappa_{b_1a} & \kappa_{b_1b_0} & \kappa_{b_1b_1} + j\beta_{1m} & \kappa_{b_1b_2} & \kappa_{b_1c}\\
\kappa_{b_2a} & \kappa_{b_2b_0} & \kappa_{b_2b_1} & \kappa_{b_2b_2} & \kappa_{b_2c} & \kappa_{b_2a} & \kappa_{b_2b_0} & \kappa_{b_2b_1} & \kappa_{b_2b_2} + j\beta_{2m} & \kappa_{b_2c}\\
\kappa_{ca} & \kappa_{cb_0} & \kappa_{cb_1} & \kappa_{cb_2} & \kappa_{cc} & \kappa_{ca} & \kappa_{cb_0} & \kappa_{cb_1} & \kappa_{cb_2} & \kappa_{cc} + j\beta_{0s}
\end{bmatrix} \tag{3.60}$$

Solution for Eq. (3.58) with an initial condition of Q(0) can be written as:

$$Q(z) = e^{Kz}Q(0) \tag{3.61}$$

3.3.2 Simulation Results and Discussions

Si and SiO$_2$ are the core and cladding materials with refractive indices of 3.473 [39] and 1.444 [182] at 1550 nm wavelength respectively. Fig. 3.8 shows the TM mode chart of slab waveguide at a wavelength of 1550 nm depicting the variation of effective refractive indices of different modes with the waveguide core width. It can be observed from the mode chart that

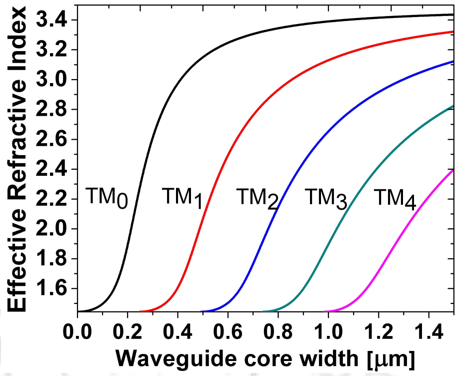

Fig. 3.8: Mode Chart with TM modes of a slab waveguide at 1550 nm.

single TM mode condition is obtained when the waveguide core width is less than 246 nm and thus w_a, w_c are taken as 246 nm. TM$_{0s}$ has an effective refractive index of 2.261. The width of WG$_b$, w_b, is taken as 900 nm such that the effective refractive indices of TM$_{1m}$, TM$_{2m}$, and TM$_{0s}$ have a substantial difference to prevent undesired co-directional coupling. The effective refractive indices of TM$_{0m}$, TM$_{1m}$, and TM$_{2m}$ are 3.371, 3.048, and 2.444 respectively.

The contra-directional coupling between TM$_{1m}$ and TM$_{0s}$ of WG$_a$, TM$_{2m}$ and TM$_{0s}$ of WG$_c$ are achieved by satisfying the phase matching conditions [69]:

$$\beta_{1m} + \beta_{0s} = \frac{2\pi}{\Lambda_1} \tag{3.62}$$

$$\beta_{2m} + \beta_{0s} = \frac{2\pi}{\Lambda_2} \tag{3.63}$$

When two dielectric waveguides are separated by a finite distance such that mode of one waveguide overlaps onto the second waveguide, the composite waveguide structure comprising the two waveguides supports a new set of eigenmode solutions called supermodes. Supermode carries energy in both the waveguides, due to which reflected supermode contains power in the input waveguide resulting in unwanted return loss. In the MDM design, return loss due to the formation of supermode and the coupling strength between the coupled modes play vital roles in determining the gap between the waveguides. Coupling strength depends on the amount of overlap between the modes, which is dependent on the separation between the waveguides. Thus, it is necessary to formulate a method to calculate the gap such that coupling strength is high and return loss is low.

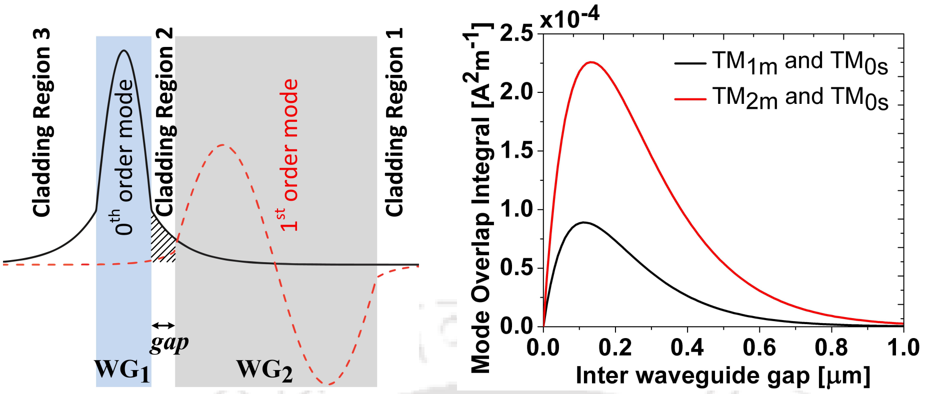

(a) (b)

Fig. 3.9: (a) Normalized TM mode profiles of two waveguides where the shaded area shows the physical overlapping of modes in the gap, (b) Variation of mode overlap integral with inter waveguide gap.

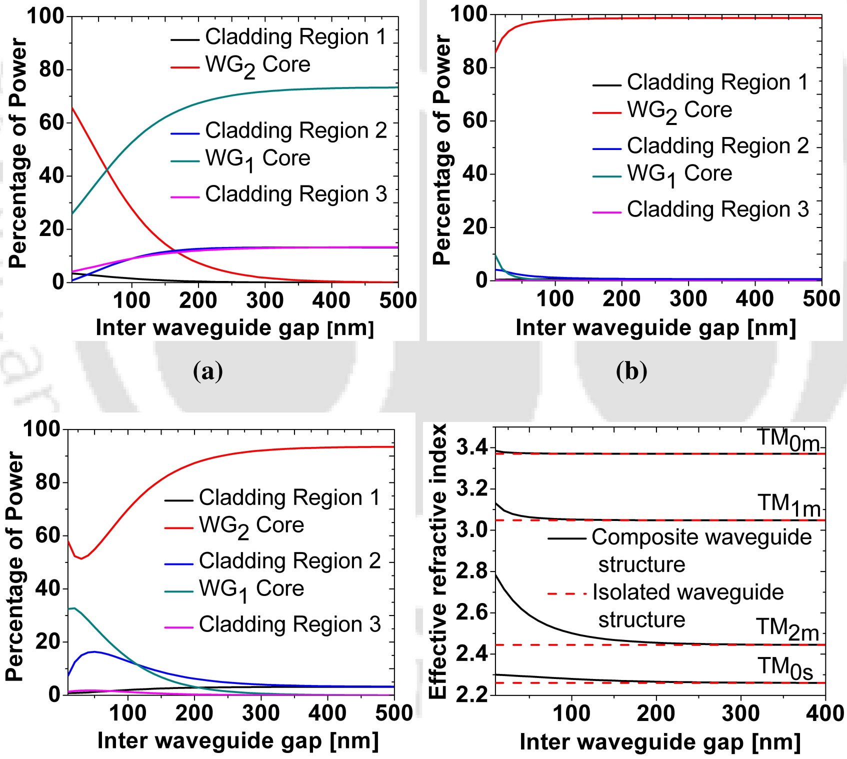

(c) (d)

Fig. 3.10: Power distribution of the supermodes corresponding to (a) TM$_{0s}$, (b) TM$_{1m}$, and (c) TM$_{2m}$ in the cladding and core regions, (d) Effective index variation of the supermodes with inter waveguide gap.

The coupling coefficient is a measure of coupling strength between two modes that can be calculated from [180]:

$$\kappa = \frac{\beta_1 \beta_2}{4\omega} \int \frac{H_{y_1}^{*}(x)\, \Delta\epsilon(x)\, H_{y_2}\, dx}{\epsilon^2(x)} \tag{3.64}$$

where κ is the coupling coefficient, β_1 and β_2 are the propagation constants, ω is the angular frequency, and H_{y_1}, H_{y_2} are the normalized magnetic field profiles of the two coupled modes. $\Delta\epsilon(x)$ represents the periodic perturbation, whereas $\epsilon(x)$ is the index profile of the entire structure. The integration is over the region where the grating is present.

From Eq. (3.64) it can be derived that the coupling coefficient is directly proportional to the mode overlap integral, which is defined as the amount of physical overlapping present between the two modes in the grating region and denoted as $\int H^*_{y_1}(x)\, H_{y_2}(x)\, dx$.

To determine the gap at which coupling strength is maximum, overlapping between TM_{1m} and TM_{0s} of WG_a, TM_{2m} and TM_{0s} of WG_c are calculated at different gaps, assuming that the grating completely covers the gap. Fig. 3.9(a) depicts the spatial overlapping of two coupled TM modes of waveguides WG_1 (with a width of 246 nm) and WG_2 (with a width of 900 nm) in the gap region. A plot between the mode overlap integral and the inter waveguide gap is shown in Fig. 3.9(b), from which it is found that for gap_1 = 110 nm and gap_2 = 130 nm, the mode overlap integrals have maximum value implying maximum coupling strength.

Figs. 3.10(a)–3.10(c) show the power distribution of the supermodes corresponding to TM_{0s}, TM_{1m}, and TM_{2m} respectively in the cladding and core region of the composite structure shown in Fig. 3.9(a) as a function of the inter waveguide gap. It can be noted that as the separation distance increases, the waveguides tend to behave as isolated waveguides, and below separation distances of 350 nm, 100 nm, and 300 nm supermodes corresponding to TM_{0s}, TM_{1m}, and TM_{2m} respectively are formed. Fig. 3.10(d) shows variation in effective index of the supermodes of the composite structure with the change in inter waveguide gap, obtained numerically. The effective indices of modes supported by the isolated waveguides are $n_{TM_{0s}}$ = 2.261, $n_{TM_{0m}}$ = 3.371, $n_{TM_{1m}}$ = 3.048, and $n_{TM_{2m}}$ = 2.444. It can be observed that as the gap between the waveguides is decreased, effective refractive indices deviate from the values of isolated waveguide modes, indicating the formation of supermodes.

Coupling strength between the modes reaches maximum when gap_1 = 110 nm and gap_2 = 130 nm. But, at these values, the composite structure supports supermodes which will cause reflection at the input port resulting in higher return loss. Thus, to minimize return loss, gaps are selected as $gap_1 = gap_2 = 350$ nm.

The proposed structure shown in Fig. 3.7 has been simulated using 2D FDTD and the results have been analyzed. N_{Λ_1} and N_{Λ_2} are taken as 200 and 178 respectively to maintain same grating length for both the gratings, whereas the widths of the grating are taken as $gW_1 = gW_2 = 175$ nm to keep undistorted output. The length of the proposed MDM device is 58 μm. Both the demultiplexing and multiplexing operations have been investigated as follows.

3.3.2.1 Demultiplexing

TM$_{0m}$, TM$_{1m}$, and TM$_{2m}$ are individually fed as inputs at Port 1 to analyze the demultiplexing operation. Figs. 3.11(a)–3.11(c) show the transmission/reflection spectra at all the ports when the inputs are TM$_{0m}$, TM$_{1m}$, and TM$_{2m}$ at Port 1. In Fig. 3.11(a), it can be observed that at Port 4 transmission is close to 100%, and no reflection peak is present at 1550 nm wavelength at any

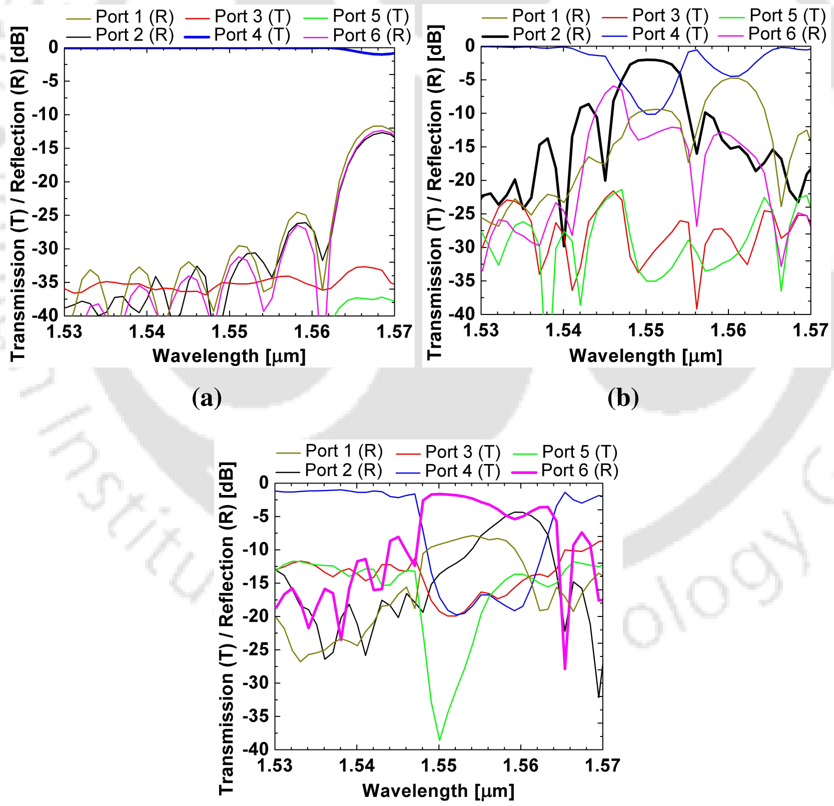

(a)

(b)

(c)

Fig. 3.11: Transmission and reflection spectrum of the proposed device during demultiplexing operation for input of (a) TM$_{0m}$, (b) TM$_{1m}$, (c) TM$_{2m}$; 'T' and 'R' represent transmission and reflection respectively.

Table 3.7: Insertion Loss and Return Loss for DEMUX

Input Mode	Insertion Loss (in dB)	Return Loss (in dB)
TM_{0m}	0.01	–31.07
TM_{1m}	2.01	–9.54
TM_{2m}	1.63	–9.17

Table 3.8: Crosstalk at different ports for DEMUX

Input Mode	Port 1 (in dB)	Port 2 (in dB)	Port 3 (in dB)	Port 4 (in dB)	Port 5 (in dB)	Port 6 (in dB)
TM_{0m}	–	–34.69	–35.12	–	–41.76	–32.51
TM_{1m}	–	–	–32.00	–10.13	–35.01	–13.58
TM_{2m}	–	–13.66	–19.58	–17.14	–38.60	–

other ports, which confirms that the TM_{0m} is not coupled to any other mode as it propagates towards Port 4. In Fig. 3.11(b), where the input is TM_{1m}, a reflection peak at 1550 nm is observed in the reflection spectrum of Port 2, which indicates that the forward propagating TM_{1m} is coupled to TM_{0s} mode of WG_a in the backward direction. Similarly, from Fig. 3.11(c), it can be observed that when TM_{2m} is fed as input, it is reflected as TM_{0s} mode of WG_c at Port 6, which is evident from the presence of reflection peak around 1550 nm at Port 6. The resulting insertion loss and return loss are tabulated in Table 3.7, whereas Table 3.8 lists the crosstalks arising at different output ports.

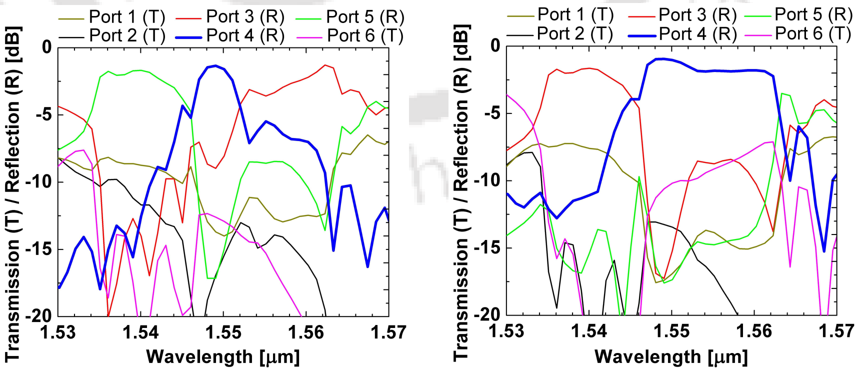

(a) (b)

Fig. 3.12: Transmission and reflection spectrum of the proposed device during multiplexing operation when input is (a) TM_{0s} of WG_a, (b) TM_{0s} of WG_c; ‘T’ and ‘R’ represent transmission and reflection respectively.

Table 3.9: Insertion Loss and Return Loss for MUX

Input Mode	Insertion Loss (in dB)	Return Loss (in dB)
TM_{0m}	0.01	–31.07
TM_{0s} of WG_a	1.59	–15.45
TM_{0s} of WG_c	1.03	–10.17

Table 3.10: Crosstalk at different ports for MUX

Input Mode	Port 1 (in dB)	Port 2 (in dB)	Port 3 (in dB)	Port 4 (in dB)	Port 5 (in dB)	Port 6 (in dB)
TM_{0m}	–	–34.69	–35.12	–	–41.76	–32.51
TM_{0s} of WG_a	–13.99	–8.05	–	–	–12.91	–14.99
TM_{0s} of WG_c	–16.90	–15.18	–13.44	–	–	–17.34

3.3.2.2 Multiplexing

Multiplexing operation is investigated by feeding TM_{0s} of WG_a (WG_c) at Port 3 (Port 5) towards -z direction and observing output at Port 4. Figs. 3.12(a)–3.12(b) show the transmission/reflection spectra at all the ports when the inputs are TM_{0s} of WG_a and TM_{0s} of WG_c. In Fig. 3.12(a), a reflection peak about 1550 nm at Port 4 is observed indicating coupling of TM_{0s} of WG_a to TM_{1m} in the opposite direction. In Fig. 3.12(b), presence of reflection peak at 1550 nm in the reflection spectrum of Port 4 implies that TM_{0s} of WG_c is coupled to TM_{2m} propagating towards Port 4. The outcome for TM_{0m} input is same as the case in the demultiplexing operation since TM_{0m} is fed at Port 1 in both the operations. The resulting insertion loss, return loss are listed in Table 3.9 and crosstalks occurring at different output ports are listed in Table 3.10.

The gap between the waveguides plays a vital role for efficient coupling, thus to study the manufacturing tolerance, the gaps between the waveguides are varied by ±10 nm and ±20 nm. The performance variation of the proposed MDM device is observed. Figs. 3.13(a)–3.13(d) show the reflection spectrum at the target ports for the inputs of TM_{1m}, TM_{2m}, TM_{0s} of WG_a, and TM_{0s} of WG_c. It has been seen that when the gap increases (decreases) the reflection spectrum shifts towards left (right) with decreasing (increasing) bandwidth. It has also been observed that the reflection strength falls below –3 dB when the gap is varied by +20 nm (–20 nm) for TM_{0s} of WG_a (TM_{1m}) input. The variation in reflection strength at the operating wavelength ranges

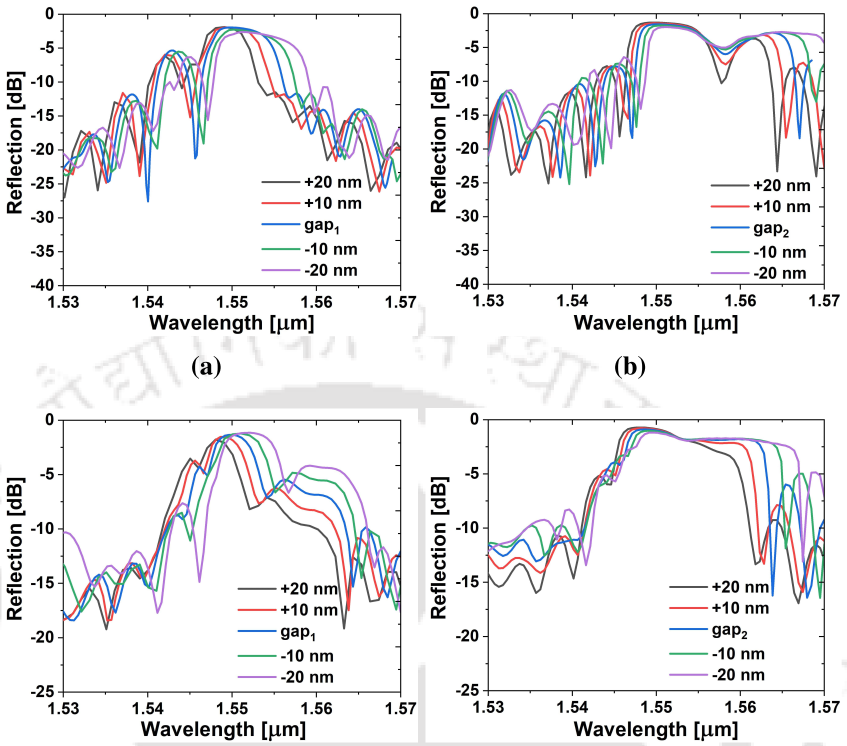

(a) (b)

(c) (d)

Fig. 3.13: Reflection spectrum at different gaps for a input of (a) TM_{1m}, (b) TM_{2m}, (c) TM_{0s} of WG_a, and (d) TM_{0s} of WG_c.

from –1.32 to –2.12 dB and –0.88 to –1.20 dB for TM_{2m} and TM_{0s} of WG_c input respectively. Thus, it can be said that the proposed device shows good fabrication tolerance.

The proposed TM MDM device is based on slab waveguide structures. However, a 3D equivalent of the proposed device, with different dimension along the width of the waveguide, can be fabricated using electron-beam lithography and inductively coupled plasma reactive ion etching followed by plasma vapor deposition process to deposit cladding oxide.

The proposed device structure is capable of (de)multiplexing three TM modes. With the use of grating$_1$ (grating$_2$), phase matching is done between TM_{1m} (TM_{2m}) and TM_{0s} of WG_a (WG_c), and as a result TM_{1m} (TM_{2m}) is coupled to contra-propagating TM_{0s} of WG_a (WG_c) while TM_{0m} is kept in the WG_b. Supermodes contribute to the return loss as the reflected supermode carries power in the input waveguide when the separation between the waveguide is below a certain distance. Thus to minimize return loss, the formation of supermode should be avoided by choosing an appropriate gap. But as the gap is increased, the value of the mode overlap integral decreases, thereby decreasing the coupling strength and resulting in larger coupling

Table 3.11: Comparison Table

Reference	Insertion Loss (dB)	Return Loss (dB)	Device Length (μm)
[174]	<5.40	<–5	~18
[173]	<6.60	<–3	~17
This Work	<2.01	<–9.17	~58

length for coupling of the same amount of power. This brings a trade-off between the device length and return loss. The crosstalks occurring at Port 4 during the demultiplexing operation due to higher-order modes have been discarded for evaluating the device performance, as they can be minimized by joining a single-mode waveguide at the end of the multimode waveguide via an adiabatic taper [183]. A comparison table of the simulation results has been given in Table 3.11, where it can be seen that the proposed device exhibits better insertion loss and return loss. In this paper, two modes are reflected/combined simultaneously by using gratings at each side of the multimode waveguide, which helps in reducing the length of the device.

3.3.3 Conclusions

A mode division (de)multiplexer has been designed for the operation at 1550 nm using slab waveguides, which can (de)multiplex three TM modes. The first and second order modes of the multimode waveguide have been coupled simultaneously to the two single-mode waveguide modes by satisfying phase-matching conditions using two grating structures in between the waveguides. The fundamental multimode bus waveguide mode continues to propagate in the forward direction without any power leakage to other modes. The proposed device is compact in size with a dimension of ~ 2.1 μm × 58 μm. The device performance has been analyzed using 2D FDTD. The insertion loss during demultiplexing is found to be in the range of 0.01 to 2.01 dB, whereas the crosstalks and return loss are in the range of –41.76 to –13.58 dB and –31.07 to –9.17 dB respectively. While multiplexing operation, the insertion loss ranges from 0.01 to 1.59 dB, the return loss is in the range of –31.07 to –10.17 dB, and the crosstalk ranges from –41.76 to –8.05 dB.

3.4 SWG-based TE Mode Division Multiplexer on Silicon for C + L band operation

As discussed in Chapter 1, SWG structures show promising coupling characteristics; this chapter proposes an SWG-based three-mode multiplexer (MUX) on a silicon-on-insulator (SOI) platform for C and L band operation. The proposed device utilizes the co-directional coupling principle to couple the modes of the single-mode waveguides to the multimode bus waveguide. The mode-MUX consists of two coupling regions, where SWG-based waveguides are employed to reduce the coupling length. The effective mode indices of the SWG waveguides in the coupling regions are matched by changing the waveguide widths keeping the duty cycle constant in order to satisfy the modal coupling criteria. The adiabatic transition between the strip waveguide modes and the SWG waveguide modes is achieved by using tapers.

3.4.1 Device Design

The bird's-eye view of the proposed SWG-based MUX is shown in Fig. 3.14. An SOI wafer with 0.22 μm top silicon and 2 μm buried oxide is used. The upper and lower cladding are both silicon dioxide. The MDM consists of three single-mode (SM) and one multimode (MM) waveguide, which are the inputs and output of the MUX. The inputs are labeled as IN$_j$ for the TE$_0$–TE$_j$ coupling and the output as OUT as shown in Fig. 3.14. SM$_0$, SM$_1$, and SM$_2$ are the single-mode waveguides for the IN$_0$, IN$_1$, and IN$_2$ inputs, respectively. The MM waveguide has a width of 1.5 μm. All the SWGs have a duty cycle of a/Λ, where a and Λ are the silicon layer thickness and period of the SWG as shown in the inset of Fig. 3.14. In this study, all the SWGs have the same duty cycle of 66.67% with a = 160 nm and Λ = 240 nm. The three SWGs are SM$_1^{SWG}$, SM$_2^{SWG}$, and MM^{SWG}. The gap between SM$_1^{SWG}$ (SM$_2^{SWG}$) and MM^{SWG}

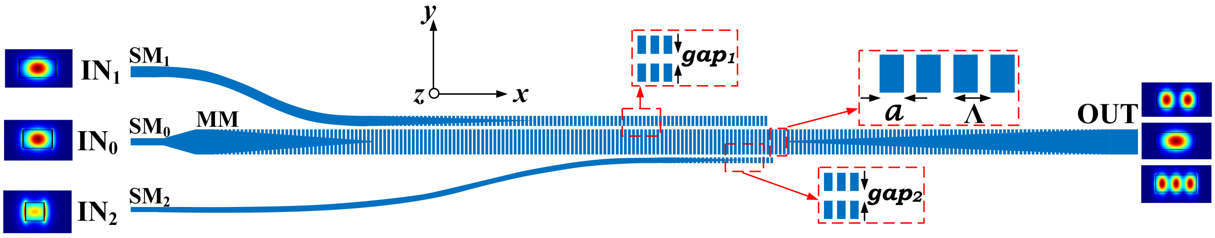

Fig. 3.14: Bird's-eye view of the designed MUX (not to scale).

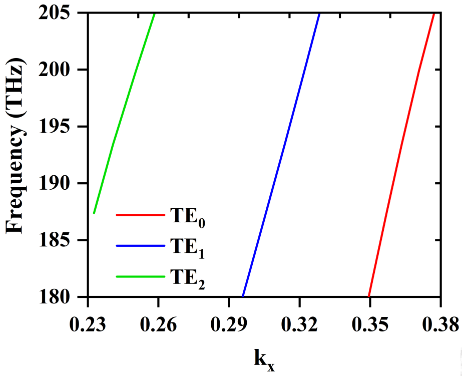

Fig. 3.15: Frequency versus wavevector plot (band structure) for different transverse electric modes.

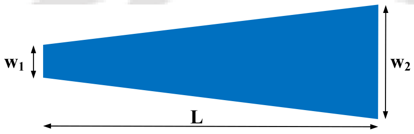

Fig. 3.16: Bird's-eye view of an adiabatic taper.

is represented by gap_1 (gap_2). The band structure analysis is done to determine the effective indices of the Bloch modes [76] in the SWG waveguides using Lumerical® FDTD solutions. The band structure plot for the supported TE modes of the MM^{SWG} waveguide is shown in Fig. 3.15. For 1550 nm wavelength operation, the optical frequency is 193.41 THz at which the x-component of the wavevector (k_x) is 0.363, 0.314, and 0.241 for the TE_0, TE_1, and TE_2 mode, respectively. The corresponding mode effective indices (n_{eff}) can be calculated as

$$n_{eff} = k_x \frac{\Lambda}{\lambda} \tag{3.65}$$

where λ is the free space wavelength of light. The effective indices of the TE_0, TE_1, and TE_2 modes determined from the band structure plot are 2.347, 2.026, and 1.555, respectively, at 1550 nm. The waveguide widths of SM_0, SM_1, and SM_2 are 0.5 μm, 0.67 μm, and 0.34 μm, respectively. The widths of SM_1 and SM_2 are chosen so that the SWG mode effective indices of the SM_1^{SWG} and SM_2^{SWG} waveguides match with the first and second-order mode indices of the MM^{SWG} waveguide in order for mode coupling to occur.

The TE_0 mode of the SM_0 strip waveguide is converted to the TE_0 mode of the MM strip waveguide using an adiabatic taper of slope +0.25 μm/μm. The taper slope is defined with the help of Fig. 3.16 as

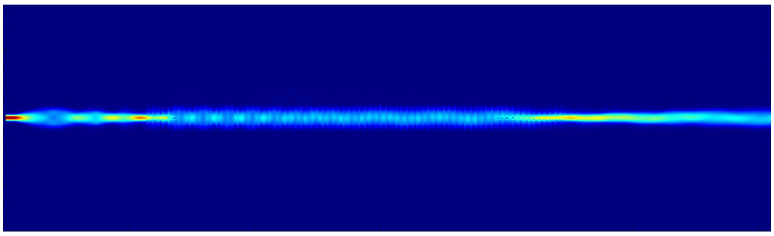

(a) Input at IN_0

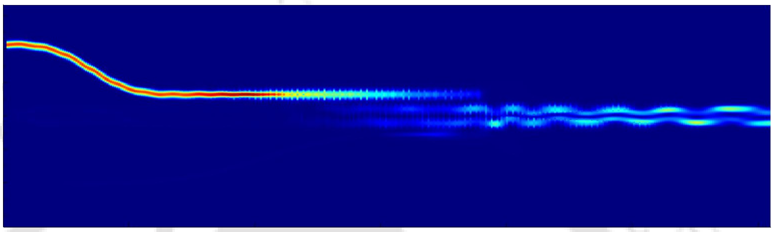

(b) Input at IN_1

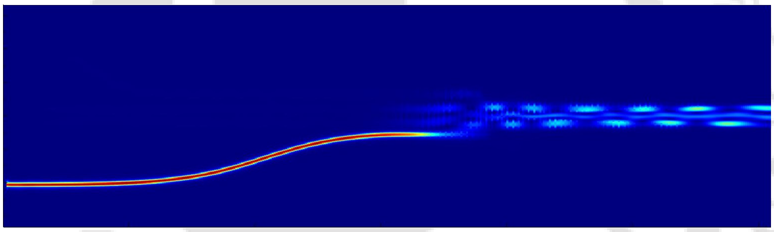

(c) Input at IN_2

Fig. 3.17: Transmission profile for power launched at different input ports.

$$\text{Taper slope} = \frac{w_2 - w_1}{2L} \tag{3.66}$$

The MM^{SWG} waveguide has two tapers at the input and output side to couple the strip waveguide mode to the SWG Bloch mode and vice-versa. The input and output side tapers have a slope of -0.072 μm/μm and +0.036 μm/μm with a length of 10 μm and 20 μm, respectively. The minimum feature size is kept 0.06 μm in accordance with e-beam lithography resolution. The output taper length is twice the input taper length since the input taper is only used for the fundamental mode transition, whereas the output taper is used to couple three SWG modes to the strip waveguide. The SM_1 and SM_2 strip waveguides are bent waveguides with a length of 14 μm and 32 μm, respectively. The two ends of the bent waveguides are laterally separated by a distance of 3 μm. The tapers used in SM_1^{SWG} and SM_2^{SWG} have a slope of -0.0305 μm/μm and -0.028 μm/μm with a length of 10 μm and 5 μm, respectively. The waveguide separation, gap_1 and gap_2 are 0.2 μm and 0.195 μm, respectively. The coupling lengths without the tapered regions are 14.00 μm and 1.48 μm for the TE_0–TE_1 and TE_0–TE_2 mode coupling, respectively. The total device length is 61 μm with 25 μm SWG length of the MM waveguide without tapers.

3.4.2 Simulation Results and Discussions

The proposed device has been simulated in Lumerical® using the 3D FDTD method. The Palik model has been used to represent silicon and silicon dioxide permittivities, which also takes into account the dispersive effects. Simulation has been carried out from 1525 nm to 1625 nm wavelength range covering the whole C and L optical telecom band. The transmission power profile at 1525 nm is shown in Fig. 3.18(a)-(c) for the single-mode inputs at IN_0, IN_1, and IN_2.

The input normalized transmission plot along with the insertion loss for TE_0 input at IN_0, IN_1, and IN_2 is shown in Fig. 3.18(a). At 1550 nm, the transmission for the TE_0–TE_0, TE_0–TE_1, and TE_0–TE_2 mode coupling is ~98%, ~88%, and ~90%, respectively. The corresponding insertion loss is <0.6 dB at 1550 nm. The lowest transmission and highest insertion loss over the whole simulated range are ~78% and 1.1 dB, which occur at 1625 nm for the TE_0–TE_2 coupling.

The return loss for different input port excitation is shown in Fig. 3.18(b). The return loss is <–15 dB over the whole simulated range, limited by the TE_0–TE_2 mode coupling. The return loss for inputs at IN_0, IN_1, and IN_2 at 1550 nm operation is ~–34 dB, ~–30 dB, and ~–15 dB, respectively.

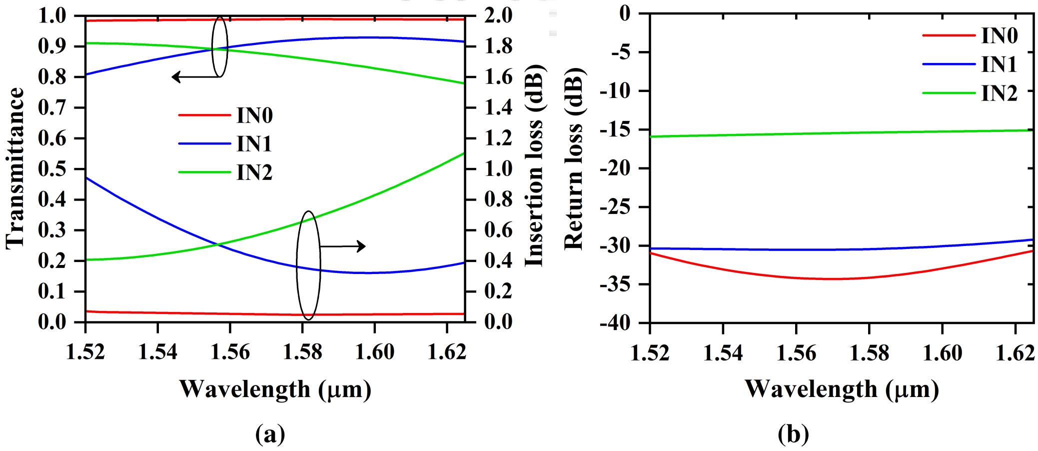

(a) (b)

Fig. 3.18: (a) Transmission and insertion loss, and (b) return loss for different inputs.

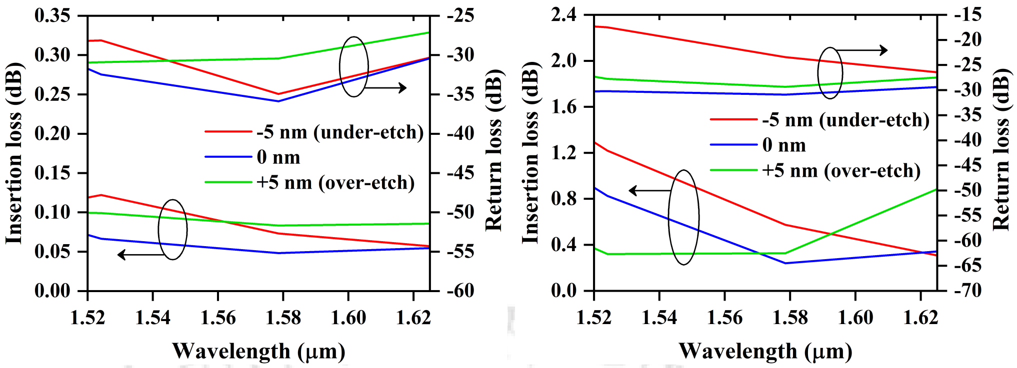

(a) Input at IN_0 **(b)** Input at IN_1

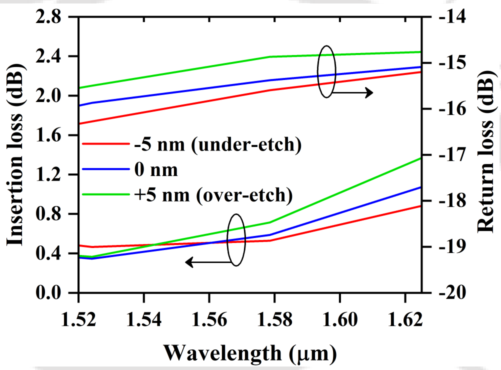

(c) Input at IN_2

Fig. 3.19: Insertion loss and return loss with variations in device dimensions for different inputs.

3.4.3 Tolerance study

An important issue in fabrication is controlling the dimensions of sub-micron devices, which may lead to poor device performance. To overcome this, the design should have high fabrication tolerance so that changes in the device dimension by few nanometers do not adversely affect the device performance. A tolerance study has been done assuming a uniform under-etch and over-etch of 5 nm. With 5 nm under-etch (over-etch), each waveguide width increases (decreases) by 10 nm, a = 170 nm (150 nm), gap_1 = 0.19 μm (0.21 μm), and gap_2 = 0.185 μm (0.205 μm). The insertion loss and return loss for variation in device dimensions with excitation at inputs IN_0, IN_1, and IN_2 are shown in Figs. 3.19(a)-(c). It can be observed from Fig. 3.19 that for the TE_0–TE_0 mode coupling (IN_0 input), the insertion loss is <0.12 dB and return loss is <–26 dB for ±10 nm change in dimension. For the TE_0–TE_1 mode coupling (IN_1 input), a 10 nm increase in the device dimensions leads to an increase in both insertion loss and return loss at lower wavelengths. At longer wavelengths, the insertion loss is more for decreasing

Table 3.12: Insertion loss and return loss data at 1550 nm for variations in device dimension.

Dimension change (nm)	**Insertion loss (dB)**			**Return loss (dB)**		
	IN$_0$	**IN$_1$**	**IN$_2$**	**IN$_0$**	**IN$_1$**	**IN$_2$**
-5 (under-etch)	0.10	0.90	0.50	–30.19	–29.40	–15.94
0	0.06	0.54	0.46	–33.77	–30.52	–15.63
+5 (over-etch)	0.10	0.32	0.53	–30.67	–28.44	–15.19

Table 3.13: Comparison of the three-mode MUX with literature.

Ref.	**No. of modes**	**Wavelength range (nm)**	**Insertion Loss (dB)**
[184][a]	2	1530–1590	<1
[185][b]	2 3	1500–1600	<0.49 <1.7
[186][c]	2	1455–1645	<0.72
This work[d]	3	1525–1625	<1.1

[a] Subwavelength-assisted Y-junction; [b] ADC; [c] Nanocube-assisted ADC; [d] SWG-based ADC.

device dimensions. The insertion loss increases with a decrease in device dimension at longer wavelengths for the TE$_0$–TE$_2$ mode coupling (IN$_2$ input). The return loss increases (decreases) with a decrease (increase) in device dimensions over the whole simulated wavelength range. The insertion loss and return loss data at 1550 nm for different inputs and device dimension variations are given in Table. 3.12. The variation in insertion loss at 1550 nm for TE$_0$–TE$_0$, TE$_0$–TE$_1$, and TE$_0$–TE$_2$ mode coupling is 0.04 dB, 0.58 dB, and 0.07 dB, respectively. The comparison of the three-mode MUX with recent literature is given in Table. 3.13, from which it can be seen that the designed device shows better performance compared to the state-of-the-art.

3.4.4 Conclusions

A three-mode MUX has been designed in a silicon photonics platform for C and L band operation. SWG waveguides have been used in the proposed MUX design in order to reduce the coupling length. The device is simulated using a 3D FDTD solver over 1525 nm to 1625 nm wavelength range. The resulting mode transmission, insertion loss, and return loss are >78%, <1.1 dB, and <–15 dB respectively over 100 nm bandwidth. The transmission is >88% and insertion loss is <0.6 dB at 1550 nm. Changing the device dimensions by ± 10 nm results in insertion loss <1.4 dB and return loss <–14.6 dB over the simulated wavelength range. The designed MUX shows good transmission characteristics and fabrication tolerance and can be used for broadband operation over the C and L optical telecom bands using three transverse electric modes.

3.5 SWG-based compact broadband two-mode multiplexer

In this chapter, an SWG-based mode MUX with two-mode channels is demonstrated on the SOI platform to operate from 1550 to 1560 nm wavelength range. The proposed device has a coupling region that comprises a SWG waveguide and a conventional multimode strip waveguide. The fundamental Bloch-Floquet TM mode of the SWG waveguide is co-directionally coupled to the first-order TM mode of the multimode strip waveguide. The period and duty cycle of the SWG waveguide are varied to match the effective indices of the coupled modes. The 3D FDTD numerical technique is implemented for the device simulation and analysis.

3.5.1 Device Structure

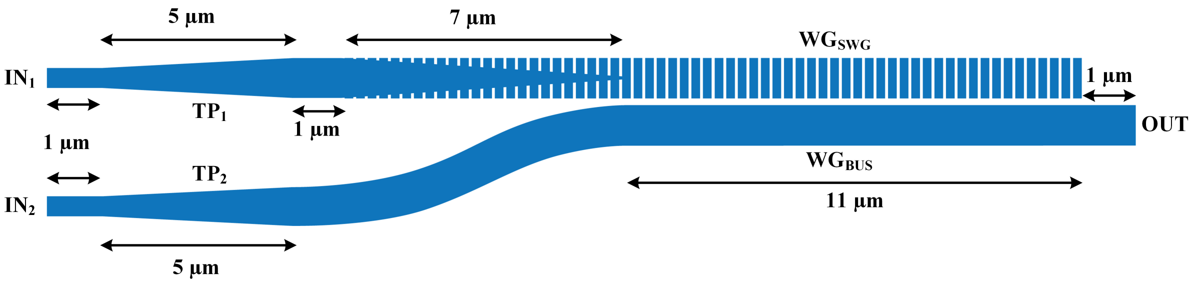

Fig. 3.20: Top view of the proposed MUX.

The top view of the proposed two-mode MUX is depicted in Fig. 3.20. The device is designed on the SOI substrate with a 220 nm Si layer sandwiched between an upper and a lower SiO_2 layer with 2 μm thickness each. The input ports are denoted as IN_1, IN_2, and the output port is denoted as OUT. The two input strip waveguides are single-mode waveguides with a width of 500 nm, separated by a distance of 2.65 μm. The fundamental TM modes of the input strip waveguides are converted to the fundamental TM modes of the multimode strip waveguides via

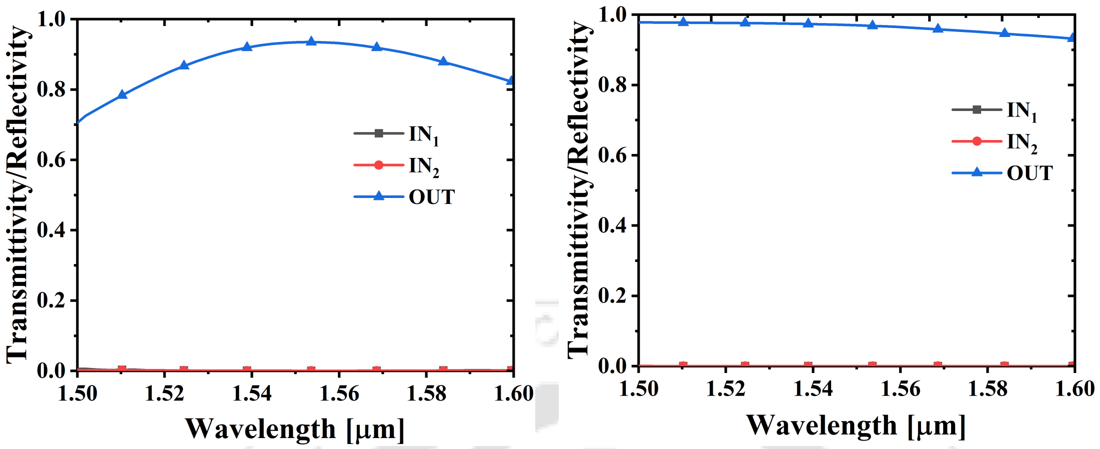

(a) (b)

Fig. 3.21: Transmission characteristics when input is given at (a) IN$_1$ and (b) IN$_2$.

adiabatic tapers (TP$_1$ and TP$_2$) of length 5 μm. The width of the multimode waveguide is 1 μm, which supports two TM modes (fundamental and first-order). For an adiabatic transition between the fundamental TM mode of the multimode strip waveguide and the SWG waveguide (WG$_{SWG}$), a 7 μm taper is used. An S-bend is used to connect TP$_2$ and the multimode waveguide (WG$_{BUS}$). WG$_{SWG}$ and WG$_{BUS}$ have the same cross-sectional dimension. The distance between WG$_{BUS}$ and WG$_{SWG}$ is kept as 150 nm with a coupling length of 11 μm. The overall length of the device is 26 μm. To phase-match the fundamental TM WG$_{SWG}$ mode and first-order TM WG$_{BUS}$ mode, the grating period and duty cycle of WG$_{SWG}$ are taken as 280 nm and 77.5%, respectively.

3.5.2 Simulation Results

The proposed device is simulated using Lumerical® 3D FDTD. The simulation domain has a dimension of 26 μm, 10 μm, and 3 μm along the length (x-axis), width (y-axis), and thickness (z-axis), respectively. The simulation is executed with eight PML layers, mesh accuracy of level 3, and simulation time of 1000 fs. The fundamental TM modes at IN$_1$ and IN$_2$ are excited and the resulting transmission characteristics are shown in Fig. 3.21. When the input is given at IN$_1$ (IN$_2$), greater than 70% (90%) transmission is observed within 1500 to 1600 nm wavelength range with a transmission of 93.5% (97%) at 1550 nm. The power profiles of the mode propagation for both the inputs are shown in Fig. 3.22. The mode coupling between the respective

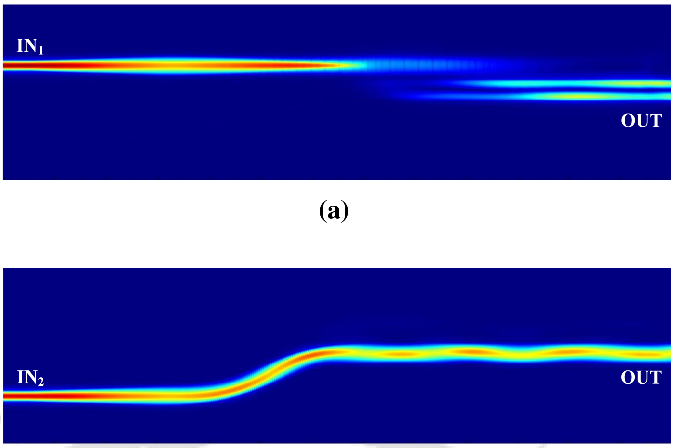

(a)

(b)

Fig. 3.22: Simulated light propagation (power) for the input at (a) IN_1 and (b) IN_2.

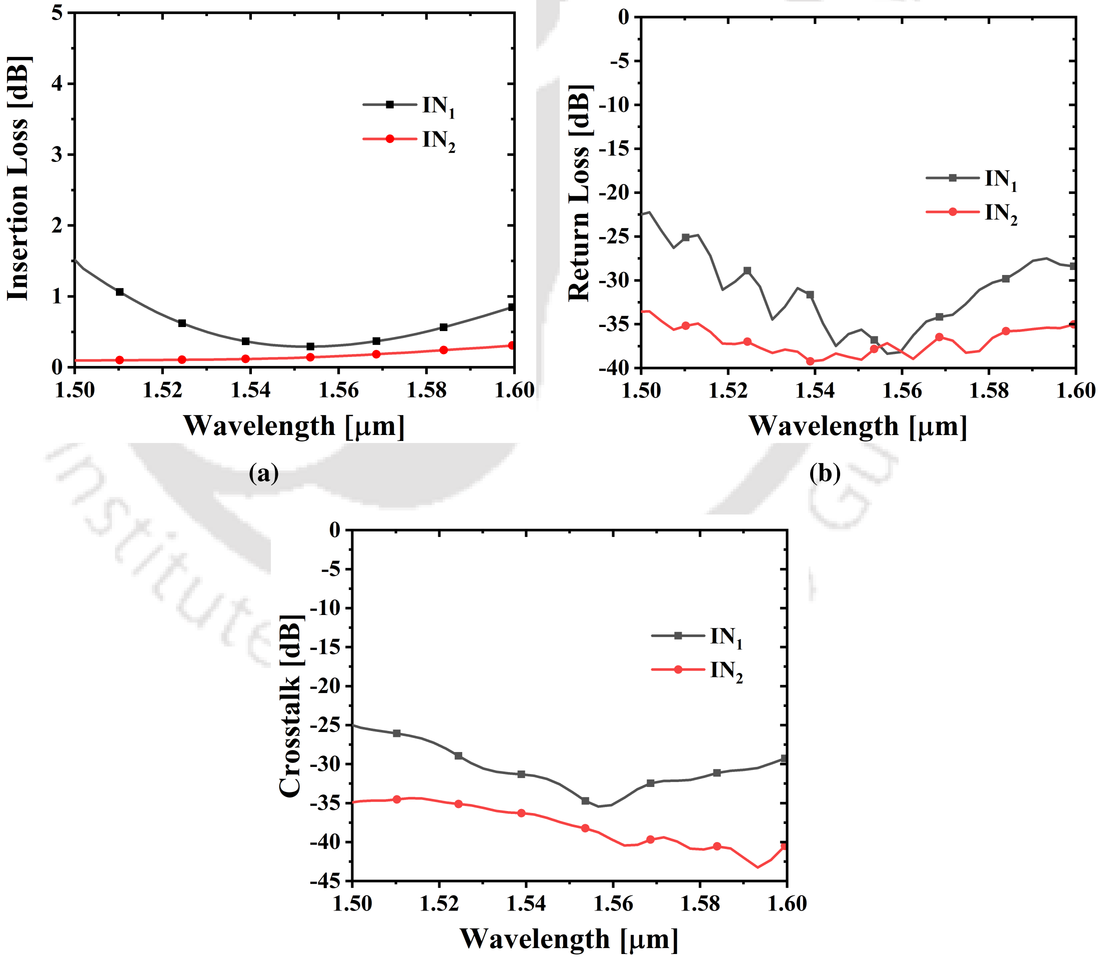

(a)

(b)

(c)

Fig. 3.23: Variation of (a) IL, (b) RL, and (c) CT with wavelength when the inputs are excited at IN_1 and IN_2.

modes can be clearly seen from the power profile.

The IL, RL, and CT plots for inputs at IN_1 and IN_2 are shown in Fig. 3.23. The IL, RL, and CT at 1550 nm for IN_1 (IN_2) input are 0.29 dB, –35.62 dB, and –33.60 dB (0.13 dB, –39.04 dB, and –37.89 dB), respectively. The overall IL, RL, and CT are <1.51 dB, <–22.49 dB, and <–25 dB, respectively over the broad wavelength range of 1500 to 1600 nm.

3.5.3 Conclusions

A compact SWG-based two-mode multiplexer is designed and simulated using 3D FDTD on the SOI platform. The device utilizes the fundamental and first-order TM modes of the multimode strip waveguide as the data carrying channels. The WG_{SWG} period and duty cycle are selected such that the effective index of the fundamental TM WG_{SWG} mode matches that of the first-order TM WG_{BUS} which results in power coupling between the two modes, whereas the fundamental strip waveguide mode propagates in the same waveguide. The proposed multiplexer shows IL <0.29 dB, RL <–35.62 dB, and CT <–33.60 dB at 1550 nm with a compact device length of 26 μm.

3.6 Summary

In summary, a TE MDM and a TM MDM have been designed using Si slab waveguides. The device structures utilized collateral contra-directional couplers for coupling the higher order multimode waveguide modes and single mode waveguide modes. In addition, an SWG based two mode TM MDM and three mode TE MDM have been demonstrated on the SOI platform.

4

Mode and Polarization Division (De)multiplexer

Contents

4.1 Introduction

The link capacity using a single wavelength source can be further improved by merging MDM and PDM technologies to form a hybrid mode and polarization division (MDM-PDM) (de)multiplexer. A few hybrid MDM-PDM devices have been accomplished using DPWA [135], Y-junction [187], and ADCs [137], etc. However, these reported (de)multiplexers operate in broadband and are less applicable for wavelength selective devices. On the other hand, grating assisted devices provide greater control over operating wavelength by varying the grating period. Thus, a grating assisted MDM-PDM (de)multiplexer is essential for link capacity enhancement of optical networks with wavelength selective operation.

In this chapter, a hybrid MDM-PDM (de)multiplexer has been designed to operate at 1550 nm. The proposed device is based on a CMOS compatible SOI platform with buried strip waveguides. 2.5D FDTD technique, which is a combination of effective index method (EIM) and 2D FDTD, has been used for designing and analyzing the device performance. In the previous chapter, slab waveguide and SWG based TE/TM-MDMs have been reported. Here, a TE-MDM is cascaded with a TM-MDM to create a hybrid MDM-PDM (de)multiplexer to increase the number of channels. The proposed device is composed of four identical single-mode access waveguides and a multimode bus waveguide. Grating structures are used in between the waveguides to ensure coupling between modes of the bus and access waveguides by satisfying the phase-matching conditions. Simultaneous (de)multiplexing of three quasi-transverse electric (quasi-TE) modes and two quasi-transverse magnetic (quasi-TM) modes of the bus waveguide has been achieved with insertion loss $>$ –0.76 dB, return loss $<$ –11.23 dB, and crosstalk $<$ –12.42 dB for the proposed device.

4.2 Device structure and operation

A schematic representation of the proposed device structure is shown in Fig. 4.1, which is designed using buried strip waveguides based on the SOI platform. The core material is Si and cladding, cover materials are SiO_2. The refractive indices of Si (n_{Si}) and SiO_2 (n_{SiO_2}) are taken as 3.473 [39] and 1.444 [182] respectively at the operating wavelength of 1550 nm.

The thickness of the waveguide is along the x-axis, width is along the y-axis, and the mode propagation is along the z-direction. For the CMOS compatibility, the thickness of the strip waveguide is taken as 220 nm. The device consists of a multimode waveguide (WG_m) and four identical single-mode waveguides (WG_{s1}, WG_{s2}, WG_{s3}, and WG_{s4}). The width of the single-mode waveguide is w_s and the width of the multimode waveguide is w_m. The grating structures namely, $grating_1$, $grating_2$, $grating_3$, $grating_4$ are placed in the gaps between WG_{s1} and WG_m (gap_1), WG_m and WG_{s2} (gap_2), WG_{s3} and WG_m (gap_3), WG_m and WG_{s4} (gap_4) respectively. The proposed device structure utilizes three quasi-TE modes (namely, TE_0^m, TE_1^m, and TE_2^m) and two quasi-TM modes (namely, TM_0^m and TM_1^m) of WG_m as data-carrying channels for communication. The fundamental quasi-TM modes of WG_{s1}, WG_{s2} are denoted as TM_0^{s1}, TM_0^{s2} and the fundamental quasi-TE modes of WG_{s3}, WG_{s4} are denoted as TE_0^{s3}, TE_0^{s4} respectively. During demultiplexing operation, different TE and TM modes of WG_m are excited at the input port to propagate along +z-direction, whereas during the multiplexing operation, fundamental modes of the single-mode waveguides are excited at their respective ports. Contra-directional coupling between TM_0^m and TM_0^{s1}, TM_1^m and TM_0^{s2}, TE_1^m and TE_0^{s3}, TE_2^m and TE_0^{s4} are realized by setting the grating periods of $grating_1$, $grating_2$, $grating_3$, $grating_4$ to satisfy the following

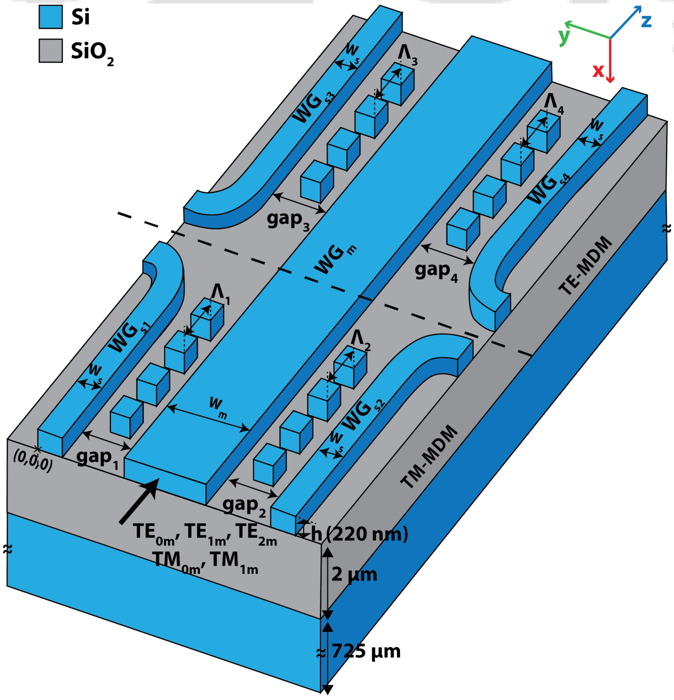

Fig. 4.1: Proposed Device Structure; cover has not been shown.

phase-matching conditions [188]:

$$\beta_{0m}^{TM} + \beta_{s1}^{TM} = \frac{2\pi}{\Lambda_1} \tag{4.1a}$$

$$\beta_{1m}^{TM} + \beta_{s2}^{TM} = \frac{2\pi}{\Lambda_2} \tag{4.1b}$$

$$\beta_{1m}^{TE} + \beta_{s3}^{TE} = \frac{2\pi}{\Lambda_3} \tag{4.1c}$$

$$\beta_{2m}^{TE} + \beta_{s4}^{TE} = \frac{2\pi}{\Lambda_4} \tag{4.1d}$$

where, $\beta_{1m}^{TE}, \beta_{2m}^{TE}, \beta_{0m}^{TM}, \beta_{1m}^{TM}, \beta_{s3}^{TE}, \beta_{s4}^{TE}, \beta_{s1}^{TM}, \beta_{s2}^{TM}$ are the propagation constants of TE_1^m, TE_2^m, TM_0^m, TM_1^m, TE_0^{s3}, TE_0^{s4}, TM_0^{s1}, TM_0^{s2}, and Λ_1, Λ_2, Λ_3, Λ_4 are the grating periods of grating_1, grating_2, grating_3, grating_4 respectively.

4.3 Mathematical Model

The proposed device is a combination of TM-MDM and TE-MDM. In this section, a mathematical model for the coupling region of both TM- and TE-MDM is discussed. Using the perturbation approach [188], the refractive index profile for the proposed structure can be defined as:

$$TM-MDM : \epsilon(x,y) = \epsilon_0[n_{SiO_2}^2 + \Delta n_{s1}^2(x,y) + \Delta n_{s2}^2(x,y) + \Delta n_m^2(x,y) + \Delta n_{grating_1}^2(x,y) + n_{grating_2}^2(x,y)] \tag{4.2a}$$

$$TE-MDM : \epsilon(x,y) = \epsilon_0[n_{SiO_2}^2 + \Delta n_{s3}^2(x,y) + \Delta n_{s4}^2(x,y) + \Delta n_m^2(x,y) + \Delta n_{grating_3}^2(x,y) + n_{grating_4}^2(x,y)] \tag{4.2b}$$

where, ϵ_0 is the permittivity of free space, Δn_{s1}^2, Δn_{s2}^2, Δn_{s3}^2, Δn_{s4}^2, Δn_m^2, $\Delta n_{grating_1}^2$, $\Delta n_{grating_2}^2$, $\Delta n_{grating_3}^2$, and $\Delta n_{grating_4}^2$ signify the presence of WG_{s1}, WG_{s2}, WG_{s3}, WG_{s4}, WG_m, grating_1, grating$_2$, grating$_3$, and grating$_4$ respectively, which are given as:

$$\Delta n_{sj}^2(x,y) = \begin{cases} n_{Si}^2 - n_{SiO_2}^2, & \text{waveguide } \ \text{WG}_{sj} \\ 0, & \text{elsewhere} \end{cases} \tag{4.3a}$$

$$\Delta n_{m}^2(x,y) = \begin{cases} n_{Si}^2 - n_{SiO_2}^2, & \text{waveguide } \ \text{WG}_{m} \\ 0, & \text{elsewhere} \end{cases} \tag{4.3b}$$

$$\Delta n_{grating_j}^2(x,y) = \begin{cases} (n_{Si}^2 - n_{SiO_2}^2) \times F_j(z), & \text{grating}_j \\ 0, & \text{elsewhere} \end{cases} \tag{4.3c}$$

where $j = 1, 2, 3, 4$ and F$_j$(z) is the fourier series expansion term, defined as:

$$F_j(z) = \sum_{a=-\infty}^{\infty} e^{ia\pi/2}\Big[\frac{sin(a\pi/2)}{a\pi}\Big]e^{-ia(2\pi/\Lambda_j)z} \tag{4.4}$$

4.3.1 Mode Profile Analysis

The mode profiles of the eigenmodes supported by each waveguide are calculated using the EIM, where the 3D structure is divided into two 2D slab waveguide structures, one along the height and another along the width. To find the mode profile of a quasi-TE mode, first y-component of the electric field E$_y$(x) is determined by performing TE analysis along the x-directed slab and then determining the y-directed electric field E$_y$(y) by performing TM analysis on the slab waveguide along the y-axis, while replacing the refractive index of the core with the effective refractive index of the eigenmode obtained from the TE analysis. The cross-sectional electric field profile of the quasi-TE mode ($\Psi^{TE}(x,y)$) can be calculated as:

$$\Psi^{TE}(x,y) = E_y(x).E_y(y) \tag{4.5}$$

Similarly, the cross-sectional mode profiles of the quasi-TM mode can be calculated by first performing TM analysis on the slab along the x-axis (H$_y$(x)) and then performing TE analysis on the slab along the y-axis (H$_y$(y)). The cross-sectional y-directed magnetic field of the quasi-TM mode ($\Psi^{TM}(x,y)$) can be expressed as:

$$\Psi^{TM}(x,y) = H_y(x).H_y(y) \tag{4.6}$$

The proposed device structure has a slab height (h) of 220 nm, the y-directed electric field and magnetic field profiles along the slab height remain the same for all the eigenmodes of the waveguides, which can be expressed as follows.

TM analysis on slab height (h) yields:

$$H_y(x) = \begin{cases} P_H e^{-\gamma_{cH}x}, \; x > 0 \\ P_H\Big[cos(\gamma_{gH}x) - \frac{n_{Si}^2\gamma_{cH}}{n_{SiO_2}^2\gamma_{gH}} sin(\gamma_{gH}x)\Big], \; -h < x < 0 \\ P_H\Big[cos(\gamma_{gH}h) + \frac{n_{Si}^2\gamma_{cH}}{n_{SiO_2}^2\gamma_{gH}} sin(\gamma_{gH}h)\Big]e^{\gamma_{cH}(x+h)}, \; x < -h \end{cases} \tag{4.7}$$

TE analysis on slab height (h) gives:

$$E_y(x) = \begin{cases} P_E e^{-\gamma_{cE}x}, \; x > 0 \\ P_E\Big[cos(\gamma_{gE}x) - \frac{\gamma_{cE}}{\gamma_{gE}} sin(\gamma_{gE}x)\Big], \; -h < x < 0 \\ P_E\Big[cos(\gamma_{gE}h) + \frac{\gamma_{cE}}{\gamma_{gE}} sin(\gamma_{gE}h)\Big]e^{\gamma_{cE}(x+h)}, \; x < -h \end{cases} \tag{4.8}$$

where

$$\gamma_{cE/cH} = \sqrt{\left(\beta_h^{TE/TM}\right)^2 - \left(\frac{2\pi n_{SiO_2}}{\lambda_0}\right)^2} \tag{4.9a}$$

$$\gamma_{gE/gH} = \sqrt{\left(\frac{2\pi n_{Si}}{\lambda_0}\right)^2 - \left(\beta_h^{TE/TM}\right)^2} \tag{4.9b}$$

Here β_h^{TE} (β_h^{TM}) is the propagation constant of the fundamental TE (TM) mode of the slab waveguide in the yz plane and λ_0 is the wavelength of operation. By performing TE analysis, the electric field mode profile along the width of the waveguides WG$_{s1}$ (E_x^{s1}), WG$_m$ (E_x^q), and

WG$_{s2}$ (E_x^{s2}) can be written as:

$$E_x^{s1}(y) = \begin{cases} P_{s1}e^{-\gamma_a^{TE}y},\ y > 0 \\ P_{s1}\Big[cos(\gamma_b^{TE}y) - \Big(\frac{\gamma_a^{TE}}{\gamma_b^{TE}}\Big) \\ \times\ sin(\gamma_b^{TE}y)\Big],\ -w_s < y < 0 \\ P_{s1}\Big[cos(\gamma_b^{TE}w_s) + \Big(\frac{\gamma_a^{TE}}{\gamma_b^{TE}}\Big) \\ \times\ sin(\gamma_b^{TE}w_s)\Big]e^{\gamma_a^{TE}(y+w_s)},\ y < -w_s \end{cases} \tag{4.10}$$

$$E_x^q(y)\Big|_{q=0,1} = \begin{cases} P_{eq}e^{-\gamma_{cq}^{TE}(y+k)},\ y > -k \\ P_{eq}\Big[cos(\gamma_{dq}^{TE}(y+k)) - \Big(\frac{\gamma_{cq}^{TE}}{\gamma_{dq}^{TE}}\Big) \\ \times\ sin(\gamma_{dq}^{TE}(y+k))\Big],\ -k < y < -(k+w_m) \\ P_{eq}\Big[cos(\gamma_{dq}^{TE}y) + \Big(\frac{\gamma_{cq}^{TE}}{\gamma_{dq}^{TE}}\Big) \\ \times\ sin(\gamma_{dq}^{TE}y)\Big]e^{\gamma_{cq}^{TE}(y+k+w_m)},\ y < -(k+w_m) \end{cases} \tag{4.11}$$

$$E_x^{s2}(y) = \begin{cases} P_{s2}e^{-\gamma_a^{TE}(y+l)},\ y > -l \\ P_{s2}\Big[cos(\gamma_b^{TE}(y+l)) - \Big(\frac{\gamma_a^{TE}}{\gamma_b^{TE}}\Big) \\ \times\ sin(\gamma_b^{TE}(y+l))\Big],\ -l < y < -(l+w_s) \\ P_{s2}\Big[cos(\gamma_b^{TE}w_s) + \Big(\frac{\gamma_a^{TE}}{\gamma_b^{TE}}\Big) \\ \times\ sin(\gamma_b^{TE}w_s)\Big]e^{\gamma_a^{TE}(y+l+w_s)},\ y < -(l+w_s) \end{cases} \tag{4.12}$$

where

$$k = w_s + gap_1,\ l = w_s + w_m + gap_1 + gap_2$$

$$
\begin{aligned}
\gamma_a^{TE} &= \sqrt{\left(\beta_{eff}\right)^2 - \left(\frac{2\pi n_{SiO_2}}{\lambda_0}\right)^2} \\
\gamma_b^{TE} &= \sqrt{\left(\beta_h^{TM}\right)^2 - \left(\beta_{eff}\right)^2} \\
\gamma_{cq}^{TE}\Big|_{q=0,1} &= \sqrt{\left(\beta_{eff}^{q}\right)^2 - \left(\frac{2\pi n_{SiO_2}}{\lambda_0}\right)^2} \\
\gamma_{dq}^{TE}\Big|_{q=0,1} &= \sqrt{\left(\beta_h^{TM}\right)^2 - \left(\beta_{eff}^{q}\right)^2}
\end{aligned}
$$

where β_{eff} and β_{eff}^{q} are the propagation constants of the quasi-TM eigenmodes of WG$_{s1}$ and WG$_{s2}$ respectively. The magnetic field mode profile along the width of the waveguides WG$_{s3}$ (H_x^{s3}), WG$_m$ (H_x^{n}), and WG$_{s4}$ (H_x^{s4}) using TM analysis can be expressed as:

$$
H_x^{s3}(y) = \begin{cases}
P_{s3}e^{-\gamma_a^{TM}y}, \ y > 0 \\
P_{s3}\Big[cos(\gamma_b^{TM}y) - \Big(\frac{\gamma_a^{TM}}{\gamma_b^{TM}}\frac{n_{Si}^2}{n_{SiO_2}^2}\Big) \\
\times\, sin(\gamma_b^{TM}y)\Big], \ -w_s < y < 0 \\
P_{s3}\Big[cos(\gamma_b^{TM}w_s) + \Big(\frac{\gamma_a^{TM}}{\gamma_b^{TM}}\frac{n_{Si}^2}{n_{SiO_2}^2}\Big) \\
\times\, sin(\gamma_b^{TM}w_s)\Big]e^{\gamma_a^{TM}(y+w_s)}, \ y < -w_s
\end{cases} \tag{4.13}
$$

$$
H_x^{n}(y)\Big|_{n=0,1,2} = \begin{cases}
P_{hn}e^{-\gamma_{cn}^{TM}(y+u)}, \ y > -u \\
P_{hn}\Big[cos(\gamma_{dn}^{TM}(y+u)) - \Big(\frac{\gamma_{cn}^{TM}}{\gamma_{dn}^{TM}}\frac{n_{Si}^2}{n_{SiO_2}^2}\Big) \\
\times\, sin(\gamma_{dn}^{TM}(y+u))\Big], \ -u < y < -(u+w_m) \\
P_{hn}\Big[cos(\gamma_{dn}^{TM}w_m) + \Big(\frac{\gamma_{cn}^{TM}}{\gamma_{dn}^{TM}}\frac{n_{Si}^2}{n_{SiO_2}^2}\Big) \\
\times\, sin(\gamma_{dn}^{TM}w_m)\Big]e^{\gamma_{cn}^{TM}(y+u+w_m)}, \ y < -(u+w_m)
\end{cases} \tag{4.14}
$$

$$H_x^{s4}(y) = \begin{cases} P_{s4}e^{-\gamma_a^{TM}(y+v)}, \; y > -v \\ P_{s4}\Big[cos(\gamma_b^{TM}(y+v)) - \Big(\frac{\gamma_a^{TM}}{\gamma_b^{TM}}\frac{n_{Si}^2}{n_{SiO_2}^2}\Big) \\ \times \; sin(\gamma_b^{TM}(y+v))\Big], \; -v < y < -(v+w_s) \\ P_{s4}\Big[cos(\gamma_b^{TM}w_s) + \Big(\frac{\gamma_a^{TM}}{\gamma_b^{TM}}\frac{n_{Si}^2}{n_{SiO_2}^2}\Big) \\ \times \; sin(\gamma_b^{TM}w_s)\Big]e^{\gamma_a^{TM}(y+v+w_s)}, \; y < -(v+w_s) \end{cases} \tag{4.15}$$

where

$$u = w_s + gap_3, \; v = w_s + w_m + gap_3 + gap_4$$

$$\begin{aligned} \gamma_a^{TM} &= \sqrt{\Big(\beta_{eff}\Big)^2 - \Big(\frac{2\pi n_{SiO_2}}{\lambda_0}\Big)^2} \\ \gamma_b^{TM} &= \sqrt{\Big(\beta_h^{TE}\Big)^2 - \Big(\beta_{eff}\Big)^2} \\ \gamma_{cn}^{TM}\Big|_{n=0,1,2} &= \sqrt{\Big(\beta_{eff}^n\Big)^2 - \Big(\frac{2\pi n_{SiO_2}}{\lambda_0}\Big)^2} \\ \gamma_{dn}^{TM}\Big|_{n=0,1,2} &= \sqrt{\Big(\beta_h^{TE}\Big)^2 - \Big(\beta_{eff}^n\Big)^2} \end{aligned}$$

where β_{eff} and β_{eff}^n are the propagation constants of the quasi-TE eigenmodes of WG$_{s3}$ and WG$_{s4}$ respectively. The corresponding y-component of electric field and magnetic field can be calculated from:

$$E_y(y) = \frac{\beta}{\omega\epsilon_0 n^2(x)}H_x(y) \tag{4.16}$$

$$H_y(y) = \frac{-\beta}{\omega\mu_0}E_x(y) \tag{4.17}$$

where $n^2(x)$ is the refractive index profile of the respective waveguide along the x-axis, and β is the propagation constant. ω is the angular frequency of operation, and μ_0 is the magnetic permeability of free space. The cross-sectional y-directed magnetic fields of the TM modes and y-directed electric field of the TE modes supported by the waveguides can be expressed as follows:

$$\Psi_{sj}^{TM}(x,y)\Big|_{j=1,2} = H_y(x).H_y^{sj}(y) \tag{4.18a}$$

$$\Psi_{qm}^{TM}(x,y)\Big|_{q=0,1} = H_y(x).H_y^q(y) \tag{4.18b}$$

$$\Psi_{sj}^{TE}(x,y)\Big|_{j=3,4} = E_y(x).E_y^{sj}(y) \tag{4.19a}$$

$$\Psi_{qm}^{TE}(x,y)\Big|_{q=0,1,2} = E_y(x).E_y^q(y) \tag{4.19b}$$

The values of the constant coefficients P_{s1}, P_{eq}, P_{s2}, P_{s3}, P_{hn}, and P_{s4} in Eqs. (4.10)–(4.15) are calculated from the normalizing condition of the cross-sectional electric and magnetic fields. The fields are normalized to a power flow of 1 W in the z-direction, i.e.:

$$\int_{-\infty}^{\infty}\int_{-\infty}^{\infty} |\Psi^{TE}(x,y)|^2 \epsilon(y)\, dx\, dy = \frac{2\mu_0\beta}{\beta_h^{TM}\epsilon_0} \tag{4.20a}$$

$$\int_{-\infty}^{\infty}\int_{-\infty}^{\infty} \frac{|\Psi^{TM}(x,y)|^2}{\epsilon(x)}\, dx\, dy = \frac{2\epsilon_0\beta}{\beta_h^{TE}\mu_0} \tag{4.20b}$$

where $\epsilon(x)$ and $\epsilon(y)$ represent permittivity of the waveguide under consideration along the x and y direction, respectively. The magnetic field (electric field) in the coupled waveguide structure of TM-MDM (TE-MDM) can be expressed as:

$$\begin{aligned} H(x,y,z) = {} & A^+(z)\Psi_{s1}^{TM}(x,y)e^{i(\omega t-\beta_{s1}^{TM}z)} + \\ & \sum_{p=0}^{1} B_p^+(z)\Psi_{pm}^{TM}(x,y)e^{i(\omega t-\beta_{pm}^{TM}z)} + C^+(z)\Psi_{s2}^{TM}(x,y)e^{i(\omega t-\beta_{s2}^{TM}z)} + \\ & A^-(z)\Psi_{s1}^{TM}(x,y)e^{i(\omega t+\beta_{s1}^{TM}z)} + \sum_{p=0}^{2} B_p^-(z)\Psi_{pm}^{TM}(x,y)e^{i(\omega t+\beta_{pm}^{TM}z)} + \\ & C^-(z)\Psi_{s2}^{TM}(x,y)e^{i(\omega t+\beta_{s2}^{TM}z)} \end{aligned} \tag{4.21}$$

$$\begin{aligned} E(x,y,z) = {} & P^+(z)\Psi_{s3}^{E}(x,y)e^{i(\omega t-\beta_{s3}^{TE}z)} + \\ & \sum_{p=0}^{2} Q_p^+(z)\Psi_{pm}^{TE}(x,y)e^{i(\omega t-\beta_{pm}^{TE}z)} + R^+(z)\Psi_{s4}^{TE}(x,y)e^{i(\omega t-\beta_{s4}^{TE}z)} + \\ & P^-(z)\Psi_{s3}^{TE}(x,y)e^{i(\omega t+\beta_{s3}^{TE}z)} + \sum_{p=0}^{2} Q_p^-(z)\Psi_{pm}^{TE}(x,y)e^{i(\omega t+\beta_{pm}^{TE}z)} + \\ & R^-(z)\Psi_{s4}^{TE}(x,y)e^{i(\omega t+\beta_{s4}^{TE}z)} \end{aligned} \tag{4.22}$$

where $A(z)$, $B_p(z)$, and $C(z)$ ($P(z)$, $Q_p(z)$, and $R(z)$) are the z-dependent amplitude of TM (TE) eigenmodes supported by WG$_{s1}$, WG$_m$, and WG$_{s2}$ (WG$_{s3}$, WG$_m$, and WG$_{s4}$) respectively. p denotes the p^{th} order eigenmode. $^+$ and $^-$ signs indicate the propagation in +z and –z direction respectively.

4.3.2 Coupled-Mode Equations

In this subsection, the solutions for the governing coupled-mode equations in the coupling region of both TM- and TE-MDM have been presented. The phase mismatched terms in the coupled-mode equations have been neglected.

4.3.2.1 TM-MDM

The coupled-mode equations for TM-MDM can be given as:

$$\frac{\partial B_0^+}{\partial z} = -iA^-(z)\kappa_1 \tag{4.23a}$$

$$\frac{\partial A^-}{\partial z} = iB_0^+(z)\kappa_1^* \tag{4.23b}$$

$$\frac{\partial B_1^+}{\partial z} = -iC^-(z)\kappa_2 \tag{4.23c}$$

$$\frac{\partial C^-}{\partial z} = iB_1^+(z)\kappa_2^* \tag{4.23d}$$

where * denotes complex conjugate and κ_1, κ_2 are the coupling coefficients, defined as:

$$\kappa_1 = K.\beta_{s1}^{TM}\beta_{0m}^{TM}P_{s1}P_{e0}\Big[cos(\gamma_b^{TE}w_s) + \frac{\gamma_a^{TE}}{\gamma_b^{TE}}sin(\gamma_b^{TE}w_s)\Big] \times \frac{2e^{-(\gamma_a^{TE}+\gamma_{c0}^{TE})gap_1/2}}{\gamma_a^{TE}-\gamma_{c0}^{TE}}sinh\{(\gamma_a^{TE}-\gamma_{c0}^{TE})gH_1/2\} \tag{4.24}$$

$$\kappa_2 = K.\beta_{s2}^{TM}\beta_{1m}^{TM}P_{s2}P_{e1}\Big[cos(\gamma_{d1}^{TE}w_m) + \frac{\gamma_{c1}^{TE}}{\gamma_{d1}^{TE}}sin(\gamma_{d1}^{TE}w_m)\Big] \times \frac{2e^{-(\gamma_a^{TE}+\gamma_{c1}^{TE})gap_2/2}}{\gamma_{c1}^{TE}-\gamma_a^{TE}}sinh\{(\gamma_{c1}^{TE}-\gamma_a^{TE})gH_2/2\} \tag{4.25}$$

where gH_1, gH_2 are the grating width of grating$_1$, grating$_2$ respectively and K is defined as:

$$K = \frac{i(n_{Si}^2 - n_{SiO_2}^2)}{4\pi\omega\mu_0} P_H^2 \Big[\frac{h}{2}\Big\{1 + \Big(\frac{\gamma_{cH} n_{Si}^2}{\gamma_{gE} n_{SiO_2}^2}\Big)^2\Big\} + \frac{sin(2\gamma_{gH} h)}{4\gamma_{gH}} \times$$
$$\times \Big\{1 - \Big(\frac{\gamma_{cH} n_{Si}^2}{\gamma_{gH} n_{SiO_2}^2}\Big)^2\Big\} + \frac{\gamma_{cH} n_{Si}^2}{2\gamma_{gH}^2 n_{SiO_2}^2}\Big\{1 - cos(2\gamma_{gH} h)\Big\}\Big] \tag{4.26}$$

For a given coupling length L and the boundary conditions $A^-(L) = C^-(L) = 0$, the solutions to Eqn. (4.23) can be written as:

$$B_0^+(z) = \frac{B_0^+(0)\; cosh\{|\kappa_1|(L-z)\}}{cosh(|\kappa_1|L)} \tag{4.27a}$$
$$A^-(z) = \frac{-i\kappa_1^* B_0^+(0) sinh\{|\kappa_1|(L-z)\}}{|\kappa_1| cosh(|\kappa_1|L)} \tag{4.27b}$$
$$B_1^+(z) = \frac{B_1^+(0)\; cosh\{|\kappa_2|(L-z)\}}{cosh(|\kappa_2|L)} \tag{4.27c}$$
$$C^-(z) = \frac{-i\kappa_2^* B_1^+(0) sinh\{|\kappa_2|(L-z)\}}{|\kappa_2| cosh(|\kappa_2|L)} \tag{4.27d}$$

where $B_0^+(0)$ and $B_1^+(0)$ are the initial mode amplitudes at $z = 0$.

4.3.2.2 TE-MDM

The coupled-mode equations for TE-MDM can be expressed as:

$$\frac{\partial Q_1^+}{\partial z} = -iP^-(z)\zeta_1 \tag{4.28a}$$
$$\frac{\partial P^-}{\partial z} = iQ_1^+(z)\zeta_1^* \tag{4.28b}$$
$$\frac{\partial Q_2^+}{\partial z} = -iR^-(z)\zeta_2 \tag{4.28c}$$
$$\frac{\partial R^-}{\partial z} = iQ_2^+(z)\zeta_2^* \tag{4.28d}$$

where ζ_1 and ζ_2 are the coupling coefficients, defined as:

$$\zeta_1 = Z.\frac{\beta_{1m}^{TE}\beta_{s3}^{TE}}{n_{SiO_2}^4}P_{s3}P_{h1}\Big[cos(\gamma_b^{TM}w_s) + \frac{\gamma_a^{TM}n_{Si}^2}{\gamma_b^{TM}n_{SiO_2}^2}sin(\gamma_b^{TM}w_s)\Big] \times \frac{2e^{-(\gamma_a^{TM}+\gamma_{c1}^{TM})gap_3/2}}{\gamma_a^{TM}-\gamma_{c1}^{TM}}sinh\{(\gamma_a^{TM}-\gamma_{c1}^{TM})gH_3/2\} \quad (4.29)$$

$$\zeta_2 = Z.\frac{\beta_{2m}^{TE}\beta_{s4}^{TE}}{n_{SiO_2}^4}P_{s4}P_{h2}\Big[cos(\gamma_{d2}^{TM}w_m) + \frac{\gamma_{c2}^{TM}n_{Si}^2}{\gamma_{d2}^{TM}n_{SiO_2}^2}sin(\gamma_{d2}^{TM}w_m)\Big] \times \frac{2e^{-(\gamma_a^{TM}+\gamma_{c2}^{TM})gap_4/2}}{\gamma_{c2}^{TM}-\gamma_a^{TM}}sinh\{(\gamma_{c2}^{TM}-\gamma_a^{TM})gH_4/2\} \quad (4.30)$$

where gH_3, gH_4 are the grating widths of grating$_3$, grating$_4$ respectively and Z is defined as:

$$Z = \frac{i(n_{Si}^2 - n_{SiO_2}^2)}{4\pi\omega\epsilon_0}P_E^2\Big[\frac{h}{2}\Big\{1+\Big(\frac{\gamma_{cE}}{\gamma_{gE}}\Big)^2\Big\} + \frac{sin(2\gamma_{gE}h)}{4\gamma_{gE}}\times \times\Big\{1-\Big(\frac{\gamma_{cE}}{\gamma_{gE}}\Big)^2\Big\} + \frac{\gamma_{cE}}{2\gamma_{gE}^2}\Big\{1-cos(2\gamma_{gE}h)\Big\}\Big] \quad (4.31)$$

Similarly, the solutions to Eqn. (4.27) can be expressed as:

$$Q_1^+(z) = \frac{Q_1^+(0)\ cosh\{|\zeta_1|(L-z)\}}{cosh(|\zeta_1|L)} \quad (4.32a)$$

$$P^-(z) = \frac{-i\zeta_1^* Q_1^+(0) sinh\{|\zeta_1|(L-z)\}}{|\zeta_1| cosh(|\zeta_1|L)} \quad (4.32b)$$

$$Q_2^+(z) = \frac{Q_2^+(0)\ cosh\{|\zeta_2|(L-z)\}}{cosh(|\zeta_2|L)} \quad (4.32c)$$

$$R^-(z) = \frac{-i\zeta_2^* Q_2^+(0) sinh\{|\zeta_2|(L-z)\}}{|\zeta_2| cosh(|\zeta_2|L)} \quad (4.32d)$$

where $Q_1^+(0)$ and $Q_2^+(0)$ are the initial mode amplitudes at $z = 0$ and $P^-(L) = R^-(L) = 0$ at $z = L$.

4.4 Results and Discussions

The effective refractive index change of the supported modes with the variation of waveguide width using the EIM has been plotted in Fig. 4.2 at 1550 nm wavelength, which is known as the modechart. The width of the single-mode waveguides (WG$_{s1}$, WG$_{s2}$, WG$_{s3}$, and WG$_{s4}$), w_s, is taken as 320 nm to satisfy the single-mode condition. The width of the multimode waveguide WG$_m$ (w_m) is taken as 1400 nm to accommodate 3 quasi-TE and 3 quasi-TM modes, such that any undesirable co-directional coupling with the single-mode waveguides is prevented. The effective refractive indices of the modes are taken from the mode chart, as shown in Fig. 4.2. The normalized cross-sectional electric field and magnetic field profiles of the corresponding quasi-TE and quasi-TM eigenmodes as calculated using the EIM are given in Fig. 4.3.

Considering the design criteria given in [189] for avoiding the supermode formation to reduce undesired co-directional coupling between the modes, the gap between the waveguides are taken as gap$_1$ = gap$_2$ = 900 nm, gap$_3$ = 350 nm, and gap$_4$ = 500 nm. The grating periods Λ_1 (grating$_1$), Λ_2 (grating$_2$), Λ_3 (grating$_3$), and Λ_4 (grating$_4$) are determined from Eq. (4.1). The grating position and grating width are optimized such that there is less distortion at the output spectrum and the desired (de)multiplexing operation is achieved at the operating wavelength of 1550 nm. The optimized grating position is at the middle of the distance between the single-mode access waveguide and multimode bus waveguide.

The main disadvantage with the 3D FDTD technique is that it involves rigorous full vectorial calculations, making it computationally intensive with long simulation time. 2.5D FDTD is an alternative method to analyze planar photonic integrated circuits, which is computationally less intensive with faster simulation runtime, and the results are comparable to that of 3D FDTD [39]. In 2.5D FDTD, the 3D structure is collapsed into a 2D structure using EIM. Then

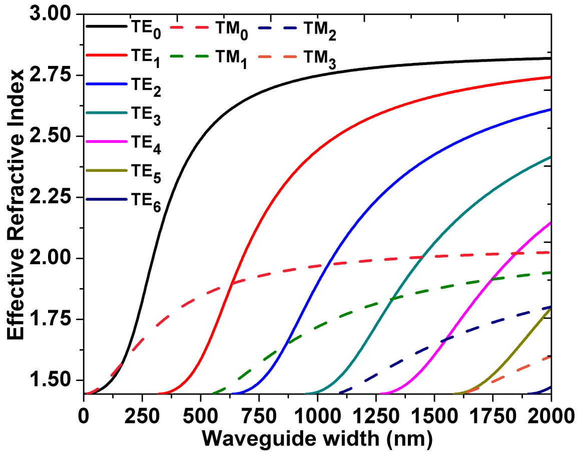

Fig. 4.2: Modechart at 1550 nm wavelength with Si as core and SiO$_2$ as cladding substrate/cover

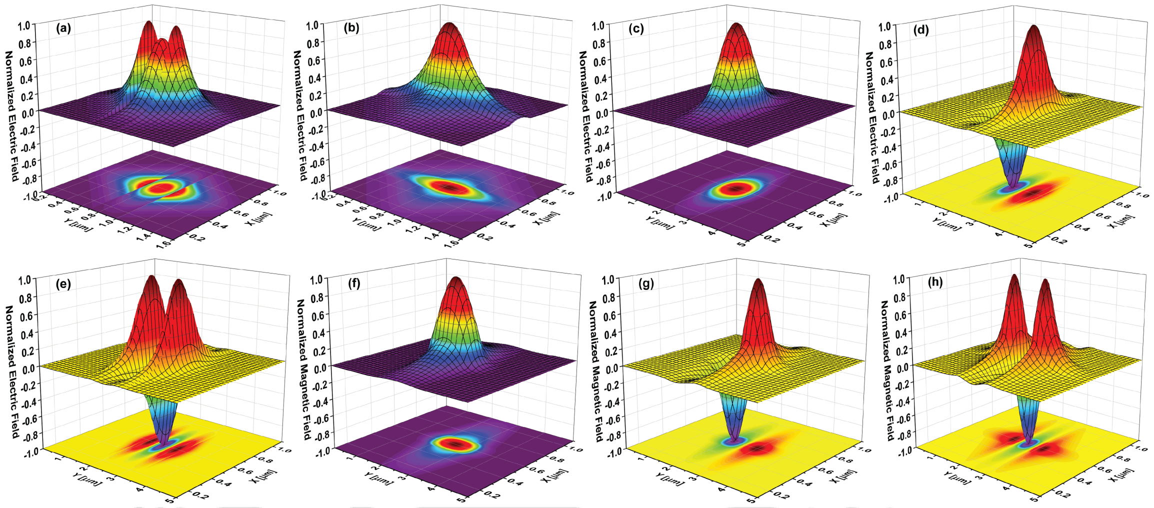

Fig. 4.3: Normalized cross-sectional mode profile of (a) $\text{TE}_0^{s1/s2/s3/s4}$, (b) $\text{TM}_0^{s1/s2/s3/s4}$, (c) TE_0^m, (d) TE_1^m, (e) TE_2^m, (f) TM_0^m, (g) TM_1^m, (h) TM_2^m; (a), (c)-(e) show E_y field and (b), (f)-(h) show H_y field.

this resulting 2D structure can be simulated using 2D FDTD. To analyze the quasi-TE wave propagation, first TE analysis is performed on the vertical slab height (h) to obtain the effective refractive index of the fundamental TE mode, say n_h^{TE}. The 3D structure is converted to a 2D structure by taking n_h^{TE} as the core refractive index. This 2D structure is the top-view of the 3D device. TM analysis is then performed on the 2D structure to obtain the magnetic field profile of the TM mode supported by the planar slab waveguide. The wave propagation of this resulting TM mode is studied using 2D FDTD to replicate the wave propagation of the quasi-TE mode of the 3D structure. Similarly, the propagation of quasi-TM waves can be analyzed by studying the wave propagation of the TE mode supported by the 2D structure, where the core refractive index is n_h^{TM} (refractive index of the fundamental TM mode obtained by performing TM analysis on the vertical slab height h).

Using this method, an equivalent 2D structure is created and is shown in Fig. 4.4. This

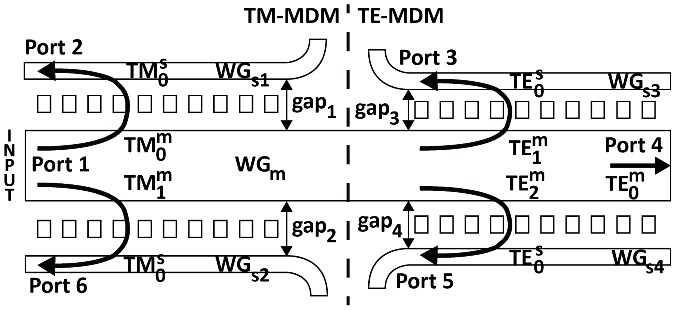

Fig. 4.4: Equivalent 2D structure of the proposed device.

structure is simulated using 2D FDTD, and the performance of the device is analyzed by measuring the transmitted/reflected power at the output ports while different modes are excited at the input port. The power of all the input modes are set to 1 W; thus, the power output (in dB) can be expressed as:

$$P_{dB} = 10\log_{10}(P_{out}) \tag{4.33}$$

where P_{out} is the transmission/reflection power measured at a particular output port in Watt.

To reduce the simulation time, the TM-MDM and TE-MDM regions are simulated separately, and the response for each quasi-TM and quasi-TE inputs (TM_0^m, TM_1^m, TE_0^m, TE_1^m, and TE_2^m) are noted. The responses are then concatenated in order to obtain the final output of the proposed device structure. Fig. 4.5 shows the simulated light propagation at 1550 nm wave-

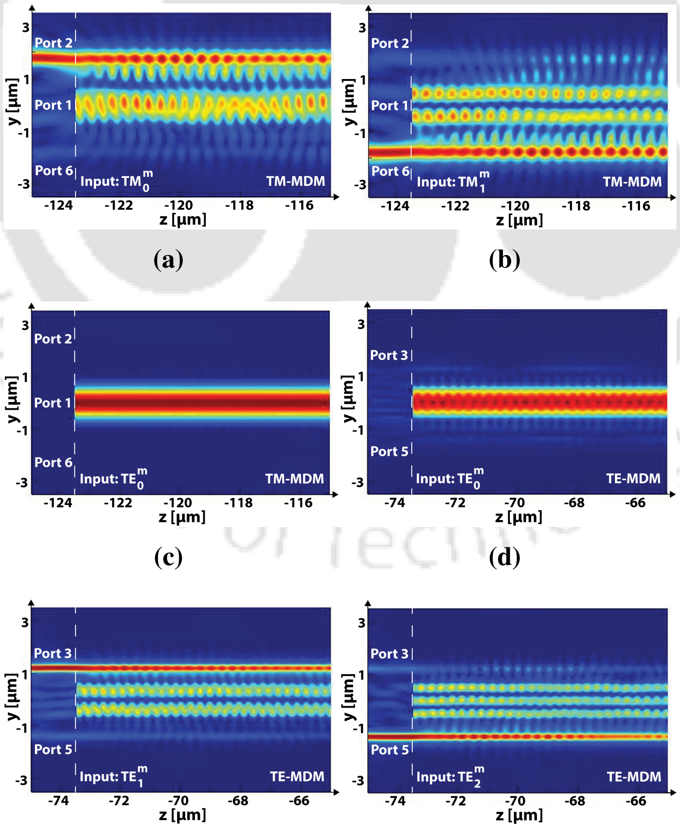

(a) (b)

(c) (d)

(e) (f)

Fig. 4.5: Simulated light propagation at 1550 nm when the inputs are (a) TM_0^m, (b) TM_1^m, (c) TE_0^m in the TM-MDM region; (d) TE_0^m, (e) TE_1^m, (f) TE_2^m in the TE-MDM region; dotted line denotes the input line, and the waveguide bents are not shown.

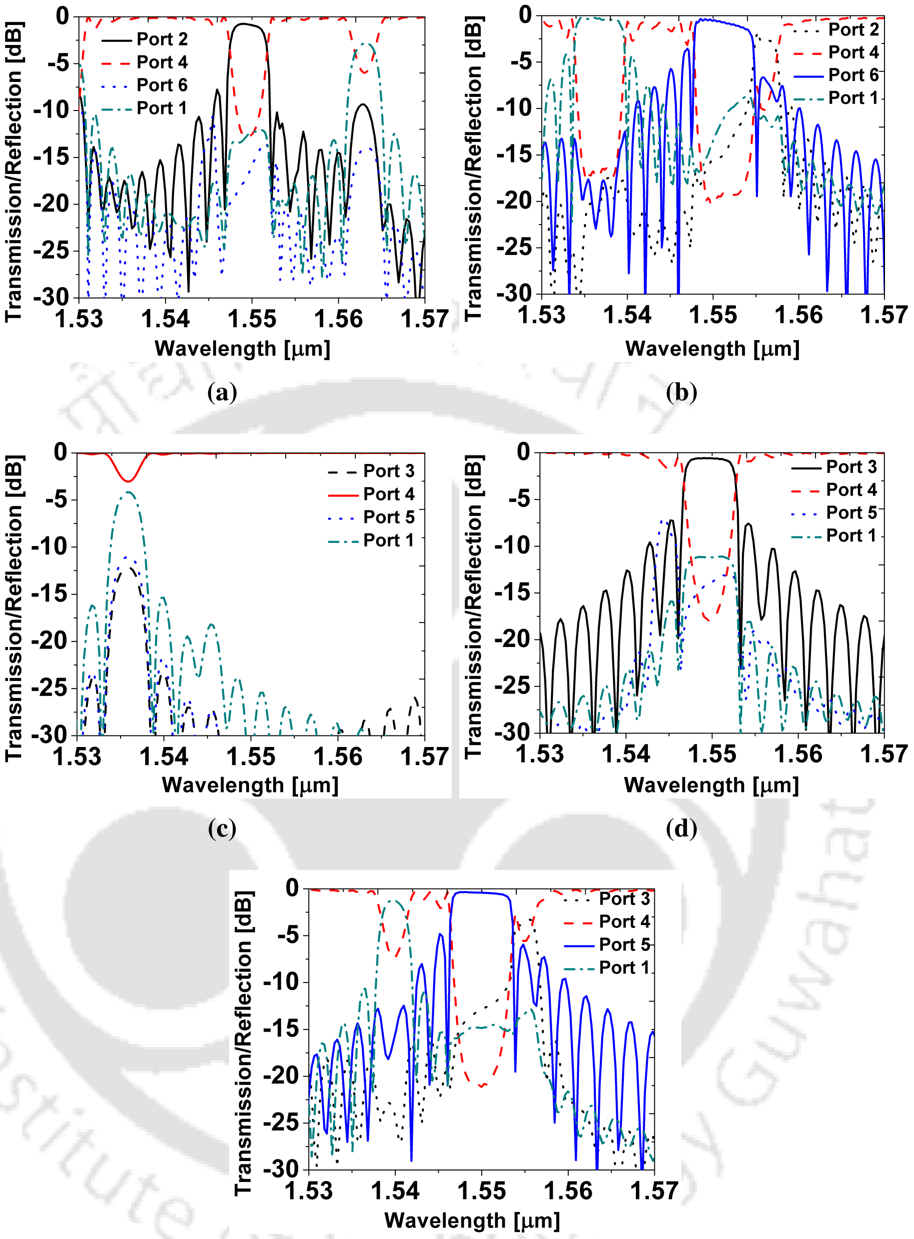

(a) (b) (c) (d) (e)

Fig. 4.6: Transmission/reflection spectra for the proposed design at their respective output ports when the input is (a) TM_0^m, (b) TM_1^m, (c) TE_0^m, (d) TE_1^m, and (e) TE_2^m.

length when TM_0^m, TM_1^m, TE_0^m are excited in the TM-MDM structure and TE_0^m TE_1^m, TE_2^m in the TE-MDM structure. It can be observed from the figures that the modes TM_0^m, TM_1^m, TE_1^m, and TE_2^m are coupled to their respective ports, whereas TE_0^m mode propagates almost unaltered without any coupling in both the TM- and TE-MDM regions.

The transmission/reflection spectra at the output ports and the input port for the proposed structure are shown in Fig. 4.6. Fig. 4.6(a) shows the transmission/reflection spectrum for TM_0^m

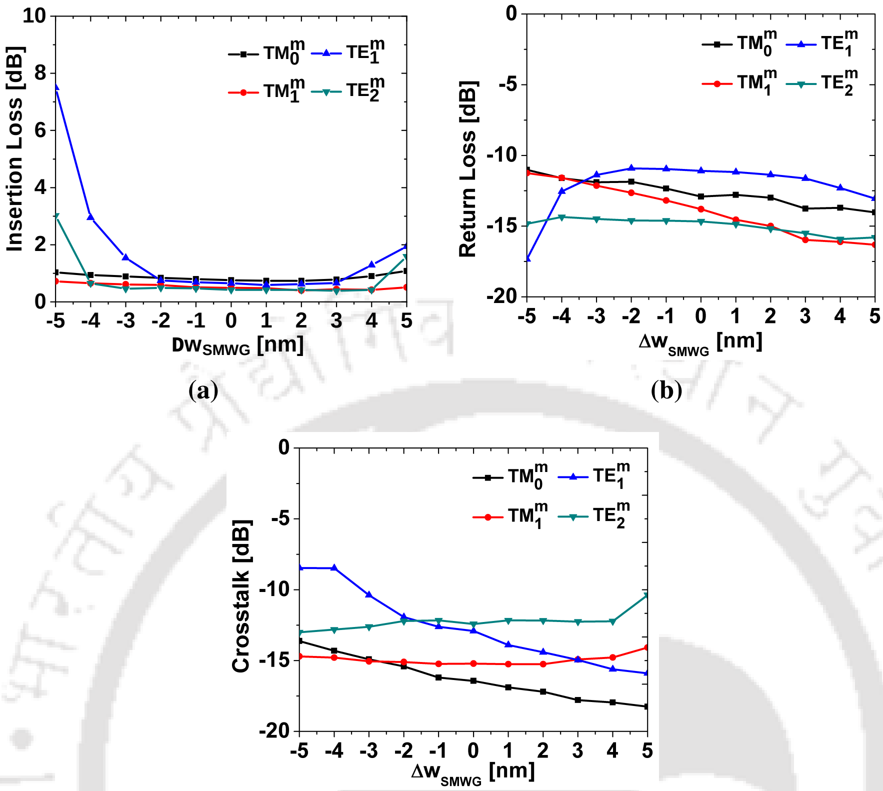

(a) (b)

(c)

Fig. 4.7: Effect of single-mode waveguide width variation on (a) insertion loss, (b) return loss, and (c) crosstalk of the proposed device.

input. It is clear from the figure that the power is transferred from TM_0^m to the fundamental mode TM_0^s of WG_{s1} in the –z direction due to the presence of grating$_1$ in between WG_{s1} and WG_m, which is indicated by the reflection peak around 1550 nm observed at the Port 2. Similarly, when TM_1^m is excited at the input port (Port 1), a reflection peak at Port 6 is seen around 1550 nm, as shown in Fig. 4.6(b), indicating that its power is backward coupled to TM_0^s of WG_{s2}. When the quasi-TE modes are excited at the input port, the modes travel through the TM-MDM region and reach the TE-MDM region without being coupled to any of the modes in the TM-MDM region. When TE_0^m is excited at Port 1, its power remains in the same waveguide WG_m as it propagates through the TE-MDM, TM-MDM regions, and it continues propagating towards the +z direction, as shown in Fig. 4.6(c). For TE_1^m input, its energy is transferred to TE_0^s of WG_{s3} in the –z direction, and as a result, a reflection peak around 1550 nm is observed in the reflection spectrum of Port 3 as shown in Fig. 4.6(d). Similarly, when TE_2^m is fed as input, its power is coupled to backward propagating TE_0^s of WG_{s4} and can be seen as a reflection at Port

5 in Fig. 4.6(e).

The insertion losses at 1550 nm for the inputs TM_0^m, TM_1^m, TE_0^m, TE_1^m, and TE_2^m are 0.76 dB, 0.49 dB, 0.01 dB, 0.65 dB, and 0.42 dB respectively. In general, to reduce the insertion loss in the case of grating-based structures, the coupling length or the grating length is increased such that reflection strength saturates beyond a certain length. In the proposed device, the saturation in reflection strength is observed above 250 μm for TM-MDM and 150 μm for TE-MDM. The crosstalks found are below –16.43 dB, –15.21 dB, –36.10 dB, –12.91 dB, and –12.42 dB for an input of TM_0^m, TM_1^m, TE_0^m, TE_1^m, and TE_2^m respectively. Crosstalks are low due to the high phase mismatch between the uncoupled modes. The crosstalk at Port 4 is excluded in the analysis since it can be nullified when the bus waveguide is linked to a single-mode waveguide with an adiabatic taper. The return losses incurred for TM_0^m, TM_1^m, TE_0^m, TE_1^m, and TE_2^m inputs are –12.91 dB, –13.80 dB, –38.78 dB, –11.23 dB, and –14.66 dB respectively. The magnitude of return loss is minimized by keeping a sufficient distance between the bus waveguide and access waveguides, at which supermode formation is suppressed and less reflection occurs at the input port.

A comparison of the present work with the previous works, which are based on GAC structures, is given in Table 4.1. It can be observed that the proposed device structure presented in this paper can (de)multiplex 5 mode channels (3 TE and 2 TM) with better insertion loss and reasonable return loss values.

Table 4.1: Comparison with previous work

References	**Number of Channels**	**Insertion Loss (dB)**	**Return Loss (dB)**
[173]	2 TE and 1 TM	<3.80	–
[177]	2 TE and 1 TM	<1.91	< -15.50
This work	3 TE and 2 TM	<0.76	< -11.23

The performance variation of the proposed device is studied by changing the single-mode waveguide width (Δw_{SMWG}) while keeping the center-to-center waveguide distance constant. The change in insertion loss, return loss, and crosstalk with the corresponding single-mode waveguide width variation are plotted in Fig. 4.7 for TM_0^m, TM_1^m, TE_1^m, and TE_2^m inputs . A maximum performance degradation of 2.30 dB, 2.22 dB, and 4.43 dB in insertion loss, return loss, and crosstalk respectively has been observed for a deviation of ±4 nm in the single-mode waveguide width (Δw_{SMWG}).

4.5 Summary

A hybrid MDM-PDM device based on the SOI platform at an operating wavelength of 1550 nm has been designed and simulated using 2.5D FDTD. The hybridization is realized by cascading two mode-division multiplexers working in quasi-TE and quasi-TM polarizations. A mathematical model of the proposed device has been presented with the coupled-mode equations and their solutions. The demultiplexing operation has been demonstrated by exciting the individual modes at the input port and observing the power output at their respective ports. The performance of the device in terms of crosstalks, insertion loss, and return loss are found to be <–12.42 dB, <0.76 dB, and <–11.23 dB respectively. The results obtained in the present work has a higher number of channels with reasonably better performance compared to the reported GAC based (de)multiplexers working with dual polarization. A fabrication tolerance study has been presented by varying the waveguide width and keeping the center-to-center waveguide distance constant. The proposed device holds potential for integration with the wavelength division multiplexing scheme to realize a three-dimensional hybrid (de)multiplexing system for a manifold increase in the link capacity of optical networks.

5

Mode and Wavelength Division (De)multiplexer

Contents

5.1 Introduction

A combination of MDM, PDM, and WDM can be implemented to enhance the link capacity of an optical network. In recent years, a rise in interest has been seen in developing a multi-dimensional hybrid multiplexing scheme by combining MDM, PDM, and WDM technologies. PDM, when integrated with MDM or WDM, has the possibility to double the link capacity. A PDM-WDM hybrid (de)multiplexer has been demonstrated in [100], using bi-directional arrayed waveguide grating (AWG) and polarization diversity circuit with 9 wavelength channels and dual polarizations. In [190], an MRR array and polarization-splitter-rotator based 16-channel PDM-WDM hybrid (de)multiplexer has been realized. MDM in association with WDM can increase the link capacity to $m \times n$ data channels, where m is the number of supported modes of the multimode bus waveguide and n is the number of wavelength channels. Previously, various structures such as photonic crystals [191], asymmetric Y-junction [68], ADC assisted AWG [83], MMI with tilt joint phase shifter [192], and ADC assisted MRR [67] have been utilized to demonstrate MDM-WDM hybrid (de)multiplexer.

In this chapter, a hybrid MDM-WDM (de)multiplexer has been proposed using grating assisted contra-directional couplers. The proposed MDM-WDM device is designed on the SOI platform due to its compatibility with the mature CMOS technology. In the last chapter, a 5-channel MDM-PDM hybrid (de)multiplexer with 3 quasi-TE and 2 quasi-TM modes was proposed. Simultaneous contra-directional mode coupling on either side of the bus waveguide with grating-assisted coupler (GAC) based structures helps in reducing the overall lenght of the device. In this chapter, the authors have utilized a GAC based arrangement to implement a hybrid MDM-WDM (de)multiplexer. The proposed MDM-WDM device can (de)multiplex 6 data channels with 3 mode and 2 wavelength channels. The device is comprised of three coupler sections assisted by grating structures. These coupler sections have been designed to contra-directionally couple the fundamental, first, and second-order modes of the bus waveguide to the respective neighboring single-mode waveguides at 1535 nm and 1560 nm wavelengths.

5.2 Device structure and operation principle

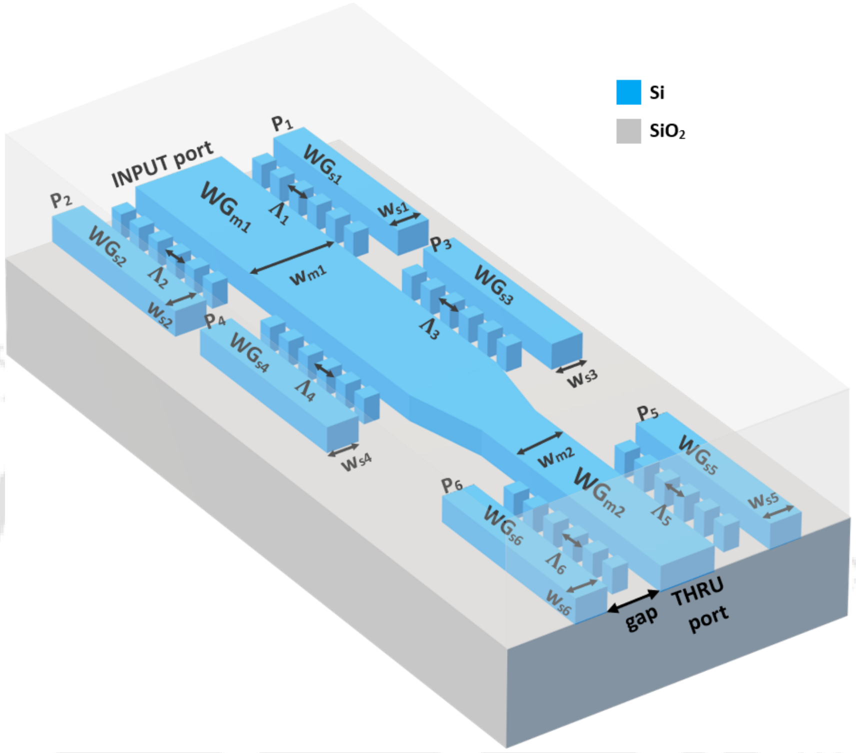

Fig. 5.1: 3D schematic of the proposed device structure.

Figure 5.1 shows the 3D schematic of the proposed MDM-WDM structure. The device is designed using buried channel waveguide structures on the SOI platform with a 2 μm lower cladding layer, 220 nm device layer, and 2 μm upper cladding layer. Si is the material for core, and SiO_2 is the material for upper cladding and lower cladding. The proposed MDM-WDM structure is formed by cascading three grating assisted coupler sections. These sections have a multimode bus waveguide at the middle, which is surrounded by two single-mode waveguides. The bus waveguides of the second and third coupler sections are connected by a low-loss adiabatic taper. In between the bus waveguide and single-mode waveguides, periodic grating structures are placed for contra-directional coupling.

The bus waveguides of the first and second coupler sections have the same width and support three quasi-TE modes, namely TE_{0m} (fundamental), TE_{1m} (first-order), and TE_{2m} (second-order). The fundamental modes of the single-mode waveguides are denoted as TE_{0s}. In the first coupler section, TE_{2m} of WG_{m1} is contra-directionally coupled to TE_{0s} of WG_{s1} and WG_{s2} at two different wavelengths 1535 nm and 1560 nm respectively. Similarly, In the second coupler section TE_{1m} is contra-directionally coupled to TE_{0s} of WG_{s3} and WG_{s4} at 1535 nm and 1560 nm respectively. In the third coupler section, the fundamental mode, TE_{0m} of WG_{m2} is coupled to backward propagating TE_{0s} of WG_{s5} and WG_{s6} at 1535 nm and 1560 nm respectively.

5.3 Design Rules

Figure 5.2 shows the variation of effective indices of various modes supported by a buried channel waveguide with a thickness of 220 nm at 1535 nm and 1560 nm wavelengths. The effective refractive indices of the modes are calculated using the EIM [39]. It can be seen that for the same mode, the effective refractive index is higher for 1535 nm wavelength since the waveguide mode extends more into the cladding with the increase in wavelength due to waveguide dispersion.

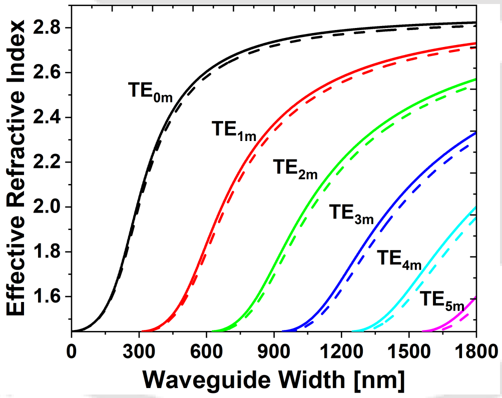

Fig. 5.2: Effective refractive index variation of the quasi-TE modes with the change in waveguide width; solid and dashed lines correspond to 1535 nm and 1560 nm respectively.

The widths of the bus waveguides and single-mode waveguides are chosen such that the coupled modes satisfy the contra-directional phase-matching conditions, given as [188]:

$$\beta_1 + \beta_2 = \frac{2\pi}{\Lambda} \tag{5.1}$$

where β_1, β_2 are the propagation constants of the two coupled modes, and Λ is the period of the grating.

To cater a considerable difference between the effective refractive indices of the modes for

Table 5.1: Device parameters for the porposed structure

Parameter	Value	Parameter	Value
w_{s1}, w_{s4}, w_{s5}	340 nm	Λ_1	334 nm
w_{s2}, w_{s3}	330 nm	Λ_2	344 nm
w_{s6}	350 nm	Λ_3	318 nm
w_{m1}	1400 nm	Λ_4	323 nm
w_{m2}	670 nm	Λ_5	315 nm
gap	350 nm	Λ_6	320 nm

avoiding undesired co-directional coupling, the width of the bus waveguide in the first and second coupler sections (w_{m1}) is taken as 1400 nm, and the width of single-mode waveguides surrounding the bus waveguides are taken as 340 nm (w_{s1} and w_{s4}) and 330 nm (w_{s2} and w_{s3}). The fundamental mode of WG_{m1} is highly confined in the core region, which makes it difficult to couple with the single-mode waveguide. Thus, the WG_{m1} is tapered down to a width of 670 nm bus waveguide (WG_{m2}) using adiabatic taper in order to achieve a substantial spread of the evanescent field in the cladding region for efficient contra-directional coupling. The effective refractive index of the fundamental mode of WG_{m2} matches with the first-order mode of the WG_{m1}. The length of the adiabatic taper section is 3 μm for low loss of the fundamental quasi-TE mode as it propagates from the second coupler section to the third coupler section. To reduce any unwanted back reflections in the third coupler section, the widths of the single-mode waveguides are taken as 340 nm (w_{s5}) and 350 nm (w_{s6}). The gap between the bus waveguide and single-mode waveguides is taken as 350 nm. Figure 5.3 shows a plot of simulated coupling efficiency with varying grating length for different input modes at 1535 nm and 1560 nm . It can be observed that the coupling efficiency increases gradually with the increase in the grating length, however beyond 150 μm the coupling efficiency tends to saturate. Therefore to maintain a good coupling strength and reduce the device length, a grating length of 150 μm has been taken for each of the coupler section. Due to the presence of the adjacent waveguides, the propagation constant of the supported mode changes in the waveguide by a small amount, and thus the required grating period differs slightly from the value obtained from Eqn. (5.1). The device parameters that are used for the simulation are listed in Table 5.1.

Figure 5.4 shows the cross-sectional electric field mode profiles of the coupled modes of

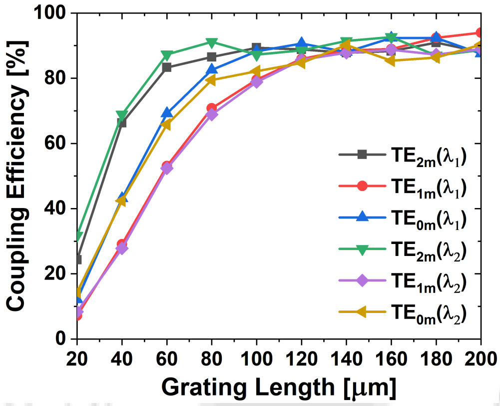

Fig. 5.3: Coupling efficiency for different mode inputs at λ_1 = 1535 nm and λ_2 = 1560 nm with variation in the grating length.

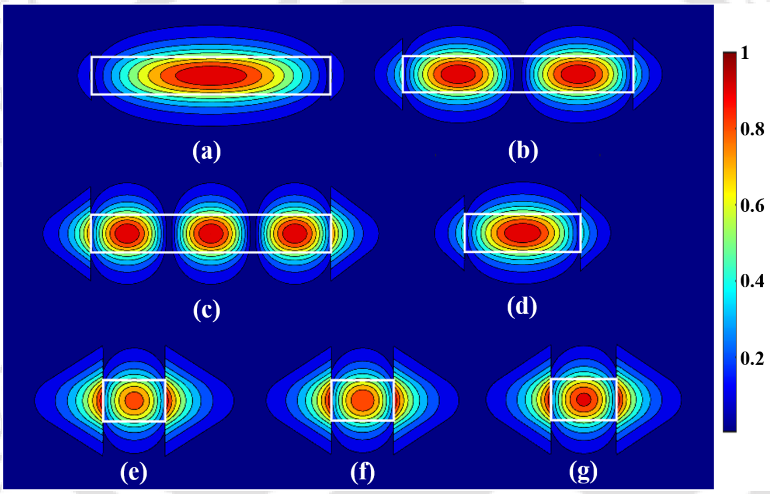

Fig. 5.4: Cross-sectional electric field mode profiles of the waveguides. The white rectangle shape represents cross-section of the waveguides.

the different waveguides, which are obtained using EIM. The mode profiles of TE_{0m}, TE_{1m}, and TE_{2m} of WG_{m1} are shown in Fig. 5.4(a), (b), and (c) respectively. Figure 5.4(d) shows the mode profile of the fundamental mode of WG_{m2}, whereas Fig. 5.4(e), (f), and (g) show the fundamental mode profile of $WG_{s2/s3}$, $WG_{s1/s4/s5}$, and WG_{s6} respectively.

The second and third coupler sections are connected via a taper. This taper needs to be a low-loss adiabatic taper. A 2.5D FDTD simulation is performed for the taper section with a 3 μm taper length, and the resulting transmittance and loss are plotted in Fig. 5.5. It can be observed that 3 μm length taper is suitable for low-loss transition from the TE_{0m} of WG_{m1} to TE_{0m} of WG_{m2}.

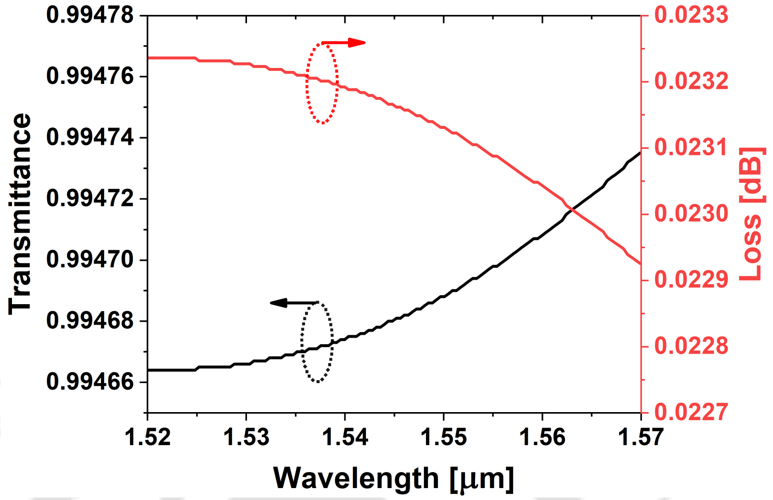

Fig. 5.5: Transmittance and loss plot for TE_{0m} of WG_{m1} to TE_{0m} of WG_{m2} transition in a 3 μm tapered waveguide.

5.4 Simulation Results

The 2.5D FDTD simulation, which is a combination of EIM and 2D FDTD, has been performed to examine the performance of the proposed device. A detailed description of the 2.5D FDTD technique is provided in section 4.4. To study the demultiplexing operation, TE_{0m}, TE_{1m}, and TE_{2m} of WG_{m1} are excited independently at the input port, and output spectra are observed at all the output ports. For simplicity and to reduce simulation run-time, each grating coupler section is simulated separately, and the results have been concatenated to obtain the overall output of the device. The output spectra for each input mode are shown in Fig. 5.6. Figure 5.6(a) shows the transmission/reflection spectrum at the output ports when TE_{2m} is excited as input. It can be observed that there are two reflection peaks at 1535 nm and 1560 nm, but at two different ports P_1 and P_2 respectively, indicating that 1535 nm is reflected back at P_1 and 1560 nm is reflected back at P_2. Similarly, for TE_{1m} input, power is coupled to the WG_{s3} and WG_{s4} at P_3 (1535 nm) and P_4 (1560 nm) respectively, which can be observed from Fig. 5.6(b). When TE_{0m} is excited at the input, it propagates through the first and second coupler sections since it does not satisfy the coupling condition in these two coupler sections. The TE_{0m} is then converted to the fundamental mode of WG_{m2} via an adiabatic taper. Its power is coupled to fundamental modes of WG_{s5} and WG_{s6} at P_5 (1535 nm) and P_6 (1560 nm) respectively, which is evident from Fig. 5.6(c).

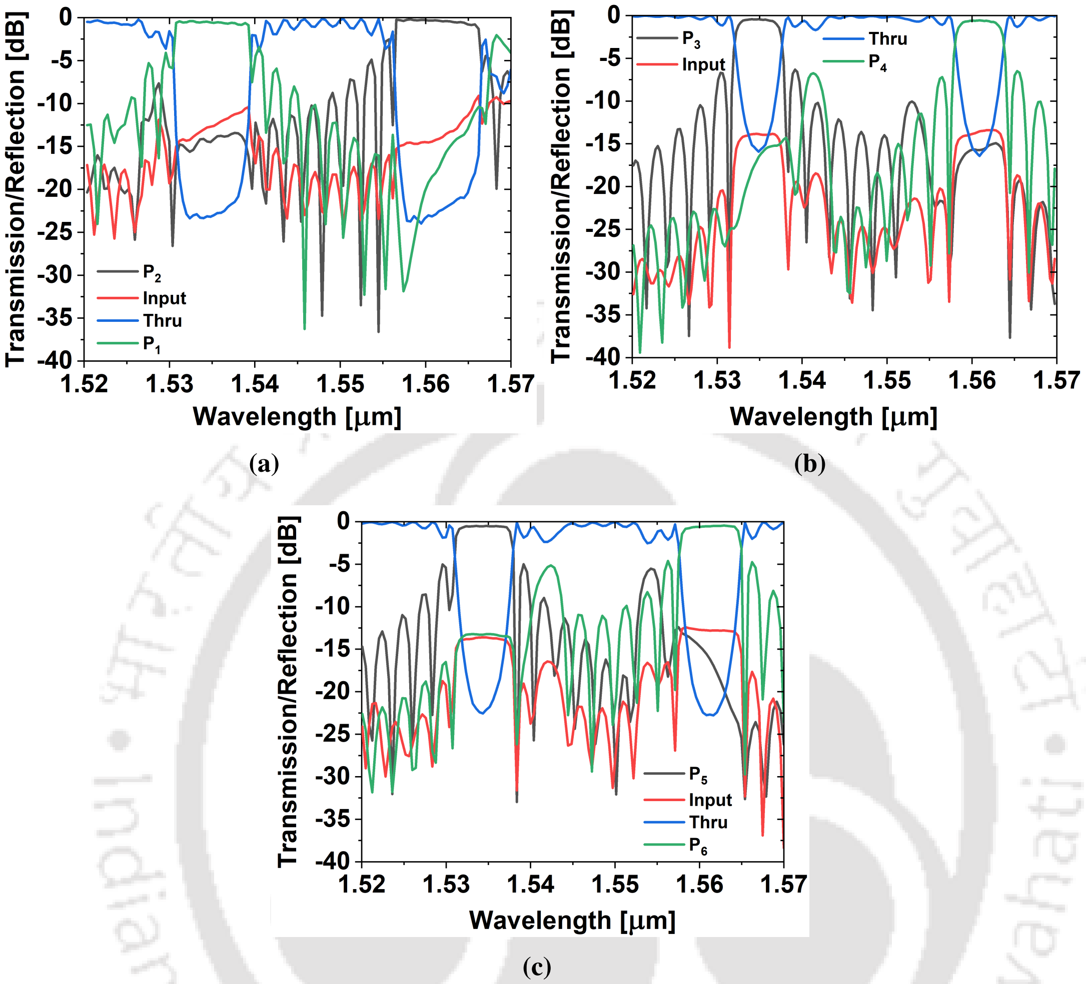

(a) (b)

(c)

Fig. 5.6: Transmission/Reflection spectra when the input is (a) TE$_{2m}$, (b) TE$_{1m}$, and (c) TE$_{0m}$.

The resulting IL, RL, and CT for different input modes are given in Table 5.2. From the table it can be observed that the IL, RL, and CT are <0.55 dB, <–12.81 dB, and <–12.74 dB for the proposed MDM-WDM device, respectively. A comparison with the previously reported MDM-WDM devices is given in Table 5.3. It can be observed that in comparison with [192] and [193], the proposed device shows better IL, i.e., IL <0.55 dB with 3 mode and 2 wavelength channels.

Figure 5.7 shows the simulated light propagation of the TE$_{2m}$, TE$_{1m}$, and TE$_{0m}$ modes when they are individually excited at the input port. It can be visually interpreted from the figure that for TE$_{2m}$, TE$_{1m}$, and TE$_{0m}$ inputs the power is backward coupled to the ports P$_1$, P$_3$, and P$_5$ (P$_2$, P$_4$, and P$_6$), respectively at 1535 nm (1560 nm).

To carry the demultiplexed signals further, bent waveguides can be connected at the ports

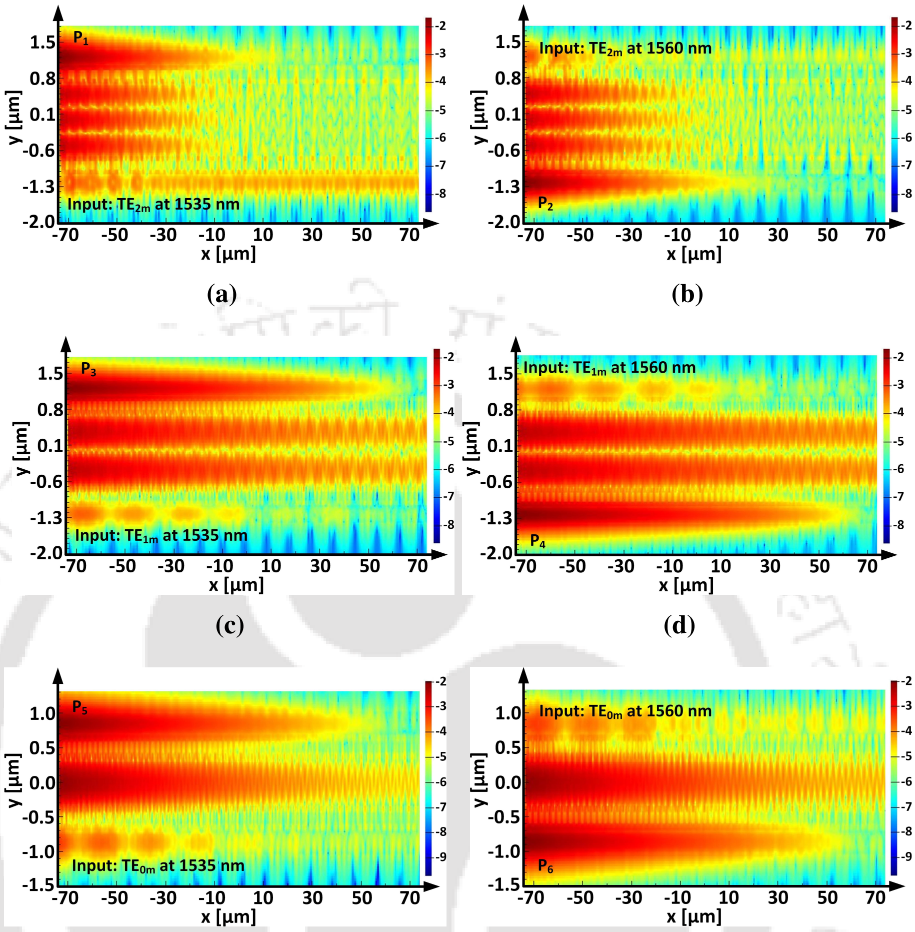

(a) (b)

(c) (d)

(e) (f)

Fig. 5.7: Simulated light propagation (poynting vector) showing the backward coupling of TE_2^m at (a) 1535 nm and (b) 1560 nm, TE_1^m at (c) 1535 nm and (d) 1560 nm, TE_0^m at (e) 1535 nm and (f) 1560 nm in the three grating assisted coupler sections.The plots are in logarithmic scale.

Table 5.2: Performance of the proposed MDM-WDM device at λ_1 = 1535 nm and λ_2 = 1560 nm

Mode	**IL (in dB)**	**RL (in dB)**	**CT (in dB)**
TE_{2m} (λ_1)	0.55	–12.83	< –13.48
TE_{2m} (λ_2)	0.34	–13.49	< –18.86
TE_{1m} (λ_1)	0.43	–13.86	< –16.09
TE_{1m} (λ_2)	0.55	–13.54	< –15.18
TE_{0m} (λ_1)	0.53	–13.62	< –12.74
TE_{0m} (λ_2)	0.54	–12.81	< –15.61

P_3, P_4, P_5, and P_6. It has been observed that by taking a bending radius of 5 μm, the demultiplexed signals can be carried forward with a loss of <0.054 dB. Considering these bent waveguide sections, the overall length of the device becomes 463 μm. The proposed device can be fabricated on SOI platform (2 μm SiO_2 BOX layer and 220 nm Si device layer) using

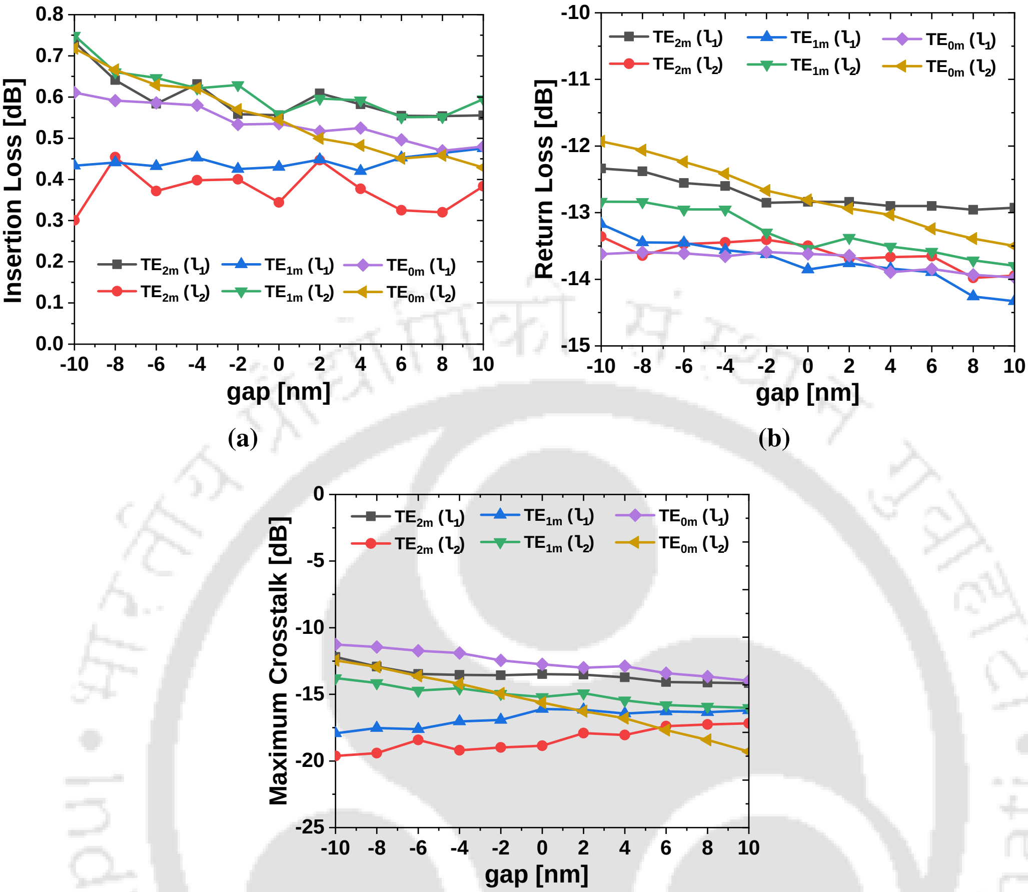

(a) (b)

(c)

Fig. 5.8: Change in (a) IL, (b) RL, and (c) maximum CT with variation in the gap; λ_1 = 1535 nm and λ_2 = 1560 nm.

Table 5.3: Comparison with previous work

Reference	Structure	Number of Channels	Insertion Loss (dB)
[192]	MMI	2 TE and 3 λ	<0.99
[193]	Photonic crystal	2 TM and 2 λ	<1.09
This work	GAC	3 TE and 2 λ	<0.55

electron beam lithography for patterning, followed by inductively coupled plasma reactive ion etching and plasma-enhanced chemical vapor deposition process for the deposition of the upper cladding layer. The fabrication tolerance of the proposed MDM-WDM device has been analyzed by varying the gap between the respective single-mode waveguide and the multimode bus waveguide to study the effect on the device performance. The change in IL, RL, and maximum CT with the gap variation is plotted in Fig. 5.8. It can be observed that the IL, RL, and maximum CT stay within the range of 0.30 dB to 0.74 dB, –14.32 dB to –11.93 dB, and –19.62 dB to –11.26 dB, respectively for a gap variation of ±10 nm. Thus the proposed device shows good fabrication tolerance over ±10 nm gap variation.

5.5 Summary

A 6-channel hybrid MDM-WDM device based on the SOI platform has been proposed. It can simultaneously (de)multiplex three modes at 1535 nm and 1560 nm wavelengths. The proposed device has been designed using the 2.5D FDTD simulation method. The operation of the MDM-WDM device involves the launching of the fundamental, first-order, and second-order quasi-TE modes of the multimode bus waveguide at the input port. These modes are contra-directionally coupled to their respective output ports through the grating structures, which are placed in between the bus waveguide and single-mode waveguides. The overall device length of the MDM-WDM structure is 463 μm considering bent waveguide sections. The proposed device exhibits an insertion loss of <0.55 dB, return loss of <–12.81 dB, and crosstalk of <–12.74. The fabrication tolerance has also been studied by observing the variation in device performance while the gap between the respective single-mode waveguide and the multimode bus waveguide is varied by ±10 nm. The presented MDM-WDM device can be extended by adding the polarization division multiplexing scheme to double up the overall link capacity.

6

Mode, Polarization, and Wavelength Division (De)multiplexer

Contents

6.1 Introduction

Recently, due to high bandwidth and high capacity demands, various hybrid multiplexing technologies have attracted a lot of attention which can be developed by combining two multiplexing technologies, such as mode and polarization [187, 194], mode and wavelength [144, 192, 195], and also wavelength and polarization division multiplexing [100, 190]. However, currently it is essential to focus more on developing hybrid multiplexing techniques which will combine all three degrees of freedom for further improvement in the optical link capacity. Yu He et al. have demonstrated a hybrid mode, polarization, and wavelength division multiplexer using subwavelength grating structures for contra-directional coupling of the waveguide modes [37].

In this chapter, a silicon hybrid mode, polarization, and wavelength division (de)multiplexer is proposed, where twelve channels comprising of three modes, two polarization, and two wavelengths can be used for data communication. The device has three coupling sections, consisting of a middle bus waveguide and two neighbouring single-mode access waveguides with periodic grating structures in between. Each of the coupling sections is dedicated for coupling of a particular order and polarization mode of the bus waveguide to the respective fundamental mode of the access waveguide. The contra-directional mode coupling is achieved by satisfying the phase-matching condition. The simulation result shows that the designed device exhibits low insertion loss, return loss and crosstalk at 1550 nm and 1560 nm.

6.2 Device Structure and Operation

The top view of the proposed device structure is shown in Fig. 6.1. The design is based on SOI waveguides with 220 nm thickness, 2 μm buried oxide, and 2 μm top silica cladding. The device structure is divided into three coupling sections (A, B, and C), where each section is dedicated for contra-directional coupling of a particular order of the guided TM and TE modes. Each section consists of two coupling regions where modes of the bus waveguides are coupled to modes of the adjacent single-mode waveguides. In Section A (Section B), the coupling regions A_1 and A_2 (B_1 and B_2) consist of a common multimode bus waveguide and two single-mode

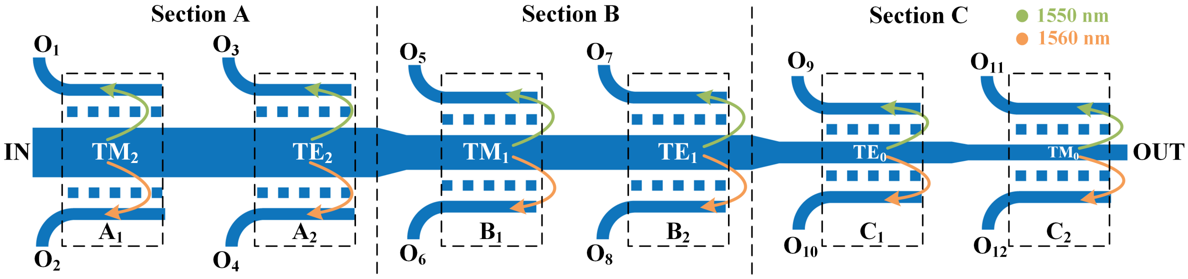

Fig. 6.1: Top view schematic of the proposed MDM-PDM-WDM device structure

access waveguides, which are placed on either side of the bus waveguide. Whereas, in Section C, the coupling regions C$_1$ and C$_2$ also consist of a bus waveguide and two adjacent access waveguides but with different bus waveguide width. The bus waveguides in Section A and B are denoted as WG$_A$ and WG$_B$, respectively. Section C has two bus waveguides which are denoted as WG$_{C1}$ and WG$_{C2}$. The bus waveguides of Sections A, B, and C support three, two, and one TM/TE modes, respectively. The input port is denoted as IN, and the output ports are denoted as O$_i$, where i = 1 to 12. The width of the bus waveguides in the coupling regions are denoted as w_A, w_B, w_{C1}, and w_{C2}, whereas the width of the single-mode access waveguides is denoted as w_{Oi} which corresponds to the ith output waveguide. The gap between the bus waveguide and the access waveguides is denoted as g_i, whereas the width and period of the associated grating structure is represented as gw_i and Λ_i, respectively. The periodic grating structures are placed at the mid-position in the gap between access and bus waveguides. The fundamental, first, and second-order TM and TE modes are excited independently at the input port IN. In Section A, the second-order TM (TE) mode, TM$_2$ (TE$_2$), is contra-directionally coupled to the fundamental TM modes of neighbouring single-mode waveguides and reflected back towards output ports O$_1$ and O$_2$ (O$_3$ and O$_4$) at 1550 nm and 1560 nm, respectively. Similarly, in Section B, the first order TM (TE) mode, TM$_1$ (TE$_1$), is reflected at 1550 nm and 1560 nm at output ports O$_5$ and O$_6$ (O$_7$ and O$_8$), respectively. The adiabatic tapers are used to interconnect the bus waveguides of Sections A, B, and C. In Section C, coupling regions C$_1$ and C$_2$ have different bus waveguide widths, which are connected via an adiabatic taper. For the fundamental TE (TM) mode input, the power is coupled to the single-mode waveguides in the backward direction along the port O$_9$ and O$_{10}$ (O$_{11}$ and O$_{12}$) at 1550 and 1560 nm, respectively.

6.3 Design Rules

The guide mode effective indices are calculated using an eigenmode solver. The Palik model of Si and SiO_2 are used to incorporate the material dispersion. A mode chart showing the change in effective index with the waveguide width is plotted in Fig. 6.2. The number of guided modes increases with the increase in the waveguide width. In each of the coupling regions, the width of the waveguides and the corresponding grating period are chosen such that the governing phase-matching condition for the contra-directional coupling is satisfied, which can be defined as

$$n_1(\lambda) + n_2(\lambda) = \frac{\lambda}{\Lambda} \tag{6.1}$$

where n_1, n_2 are the wavelength dependent effective indices of the coupled modes, λ is the wavelength of interest, and Λ is the period of the grating structure placed between the two waveguides.

The widths of the bus waveguides are taken as $w_A = 2\ \mu$m, $w_B = 1.5\ \mu$m, $w_{C1} = 1\ \mu$m, and

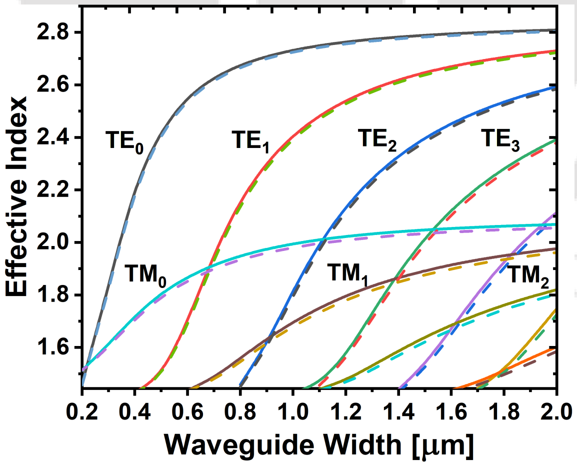

Fig. 6.2: Mode chart for the 220 nm thick SOI waveguide at 1550 nm (solid lines) and 1560 nm (dashed lines).

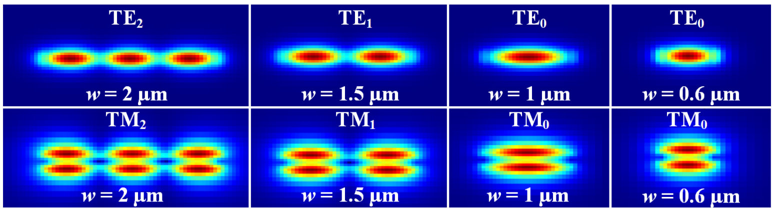

Fig. 6.3: Cross-sectional mode profile of the TE and TM modes.

w_{C2} = 0.6 μm, such that WG$_A$, WG$_B$, and WG$_{C1/C2}$ support three, two, and one guided TM/TE modes, respectively. The three adiabatic linear tapers t$_1$, t$_2$, and t$_3$, each of length 10 μm, are used for the low loss mode transition from WG$_A$ to WG$_B$, WG$_B$ to WG$_{C1}$, and WG$_{C1}$ to WG$_{C2}$, respectively. For TM mode coupling regions, the widths of the single mode access waveguides are 350 nm and 400 nm, whereas for TE mode coupling regions, the widths are 400 nm and 500 nm for two different wavelengths. The access waveguide widths are taken different in order to avoid undesired mode coupling and back reflections. The mode profiles of the guided TE and TM modes in the corresponding bus waveguides are shown in Fig. 6.3. In the TM mode coupling regions, the grating structures placed on either side of the bus waveguide are out of phase by 180° for better mode coupling. The periods of the grating structures are selected to satisfy the contra-directional phase-matching condition between the respective coupled modes. In addition, the gap between the access and bus waveguide is higher compared to the TE coupling regions since the TM evanescent fields extend farther and cause undesired co-directional coupling at short separation distances. The length of each coupling region is taken to be 400 μm for the highest achievable reflection at the target output port. The device parameters taken for the simulation are tabulated in Table 6.1.

6.4 Simulation Results

The proposed MDM-PDM-WDM device has been numerically simulated using the full vectorial 3D FDTD method in Ansys Lumerical FDTD software. To reduce simulation runtime,

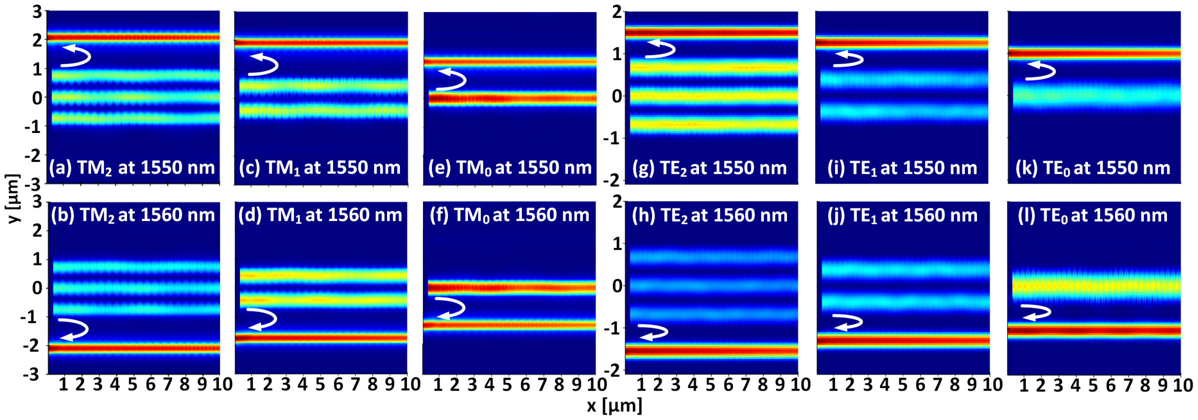

Fig. 6.4: Mode Propagation (Poynting vector) of the TE/TM modes at 1550 and 1560 nm.

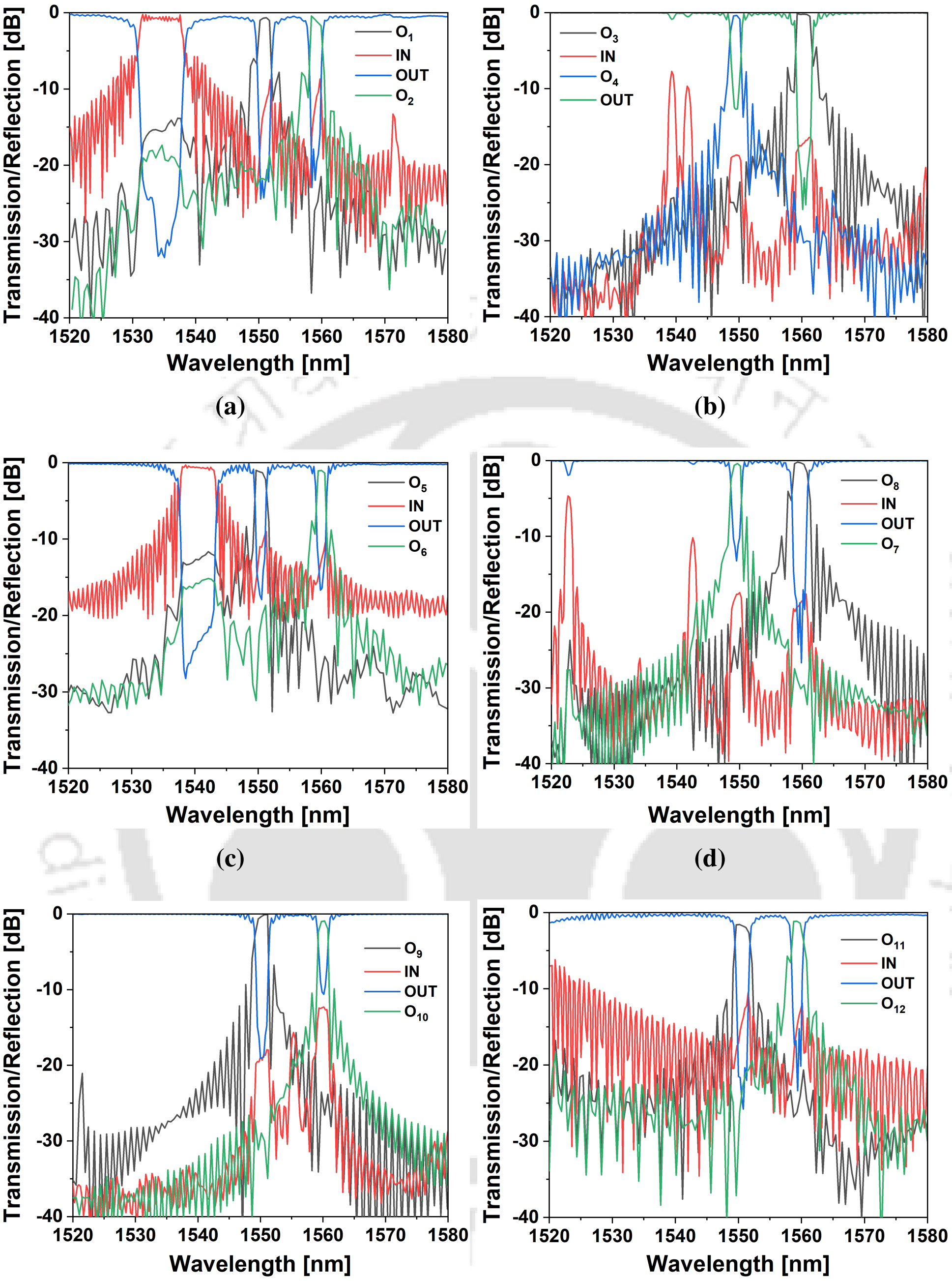

(a) (b)

(c) (d)

(e) (f)

Fig. 6.5: Transmission/Reflection spectrum at the input and output ports for mode inputs of (a) TM_2, (b) TE_2, (c) TM_1, (d) TE_1, (e) TE_0, and (f) TM_0.

only the coupling regions have been simulated, and to get the response of the entire device structures, the results of each coupling region have been concatenated. A nonuniform mesh is used for the simulation. The length of the simulation domain is equal to the coupling length of the corresponding coupling region, while the simulation width and height are taken as 5 μm and 2 μm, respectively. Simulation is executed by injecting the TE/TM modes at the input and

Table 6.1: Device parameters

Parameter	**Value (nm)**	**Parameter**	**Value (nm)**
w_{O1}, w_{O5}, w_{O9}, w_{O11}	350	Λ_3	318
w_{O2}, w_{O3}, w_{O6}, w_{O7}, w_{O10}, w_{O12}	400	Λ_4	320
w_{O8}, w_{O4}	500	Λ_7	315
g_1, g_2	900	Λ_5, Λ_6, Λ_{11}, Λ_{12}	440
g_3, g_4, g_7, g_8, g_9, g_{10}, Λ_8	300	Λ_9	306
g_5	1000	Λ_{10}	297
g_6, g_{11}, g_{12}	800	w_A	2000
Λ_1, Λ_2	450	w_B	1500
w_{C1}, w_{C2}, gw_1, gw_2	600	L_c	4×10^5
t_1, t_2, t_3	10000	gw_5, gw_{11}, gw_{12}	650
gw_6	450	gw_3, gw_4, gw_7, gw_8, gw_9, gw_{10}	180

observing the transmission or reflection spectrum at the input and output ports. The simulated propagation of the three TE modes and three TM modes at 1550 nm and 1560 nm have been shown in Fig. 6.4. The power transfer between the coupled modes can be observed in the respective coupling regions. The resulting transmission or reflection spectrum for the corresponding input modes has been shown in Fig. 6.5. In Fig. 6.5(a), two reflection peaks (at 1550 nm and 1560 nm) can be seen in the spectrum, which indicates power coupling between the TM_2 mode and fundamental modes of WG_{O1} and WG_{O2}. Similarly, for the TE_2 mode input, reflections are obtained at the output ports O_3 (at 1550 nm) and O_4 (at 1560 nm), as observed in Fig 6.5(b). For the remaining first and zeroth order mode inputs, the power is contra-directionally coupled to the respective output ports, which can be seen in Fig. 6.5(c)-(f).

The IL for TE mode inputs are found to be <0.38 dB and <0.93 dB, whereas, for TM mode inputs, IL is <1.56 dB and <1.12 dB at 1550 and 1560 nm, respectively. The return loss for TE and TM mode inputs are <–17.65 dB and <–12.90 dB (<–12.29 dB and <–12.22 dB) at 1550 nm (1560 nm). The highest crosstalk of –26.25 dB for TE mode excitation is observed in the output port O_4 at 1550 nm for TE_2 mode input, whereas in the case of TM mode inputs, the highest crosstalk of –21.74 dB is detected in port O_2 at 1550 nm.

Table 6.2: Comparison with literature

References	Number of Channels	IL (dB)
[196]	10 (10 modes)	<0.46
[195]	6 (3 modes, 2 wavelengths)	<0.55
[37]	8 (2 modes, 2 polarization, and 2 wavelengths)	<1.5
This work	12 (3 modes, 2 polarization, and 2 wavelengths)	<1.56

For fabrication tolerance study, the grating period is varied in each of the coupling sections, and a shift in coupling wavelength for each of the modes is observed. Fig. 6.6 shows that an increase in the grating period results in a redshift of the transmission/reflection spectrum, while a decrease in the grating period results in a blue shift. For a ±2 nm change in the grating period, a maximum of ±7 nm shift is observed in the spectrum with similar device performance at the corresponding coupling wavelength. A comparison of the designed device with the reported devices is shown in Table 6.2. It can be observed that the proposed device has a higher number of data channels with good performance.

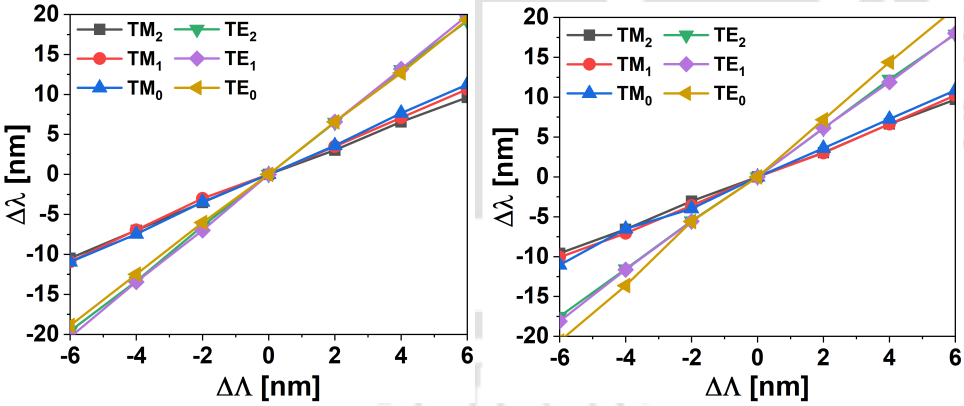

(a)

(b)

Fig. 6.6: Variation in coupling wavelength with change in grating period at (a) 1550 nm and (b) 1560 nm.

6.5 Summary

The design of a 12-channel hybrid mode-, polarization-, and wavelength-division (de)multiplexer has been demonstrated on the SOI platform. Three TE modes and three TM modes of the bus waveguide are exploited at two wavelengths (1550 and 1560 nm) to be used as data-carrying channels. The proposed device consists of six coupling regions and three linear adiabatic tapers. The total length of the device is ~2500 μm when all the coupling regions are connected in series; however, with the use of U-bends, the length can be drastically reduced. The proposed (de)multiplexer exhibits insertion loss <1.56 dB, return loss <–12.22 dB, and crosstalk <–21.74 dB, at 1550 and 1560 nm. The fabrication tolerance study shows a maximum of ±7 nm shift in the spectrum for a ±2 nm variation in the grating period.

7

Conclusions and Future Scope

Contents

7.1 Conclusions

In conclusion, a review of the findings during this thesis work can be presented as below.

1. **Numerical design and analysis of a 3-channel grating assisted mode-division (de) multiplexer**

   A grating assisted slab waveguide structure has been designed to (de)multiplex three TE modes at 1550 nm wavelength. Two gratings with different periods have been placed at both sides of the multimode waveguide to contra-directionally couple first order and second order modes to the fundamental mode of two single mode waveguides. The fundamental mode of the multimode waveguide is not coupled to any other mode. The waveguide widths are obtained from the mode chart and the inter waveguide gaps have been determined such that return loss is minimized, which occurs mainly due to the supermode formation. The proposed device structure has shown insertion loss ranging from 0.43 to 1.27 dB, return loss from –12.73 to –8.65 dB, and crosstalk from –31.20 to –15.31 dB with a device length of 38.5 μm. This mode-division multiplexer can be integrated with polarization division multiplexer or wavelength division multiplexer for further increase in the link capacity.

2. **Numerical modeling and analysis of a TM mode-division (de) multiplexer based on grating assisted couplers**

   A mode-division (de)multiplexer is proposed and designed using slab waveguides with Si as core and SiO_2 as cladding. The device is able to (de)multiplex three TM modes at the operating wavelength of 1550 nm. It simultaneously reflects two higher-order modes when it works as a demultiplexer and combines them during multiplexing, whereas the fundamental mode of the multimode waveguide is not coupled and hence continues forward propagation in the same waveguide. The aspect of supermodes for determining the suitable gap between the waveguides has been introduced to minimize the return loss. The proposed device is compact in size with a dimension of ~2.1 μm × 58 μm. The device performance has been analyzed using 2D FDTD. The insertion loss during demultiplexing is found to be in the range of 0.01 to 2.01 dB, whereas the crosstalks and return loss are in the range of –41.76 to –13.58 dB and –31.07 to –9.17 dB respectively. While multiplexing operation, the insertion loss ranges from 0.01 to 1.59 dB, the return loss is in the range of –31.07 to –10.17 dB, and the crosstalk ranges from –41.76 to –8.05 dB. From the tolerance study it has been observed that the reflection strength falls below –3 dB when the gap between the waveguides is varied more than ±20 nm.

3. **SWG-based compact broadband two-mode TM multiplexer**

   A compact two-mode silicon optical multiplexer is reported using subwavelength grating (SWG) structures. The coupler section in the proposed device consists of an SWG-based access waveguide and a multimode strip bus waveguide. Tapers have been employed for adiabatic transition of the fundamental TM modes of the input strip waveguides to the respective fundamental TM modes of the SWG-based waveguide and multimode strip waveguide. The duty cycle and grating period are tailored to couple the first-order TM mode of the strip waveguide and the fundamental TM mode of the SWG-based waveguide. A 3D finite-difference time-domain simulation is performed to study the device performance. The multiplexer is very compact with a device length of 26 μm, which exhibits a return loss of <–35.62 dB, crosstalk of <–33.60 dB, and insertion loss of <0.29 dB, at 1550 nm.

4. **SWG-based Silicon TE MDM for C + L band operation**

   An SWG based multiplexer on a silicon photonics platform is proposed, which is capable of multiplexing three transverse electric modes. The designed multiplexer is simulated using a 3D FDTD solver and shows broadband operation over the whole C and L optical telecom bands from 1530 nm to 1625 nm wavelength range. The effective indices of the Bloch modes in the SWG waveguides are extracted from the band structure plot.The designed MUX consists of two codirectional coupling regions for fundamental to higher-order mode coupling, with each coupling stage consisting of single-mode and multimode SWG waveguides. The transmission characteristics, viz. transmittance, insertion loss, and return loss are presented and discussed. The coupling lengths without the tapering regions for TE_0–TE_1 and TE_0-TE_2 mode couplings are 14 μm and 1.48 μm, respectively.

The transmittance is >78% with the highest insertion loss and return loss of 1.1 dB and –15 dB, respectively. At 1550 nm, the transmission is > 88%, insertion loss is >–0.6 dB, and return loss is <–15 dB. A uniform under-etch and over-etch of 5 nm are taken for the fabrication tolerance study, which shows maximum variation of 0.58 dB for the insertion loss with return loss <–14.6 dB at 1550 nm. Over the whole simulated range, the insertion loss is <1.4 dB and return loss is <–14.6 dB with ±10 nm change in device dimension.

5. **Design and analysis of a grating assisted hybrid mode and polarization division (de) multiplexer**

   A 3D hybrid MDM-PDM (de)multiplexer is designed, which is based on the CMOS compatible SOI platform with buried strip waveguides. 2.5D FDTD technique, a combination of effective index method (EIM) and 2D FDTD, is employed to design and analyze the performance of the device. A TE-MDM and a TM-MDM are cascaded together to build a hybrid MDM-PDM (de)multiplexer such that both polarizations are used to increase the number of data channels. Simultaneous (de)multiplexing of three quasi-TE modes and two quasi-TM modes of the bus waveguide is achieved with an insertion loss of <0.76 dB, return loss of <–11.23 dB, and crosstalk of <–12.42 dB. The fabrication tolerance has been studied to analyze the performance degradation of the proposed device with waveguide width variation.

6. **Design of a hybrid mode and wavelength division (de) multiplexer based on contra-directional grating assisted couplers on the SOI platform**

   A 6-channel hybrid MDM-WDM device based on the SOI platform has been proposed. It can simultaneously (de)multiplex three modes at 1535 nm and 1560 nm wavelengths. The proposed device has been designed using the 2.5D FDTD simulation method. The operation of the MDM-WDM device involves the launching of the fundamental, first-order, and second-order quasi-TE modes of the multimode bus waveguide at the input port. These modes are contra-directionally coupled to their respective output ports through the grating structures, which are placed in between the bus waveguide and single-mode waveguides. The device length is 463 μm considering bent waveguide sections. The proposed device exhibits an insertion loss of <0.55 dB, return loss of <–12.81 dB, and crosstalk of <–12.74. The fabrication tolerance has also been studied by observing the variation in device performance while the gap between the respective single-mode waveguide and the multimode bus waveguide is varied by ±10 nm.

7. **Design of a Grating Assisted Silicon MDM-PDM-WDM**

   A 12-channel hybrid mode-, polarization-, and wavelength-division (de)multiplexer has been presented. The proposed device is designed on silicon-on-insulator platform. The device structure constitutes three coupling sections with a bus waveguide at the middle and two single mode waveguides on each side. The periodic grating structures are present in between the waveugides for contra-directional coupling of the three TE modes and three TM modes of the bus waveguide to respective fundamental modes of the single-mode waveguides at 1550 and 1560 nm. The device is simulated using 3D finite difference time domain technique and the resulting insertion loss, crosstalk, and return loss are <1.56 dB, <–12.22 dB, and <–21.74 dB respectively. Moreover, the period of the grating structures are varied to perform the fabrication tolerance study.

7.2 Future scope

This thesis explores various multiplexing techniques for improving the link capacity of optical interconnects on SOI platform using periodic grating structures. The thesis has delved into the objective of developing hybrid multiplexing techniques by integrating two or more multiplexing schemes simultaneously. The work presented in this thesis can be expanded into the following potential directions.

1. System level implementation and performance analysis of the designed (de)multiplexers.
2. Validation of the design concepts and working of the proposed device structures through fabrication and characterization.
3. The presented hybrid (de)multiplexers can be improved by accommodating more number of wavelength channels as well as mode channels, however the complexity will increase with the addition of more channels.

4. For further improvement in the integration density and data capacity, the present work can be extended for the implementation in 3D photonics integrated circuits .
5. The multiplexer design can be explored on Silicon Nitride platform for data communication in 500–1100 nm wavelength range.
6. Photonic crystal and SWG based devices are a promising candidate to realize hybrid (de)multiplexers, which can be explored.
7. With increasing hybridization complexity, optimized design techniques must be employed to improve coupling efficiency and reduce crosstalk between the interconnects.
8. As silicon has high thermo-optic coefficient, the Bragg grating based (de)multiplexers can be thermally tuned to operate at a different wavelength.

A

Appendix

A.1 Slab Waveguide

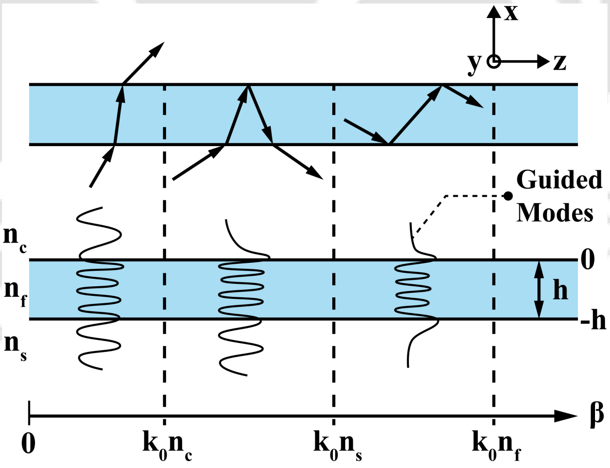

Fig. A.1: Planar slab waveguide structure with electric field profile for guiding of light [181].

The slab waveguide, shown in Figure A.1, consists of a high index dielectric layer with a thickness h surrounded by lower index material on either side. The slab is infinite in extent in the yz plane, and finite in the x direction. The refractive index of core, cladding, and substrate are denoted as n_f, n_c, and n_s respectively. In order for total internal reflection (TIR) to occur at the interfaces, the refractive indices of the layers are chosen such that n_f is greater than n_s and n_c. Only a discrete number of modes are guided by the waveguide structure. Transverse electric (TE) and transverse magnetic (TM) are the two possible electric field polarization. For the mode to be guided it must have oscillatory field in the core and exponentially decaying field in the cladding and substrate region. Thus the electric field amplitudes in the three layers for TE mode are [181]:

$$E_y(x) = Ae^{-\gamma_c x}, \text{ cladding layer} \tag{A.1}$$

$$E_y(x) = Bcos(\kappa_f x) + Csin(\kappa_f x), \text{ core layer} \tag{A.2}$$

$$E_y(x) = De^{-\gamma_s(x+h)}, \text{ substrate layer} \tag{A.3}$$

where A, B, C, D are amplitude coefficients which can be determined from the boundary conditions. γ_c and γ_s are the attenuation coefficients in the cladding and substrate layer respectively. κ_f is the transverse component of the wave vector k in the core. After applying boundary conditions at both the interface a transcendental equation is obtained:

$$tan(h\kappa_f) = \frac{\gamma_c + \gamma_s}{\kappa_f\left[1 - \frac{\gamma_c\gamma_s}{\kappa_f}\right]} \tag{A.4}$$

Numerically solving this transcendental equation will give solutions for propagation constant β of the allowed TE modes for propagation in the waveguide. Similarly for the TM case, the propagation constant of the supported modes can be found from solving the transcendental

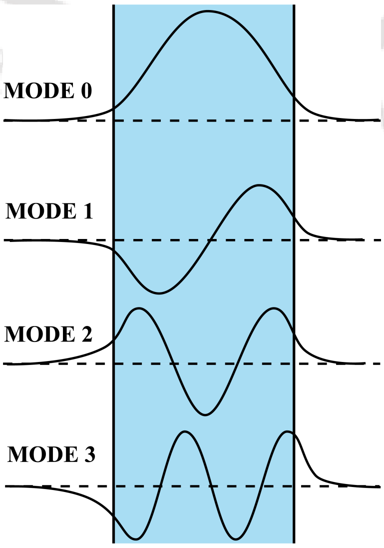

Fig. A.2: Mode field patterns of the first four TE modes.

equation:

$$tan(h\kappa_f) = \frac{\kappa_f\left[\frac{n_f^2}{n_s^2}\gamma_s + \frac{n_f^2}{n_c^2}\gamma_c\right]}{\kappa_f^2 - \frac{n_f^2}{n_c^2 n_s^2}\gamma_c\gamma_s} \tag{A.5}$$

The mode field patterns for the first four TE modes of a waveguide are shown in Fig. A.2.

Bibliography

[1] A. Biberman and K. Bergman, “Optical interconnection networks for high-performance computing systems,” *Reports on Progress in Physics*, vol. 75, no. 4, p. 046402, 2012.

[2] A. Shacham, K. Bergman, and L. P. Carloni, “Photonic networks-on-chip for future generations of chip multiprocessors,” *IEEE Transactions on Computers*, vol. 57, no. 9, pp. 1246–1260, 2008.

[3] A. V. Krishnamoorthy and K. W. Goossen, “Optoelectronic-vlsi: Photonics integrated with vlsi circuits,” *IEEE Journal of Selected Topics in Quantum Electronics*, vol. 4, no. 6, pp. 899–912, 1998.

[4] S. C. Nicholes, M. L. Masanovic, B. Jevremovic, E. Lively, L. A. Coldren, and D. J. Blumenthal, “An 8×8 inp monolithic tunable optical router (motor) packet forwarding chip,” *Journal of Lightwave Technology*, vol. 28, no. 4, pp. 641–650, 2009.

[5] R. Soref and J. Lorenzo, “Single-crystal silicon: a new material for 1.3 and 1.6 μm integrated-optical components,” *Electronics Letters*, vol. 21, no. 21, pp. 953–954, 1985.

[6] G. T. Reed, G. Mashanovich, F. Y. Gardes, and D. Thomson, “Silicon optical modulators,” *Nature photonics*, vol. 4, no. 8, p. 518, 2010.

[7] F. Zhang, L. Zhang, X. Ruan, F. Yang, H. Ming, and Y. Li, “High baud rate transmission with silicon photonic modulators,” *IEEE Journal of Selected Topics in Quantum Electronics*, vol. 27, no. 3, pp. 1–9, 2021.

[8] A. Melikyan, N. Kaneda, K. Kim, Y. Baeyens, and P. Dong, “Differential drive i/q modulator based on silicon photonic electro-absorption modulators,” *Journal of Lightwave Technology*, vol. 38, no. 11, pp. 2872–2876, 2020.

[9] W. Cao, D. Hagan, D. J. Thomson, M. Nedeljkovic, C. G. Littlejohns, A. Knights, S.-U. Alam, J. Wang, F. Gardes, W. Zhang *et al.*, “High-speed silicon modulators for the 2 μm wavelength band,” *Optica*, vol. 5, no. 9, pp. 1055–1062, 2018.

[10] A. Melikyan, K. Kim, B. Stern, and N. Kaneda, “Self-biasing of carrier depletion based silicon microring modulators,” *Optics Express*, vol. 28, no. 15, pp. 22 540–22 548, 2020.

[11] Y. Hinakura, D. Akiyama, H. Ito, and T. Baba, “Silicon photonic crystal modulators for high-speed transmission and wavelength division multiplexing,” *IEEE Journal of Selected Topics in Quantum Electronics*, vol. 27, no. 3, pp. 1–8, 2020.

[12] M. M. P. Fard, C. Williams, G. Cowan, and O. Liboiron-Ladouceur, “High-speed grating-assisted all-silicon photodetectors for 850 nm applications,” *Optics express*, vol. 25, no. 5, pp. 5107–5118, 2017.

[13] J. Kim, S. S. Joo, K. W. Lee, J. H. Kim, D. H. Shin, S. Kim, and S.-H. Choi, "Near-ultraviolet-sensitive graphene/porous silicon photodetectors," *ACS applied materials & interfaces*, vol. 6, no. 23, pp. 20 880–20 886, 2014.

[14] M. Casalino, "Design of resonant cavity-enhanced schottky graphene/silicon photodetectors at 1550 nm," *Journal of Lightwave Technology*, vol. 36, no. 9, pp. 1766–1774, 2018.

[15] X. Jin, Q. Wu, S. Huang, G. Deng, J. Yao, H. Huang, P. Zhao, and J. Xu, "High-performance black silicon photodetectors operating over a wide temperature range," *Optical Materials*, vol. 113, p. 110874, 2021.

[16] I.-S. Chung and J. Mørk, "Silicon-photonics light source realized by iii–v/si-grating-mirror laser," *Applied Physics Letters*, vol. 97, no. 15, p. 151113, 2010.

[17] I. J. Luxmoore, R. Toro, O. Del Pozo-Zamudio, N. A. Wasley, E. A. Chekhovich, A. M. Sanchez, R. Beanland, A. M. Fox, M. S. Skolnick, H. Y. Liu *et al.*, "Iii–v quantum light source and cavity-qed on silicon," *Scientific reports*, vol. 3, no. 1, pp. 1–5, 2013.

[18] N. Hatori, T. Shimizu, M. Okano, M. Ishizaka, T. Yamamoto, Y. Urino, M. Mori, T. Nakamura, and Y. Arakawa, "A hybrid integrated light source on a silicon platform using a trident spot-size converter," *Journal of Lightwave Technology*, vol. 32, no. 7, pp. 1329–1336, 2014.

[19] M. A. Green, J. Zhao, A. Wang, P. J. Reece, and M. Gal, "Efficient silicon light-emitting diodes," *Nature*, vol. 412, no. 6849, pp. 805–808, 2001.

[20] Z. Wang, A. Abbasi, U. Dave, A. De Groote, S. Kumari, B. Kunert, C. Merckling, M. Pantouvaki, Y. Shi, B. Tian *et al.*, "Novel light source integration approaches for silicon photonics," *Laser & Photonics Reviews*, vol. 11, no. 4, p. 1700063, 2017.

[21] N. Volet, A. Spott, E. J. Stanton, M. L. Davenport, L. Chang, J. D. Peters, T. C. Briles, I. Vurgaftman, J. R. Meyer, and J. E. Bowers, "Semiconductor optical amplifiers at 2.0-μm wavelength on silicon," *Laser & Photonics Reviews*, vol. 11, no. 2, p. 1600165, 2017.

[22] P. Xing, G. Chen, X. Zhao, D. Ng, M. Tan, and D. Tan, "Silicon rich nitride ring resonators for rare–earth doped telecommunications-band amplifiers pumped at the o-band," *Scientific reports*, vol. 7, no. 1, pp. 1–9, 2017.

[23] B. Haq, S. Kumari, K. Van Gasse, J. Zhang, A. Gocalinska, E. Pelucchi, B. Corbett, and G. Roelkens, "Micro-transfer-printed iii-v-on-silicon c-band semiconductor optical amplifiers," *Laser & Photonics Reviews*, vol. 14, no. 7, p. 1900364, 2020.

[24] S. Liu, J. Norman, M. Dumont, D. Jung, A. Torres, A. C. Gossard, J. E. Bowers, S. Liu, A. Torres, A. Gossard *et al.*, "High-performance o-band quantum-dot semiconductor optical amplifiers directly grown on a cmos compatible silicon substrate," *ACS Photonics*, vol. 6, no. 10, pp. 2523–2529, 2019.

[25] S. Arshavsky-Graham, N. Massad-Ivanir, E. Segal, and S. Weiss, "Porous silicon-based photonic biosensors: Current status and emerging applications," *Analytical chemistry*, vol. 91, no. 1, pp. 441–467, 2018.

[26] S. Sahu, J. Ali, P. P. Yupapin, and G. Singh, "Porous silicon based bragg-grating resonator for refractive index biosensor," *Photonic Sensors*, vol. 8, no. 3, pp. 248–254, 2018.

[27] H. Yan, C.-J. Yang, N. Tang, Y. Zou, S. Chakravarty, A. Roth, and R. T. Chen, "Specific detection of antibiotics by silicon-on-chip photonic crystal biosensor arrays," *IEEE Sensors Journal*, vol. 17, no. 18, pp. 5915–5919, 2017.

[28] P. Steglich, M. Hülsemann, B. Dietzel, and A. Mai, "Optical biosensors based on silicon-on-insulator ring resonators: A review," *Molecules*, vol. 24, no. 3, p. 519, 2019.

[29] G. A. Rodriguez, P. Markov, A. P. Cartwright, M. H. Choudhury, F. O. Afzal, T. Cao, S. I. Halimi, S. T. Retterer, I. I. Kravchenko, and S. M. Weiss, "Photonic crystal nanobeam biosensors based on porous silicon," *Optics express*, vol. 27, no. 7, pp. 9536–9549, 2019.

[30] Z. Cheng, J. Zhang, J. Dong, and Y. Ding, "Compact high-contrast silicon optical filter using all-passive and crow fano nanobeam resonators," *Optics Letters*, vol. 46, no. 16, pp. 3873–3876, 2021.

[31] J. Wan, J. Miao, J. You, L. Xu, and X. Xie, "Silicon optical filter with multiple semi-rings," *Applied Optics*, vol. 59, no. 22, pp. 6551–6556, 2020.

[32] D. Liu and D. Dai, "Silicon-based polarization-insensitive optical filter with dual-gratings," *Optics express*, vol. 27, no. 15, pp. 20 704–20 710, 2019.

[33] D. Liu, H. Wu, and D. Dai, "Silicon multimode waveguide grating filter at 2 μm," *Journal of Lightwave Technology*, vol. 37, no. 10, pp. 2217–2222, 2019.

[34] J. Feng, R. Akimoto, Q. Hao, and H. Zeng, "Three-dimensional cross-coupled silicon nitride race-track resonator-based tunable optical filter," *IEEE Photonics Technology Letters*, vol. 29, no. 9, pp. 771–774, 2017.

[35] Y. He, Y. Zhang, Q. Zhu, S. An, R. Cao, X. Guo, C. Qiu, and Y. Su, "Silicon high-order mode (de) multiplexer on single polarization," *Journal of Lightwave Technology*, vol. 36, no. 24, pp. 5746–5753, 2018.

[36] D. Dai, J. Wang, and Y. Shi, "Silicon mode (de) multiplexer enabling high capacity photonic networks-on-chip with a single-wavelength-carrier light," *Optics letters*, vol. 38, no. 9, pp. 1422–1424, 2013.

[37] Y. He, Y. Zhang, H. Wang, L. Sun, and Y. Su, "Design and experimental demonstration of a silicon multi-dimensional (de) multiplexer for wavelength-, mode-and polarization-division (de) multiplexing," *Optics letters*, vol. 45, no. 10, pp. 2846–2849, 2020.

[38] W. Jiang, J. Hu, S. Mao, H. Zhang, L. Zhou, and B. A. Rahman, "Broadband silicon four-mode (de) multiplexer using subwavelength grating-assisted triple-waveguide couplers," *Journal of Lightwave Technology*, vol. 39, no. 15, pp. 5042–5047, 2021.

[39] L. Chrostowski and M. Hochberg, *Silicon photonics design: from devices to systems*. Cambridge University Press, 2015.

[40] M. Dinu, F. Quochi, and H. Garcia, "Third-order nonlinearities in silicon at telecom wavelengths," *Applied physics letters*, vol. 82, no. 18, pp. 2954–2956, 2003.

[41] R. Claps, D. Dimitropoulos, V. Raghunathan, Y. Han, and B. Jalali, "Observation of stimulated raman amplification in silicon waveguides," *Optics express*, vol. 11, no. 15, pp. 1731–1739, 2003.

[42] B. Jalali and S. Fathpour, "Silicon photonics," *Journal of lightwave technology*, vol. 24, no. 12, pp. 4600–4615, 2006.

[43] H. H. Goldstine and A. Goldstine, "The electronic numerical integrator and computer (eniac)," *IEEE Annals of the History of Computing*, vol. 18, no. 1, pp. 10–16, 1996.

[44] J. M. Rabaey, A. P. Chandrakasan, and B. Nikolic, *Digital integrated circuits.* Prentice hall Englewood Cliffs, 2002, vol. 2.

[45] A. Rose, "Lightning strikes mathematics," *Popular Science*, pp. 83–86, 1946.

[46] W. Aspray, "The intel 4004 microprocessor: what constituted invention?" *IEEE Annals of the History of Computing*, vol. 19, no. 3, pp. 4–15, 1997.

[47] R. R. Schaller, "Moore's law: past, present and future," *IEEE spectrum*, vol. 34, no. 6, pp. 52–59, 1997.

[48] B. Dhoedt, R. Baets, P. Van Daele, P. Heremans, J. Van Campenhout, J. Hall, R. Michalzik, A. Schmid, H. Thienpont, R. Vounckx *et al.*, "Optically interconnected integrated circuits to solve the cmos interconnect bottleneck," in *Electronic Components & Technology Conference, 1998. 48th IEEE.* IEEE, 1998, pp. 992–998.

[49] P. Gepner and M. F. Kowalik, "Multi-core processors: New way to achieve high system performance," in *Parallel Computing in Electrical Engineering, 2006. PAR ELEC 2006. International Symposium on.* IEEE, 2006, pp. 9–13.

[50] J. Ahn, M. Fiorentino, R. G. Beausoleil, N. Binkert, A. Davis, D. Fattal, N. P. Jouppi, M. McLaren, C. M. Santori, R. S. Schreiber *et al.*, "Devices and architectures for photonic chip-scale integration," *Applied Physics A*, vol. 95, no. 4, pp. 989–997, 2009.

[51] C. Zhang, S. Zhang, J. D. Peters, and J. E. Bowers, "8× 8× 40 gbps fully integrated silicon photonic network on chip," *Optica*, vol. 3, no. 7, pp. 785–786, 2016.

[52] D. Dai and J. E. Bowers, "Silicon-based on-chip multiplexing technologies and devices for petabit optical interconnects," *Nanophotonics*, vol. 3, no. 4-5, pp. 283–311, 2014.

[53] H. Cho, P. Kapur, and K. C. Saraswat, "Power comparison between high-speed electrical and optical interconnects for interchip communication," *Journal of Lightwave Technology*, vol. 22, no. 9, p. 2021, 2004.

[54] C. Williams, B. Banan, G. Cowan, and O. Liboiron-Ladouceur, "A source-synchronous architecture using mode-division multiplexing for on-chip silicon photonic interconnects," *IEEE Journal of Selected Topics in Quantum Electronics*, vol. 22, no. 6, pp. 473–481, 2016.

[55] S. Martínez-Garaot, S.-Y. Tseng, and J. Muga, "Compact and high conversion efficiency mode-sorting asymmetric y junction using shortcuts to adiabaticity," *Optics letters*, vol. 39, no. 8, pp. 2306–2309, 2014.

[56] L. F. Frellsen, Y. Ding, O. Sigmund, and L. H. Frandsen, "Topology optimized mode multiplexing in silicon-on-insulator photonic wire waveguides," *Optics express*, vol. 24, no. 15, pp. 16 866–16 873, 2016.

[57] S.-Y. Tseng, R.-D. Wen, Y.-F. Chiu, and X. Chen, "Short and robust directional couplers designed by shortcuts to adiabaticity," *Optics express*, vol. 22, no. 16, pp. 18 849–18 859, 2014.

[58] H. Fukuda, K. Yamada, T. Tsuchizawa, T. Watanabe, H. Shinojima, and S.-i. Itabashi, "Silicon photonic circuit with polarization diversity," *Optics express*, vol. 16, no. 7, pp. 4872–4880, 2008.

[59] T. Barwicz, M. R. Watts, M. A. Popović, P. T. Rakich, L. Socci, F. X. Kärtner, E. P. Ippen, and H. I. Smith, “Polarization-transparent microphotonic devices in the strong confinement limit,” *Nature Photonics*, vol. 1, no. 1, pp. 57–60, 2007.

[60] R. Ding, Y. Liu, Q. Li, Z. Xuan, Y. Ma, Y. Yang, A. E.-J. Lim, G.-Q. Lo, K. Bergman, T. Baehr-Jones *et al.*, “A compact low-power 320-gb/s wdm transmitter based on silicon microrings,” *IEEE Photonics Journal*, vol. 6, no. 3, pp. 1–8, 2014.

[61] Q. Fang, T.-Y. Liow, J. F. Song, K. W. Ang, M. B. Yu, G. Q. Lo, and D.-L. Kwong, “Wdm multi-channel silicon photonic receiver with 320 gbps data transmission capability,” *Optics express*, vol. 18, no. 5, pp. 5106–5113, 2010.

[62] X. Fu and D. Dai, “Ultra-small si-nanowire-based 400 ghz-spacing 15 x 15 arrayed-waveguide grating router with microbends,” *Electronics letters*, vol. 47, no. 4, pp. 266–268, 2011.

[63] W. Bogaerts, P. Dumon, D. Van Thourhout, D. Taillaert, P. Jaenen, J. Wouters, S. Beckx, V. Wiaux, and R. G. Baets, “Compact wavelength-selective functions in silicon-on-insulator photonic wires,” *IEEE Journal of Selected Topics in Quantum Electronics*, vol. 12, no. 6, pp. 1394–1401, 2006.

[64] K. Okamoto, “Wavelength-division-multiplexing devices in thin soi: Advances and prospects,” *IEEE Journal of Selected Topics in Quantum Electronics*, vol. 20, no. 4, pp. 248–257, 2013.

[65] P. Dong, “Silicon photonic integrated circuits for wavelength-division multiplexing applications,” *IEEE Journal of Selected Topics in Quantum Electronics*, vol. 22, no. 6, pp. 370–378, 2016.

[66] A. Liu, L. Liao, Y. Chetrit, J. Basak, H. Nguyen, D. Rubin, and M. Paniccia, “Wavelength division multiplexing based photonic integrated circuits on silicon-on-insulator platform,” *IEEE Journal of Selected Topics in Quantum Electronics*, vol. 16, no. 1, pp. 23–32, 2009.

[67] L.-W. Luo, N. Ophir, C. P. Chen, L. H. Gabrielli, C. B. Poitras, K. Bergmen, and M. Lipson, “Wdm-compatible mode-division multiplexing on a silicon chip,” *Nature communications*, vol. 5, no. 1, p. 3069, 2014.

[68] J. B. Driscoll, C. P. Chen, R. R. Grote, B. Souhan, J. I. Dadap, A. Stein, M. Lu, K. Bergman, and R. M. Osgood, “A 60 gb/s mdm-wdm si photonic link with< 0.7 db power penalty per channel,” *Optics express*, vol. 22, no. 15, pp. 18 543–18 555, 2014.

[69] A. Yariv and P. Yeh, “Photonics-optical electronics in modern communications,” 2007.

[70] X. Wang, Y. Zhao, Y. Ding, S. Xiao, and J. Dong, “Tunable optical delay line based on integrated grating-assisted contradirectional couplers,” *Photonics Research*, vol. 6, no. 9, pp. 880–886, 2018.

[71] H. Qiu, J. Jiang, P. Yu, D. Mu, J. Yang, X. Jiang, H. Yu, R. Cheng, and L. Chrostowski, “Narrow-band add-drop filter based on phase-modulated grating-assisted contra-directional couplers,” *Journal of Lightwave Technology*, vol. 36, no. 17, pp. 3760–3764, 2018.

[72] X. Nie, N. Turk, Y. Li, Z. Liu, and R. Baets, “High extinction ratio on-chip pump-rejection filter based on cascaded grating-assisted contra-directional couplers in silicon nitride rib waveguides,” *Optics letters*, vol. 44, no. 9, pp. 2310–2313, 2019.

[73] J. A. Davis, A. Grieco, M. C. Souza, N. C. Frateschi, and Y. Fainman, “Hybrid multimode resonators based on grating-assisted counter-directional couplers,” *Optics express*, vol. 25, no. 14, pp. 16 484–16 490, 2017.

[74] R. Halir, A. Ortega-Monux, J. H. Schmid, C. Alonso-Ramos, J. Lapointe, D.-X. Xu, J. G. Wangüemert-Pérez, I. Molina-Fernandez, and S. Janz, "Recent advances in silicon waveguide devices using sub-wavelength gratings," *IEEE Journal of Selected Topics in Quantum Electronics*, vol. 20, no. 4, pp. 279–291, 2013.

[75] S. Rytov, "Electromagnetic properties of a finely stratified medium," *Soviet Physics JEPT*, vol. 2, pp. 466–475, 1956.

[76] Z. Jafari, A. Zarifkar, and M. Miri, "Compact fabrication-tolerant subwavelength-grating-based two-mode division (de) multiplexer," *Applied optics*, vol. 56, no. 26, pp. 7311–7319, 2017.

[77] S. Wu, S. Mao, L. Zhou, L. Liu, Y. Chen, X. Mu, L. Cheng, Z. Chen, X. Tu, and H. Fu, "A compact and polarization-insensitive silicon waveguide crossing based on subwavelength grating mmi couplers," *Optics Express*, vol. 28, no. 19, pp. 27 268–27 276, 2020.

[78] R. Halir, P. Cheben, J. Schmid, R. Ma, D. Bedard, S. Janz, D.-X. Xu, A. Densmore, J. Lapointe, and I. Molina-Fernández, "Continuously apodized fiber-to-chip surface grating coupler with refractive index engineered subwavelength structure," *Optics Letters*, vol. 35, no. 19, pp. 3243–3245, 2010.

[79] Y. Xiong, J. G. Wangüemert-Pérez, D.-X. Xu, J. H. Schmid, P. Cheben, and N. Y. Winnie, "Polarization splitter and rotator with subwavelength grating for enhanced fabrication tolerance," *Optics Letters*, vol. 39, no. 24, pp. 6931–6934, 2014.

[80] A. Ortega-Moñux, C. Alonso-Ramos, A. Maese-Novo, R. Halir, L. Zavargo-Peche, D. Pérez-Galacho, I. Molina-Fernández, J. G. Wangüemert-Pérez, P. Cheben, J. H. Schmid *et al.*, "An ultra-compact multimode interference coupler with a subwavelength grating slot," *Laser & Photonics Reviews*, vol. 7, no. 2, pp. L12–L15, 2013.

[81] J. Wang, I. Glesk, and L. R. Chen, "Subwavelength grating filtering devices," *Optics Express*, vol. 22, no. 13, pp. 15 335–15 345, 2014.

[82] H. Xie, J. Zheng, P. Xu, J. Yao, J. Whitehead, and A. Majumdar, "Ultra-compact subwavelength-grating-assisted polarization-independent directional coupler," *IEEE Photonics Technology Letters*, vol. 31, no. 18, pp. 1538–1541, 2019.

[83] J. Wang, S. Chen, and D. Dai, "Silicon hybrid demultiplexer with 64 channels for wavelength/mode-division multiplexed on-chip optical interconnects," *Optics letters*, vol. 39, no. 24, pp. 6993–6996, 2014.

[84] S. Pathak, P. Dumon, D. Van Thourhout, and W. Bogaerts, "Comparison of awgs and echelle gratings for wavelength division multiplexing on silicon-on-insulator," *IEEE Photonics Journal*, vol. 6, no. 5, pp. 1–9, 2014.

[85] S. Pathak, M. Vanslembrouck, P. Dumon, D. Van Thourhout, P. Verheyen, G. Lepage, P. Absil, and W. Bogaerts, "Effect of mask discretization on performance of silicon arrayed waveguide gratings," *IEEE Photonics Technology Letters*, vol. 26, no. 7, pp. 718–721, 2014.

[86] S. Pathak, D. Van Thourhout, and W. Bogaerts, "Design trade-offs for silicon-on-insulator-based awgs for (de) multiplexer applications," *Optics letters*, vol. 38, no. 16, pp. 2961–2964, 2013.

[87] W. Bogaerts, D. Taillaert, P. Dumon, D. Van Thourhout, R. Baets, and E. Pluk, "A polarization-diversity wavelength duplexer circuit in silicon-on-insulator photonic wires," *Optics express*, vol. 15, no. 4, pp. 1567–1578, 2007.

[88] P. Chen, S. Chen, X. Guan, Y. Shi, and D. Dai, “High-order microring resonators with bent couplers for a box-like filter response,” *optics letters*, vol. 39, no. 21, pp. 6304–6307, 2014.

[89] F. Xia, M. Rooks, L. Sekaric, and Y. Vlasov, “Ultra-compact high order ring resonator filters using submicron silicon photonic wires for on-chip optical interconnects,” *Optics express*, vol. 15, no. 19, pp. 11 934–11 941, 2007.

[90] Y. Tan, S. Chen, and D. Dai, “Polarization-selective microring resonators,” *Optics Express*, vol. 25, no. 4, pp. 4106–4119, 2017.

[91] X. Luo, J. Song, S. Feng, A. W. Poon, T.-Y. Liow, M. Yu, G.-Q. Lo, and D.-L. Kwong, “Silicon high-order coupled-microring-based electro-optical switches for on-chip optical interconnects,” *IEEE Photonics Technology Letters*, vol. 24, no. 10, pp. 821–823, 2012.

[92] M. S. Dahlem, C. W. Holzwarth, A. Khilo, F. X. Kärtner, H. I. Smith, and E. P. Ippen, “Reconfigurable multi-channel second-order silicon microring-resonator filterbanks for on-chip wdm systems,” *Optics express*, vol. 19, no. 1, pp. 306–316, 2011.

[93] L. Y. M. Tobing, P. Dumon, R. Baets, and M.-K. Chin, “Boxlike filter response based on complementary photonic bandgaps in two-dimensional microresonator arrays,” *Optics letters*, vol. 33, no. 21, pp. 2512–2514, 2008.

[94] R. Grover, V. Van, T. Ibrahim, P. Absil, L. Calhoun, F. Johnson, J. Hryniewicz, and P.-T. Ho, “Parallel-cascaded semiconductor microring resonators for high-order and wide-fsr filters,” *Journal of Lightwave Technology*, vol. 20, no. 5, p. 872, 2002.

[95] B. E. Little, S. T. Chu, J. V. Hryniewicz, and P. P. Absil, “Filter synthesis for periodically coupled microring resonators,” *Optics Letters*, vol. 25, no. 5, pp. 344–346, 2000.

[96] P. Dong, N.-N. Feng, D. Feng, W. Qian, H. Liang, D. C. Lee, B. Luff, T. Banwell, A. Agarwal, P. Toliver *et al.*, “Ghz-bandwidth optical filters based on high-order silicon ring resonators,” *Optics express*, vol. 18, no. 23, pp. 23 784–23 789, 2010.

[97] P. Dong, W. Qian, H. Liang, R. Shafiiha, N.-N. Feng, D. Feng, X. Zheng, A. V. Krishnamoorthy, and M. Asghari, “Low power and compact reconfigurable multiplexing devices based on silicon microring resonators,” *Optics express*, vol. 18, no. 10, pp. 9852–9858, 2010.

[98] W. Bogaerts, P. De Heyn, T. Van Vaerenbergh, K. De Vos, S. Kumar Selvaraja, T. Claes, P. Dumon, P. Bienstman, D. Van Thourhout, and R. Baets, “Silicon microring resonators,” *Laser & Photonics Reviews*, vol. 6, no. 1, pp. 47–73, 2012.

[99] L. Vivien and L. Pavesi, *Handbook of silicon photonics*. Taylor & Francis, 2016.

[100] S. Chen, Y. Shi, S. He, and D. Dai, “Compact monolithically-integrated hybrid (de) multiplexer based on silicon-on-insulator nanowires for pdm-wdm systems,” *Optics Express*, vol. 23, no. 10, pp. 12 840–12 849, 2015.

[101] D. Dai, J. Wang, and Y. Shi, “Silicon mode (de) multiplexer enabling high capacity photonic networks-on-chip with a single-wavelength-carrier light,” *Optics letters*, vol. 38, no. 9, pp. 1422–1424, 2013.

[102] M. Greenberg and M. Orenstein, “Multimode add-drop multiplexing by adiabatic linearly tapered coupling,” *Optics express*, vol. 13, no. 23, pp. 9381–9387, 2005.

[103] D. Dai and J. Wang, “Multi-channel silicon mode (de) multiplexer based on asymmetrical directional couplers for on-chip optical interconnects,” *IEEE Photon. Soc. News*, vol. 28, no. 2, pp. 8–14, 2014.

[104] D. Dai and S. Wang, “Asymmetric directional couplers based on silicon nanophotonic waveguides and applications,” *Frontiers of Optoelectronics*, vol. 9, no. 3, pp. 450–465, 2016.

[105] J. Love, R. Vance, and A. Joblin, “Asymmetric, adiabatic multipronged planar splitters,” *Optical and quantum electronics*, vol. 28, no. 4, pp. 353–369, 1996.

[106] H. Li, P. Wang, T. Yang, T. Dai, G. Wang, S. Li, W. Chen, and J. Yang, “Experimental demonstration of a broadband two-mode multi/demultiplexer based on asymmetric y-junctions,” *Optics & Laser Technology*, vol. 100, pp. 7–11, 2018.

[107] W. Chen, P. Wang, and J. Yang, “Mode multi/demultiplexer based on cascaded asymmetric y-junctions,” *Optics express*, vol. 21, no. 21, pp. 25 113–25 119, 2013.

[108] N. Riesen and J. D. Love, “Design of mode-sorting asymmetric y-junctions,” *Applied optics*, vol. 51, no. 15, pp. 2778–2783, 2012.

[109] J. B. Driscoll, R. R. Grote, B. Souhan, J. I. Dadap, M. Lu, and R. M. Osgood, “Asymmetric Y junctions in silicon waveguides for on-chip mode-division multiplexing,” *Optics Letters*, vol. 38, no. 11, pp. 1854–1856, 2013.

[110] D. González-Andrade, J. G. Wangüemert-Pérez, A. V. Velasco, A. Ortega-Moñux, A. Herrero-Bermello, I. Molina-Fernández, R. Halir, and P. Cheben, “Ultra-broadband mode converter and multiplexer based on sub-wavelength structures,” *IEEE Photonics Journal*, vol. 10, no. 2, pp. 1–10, 2018.

[111] L. Han, S. Liang, H. Zhu, L. Qiao, J. Xu, and W. Wang, “Two-mode de/multiplexer based on multimode interference couplers with a tilted joint as phase shifter,” *Optics letters*, vol. 40, no. 4, pp. 518–521, 2015.

[112] Y. Li, C. Li, C. Li, B. Cheng, and C. Xue, “Compact two-mode (de) multiplexer based on symmetric y-junction and multimode interference waveguides,” *Optics express*, vol. 22, no. 5, pp. 5781–5786, 2014.

[113] T. Uematsu, Y. Ishizaka, Y. Kawaguchi, K. Saitoh, and M. Koshiba, “Design of a compact two-mode multi/demultiplexer consisting of multimode interference waveguides and a wavelength-insensitive phase shifter for mode-division multiplexing transmission,” *Journal of Lightwave Technology*, vol. 30, no. 15, pp. 2421–2426, 2012.

[114] Y. Kawaguchi and K. Tsutsumi, “Mode multiplexing and demultiplexing devices using multimode interference couplers,” *Electronics Letters*, vol. 38, no. 25, pp. 1701–1702, 2002.

[115] Y. Ding, J. Xu, F. Da Ros, B. Huang, H. Ou, and C. Peucheret, “On-chip two-mode division multiplexing using tapered directional coupler-based mode multiplexer and demultiplexer,” *Optics express*, vol. 21, no. 8, pp. 10 376–10 382, 2013.

[116] D. Guo and T. Chu, “Silicon mode (de) multiplexers with parameters optimized using shortcuts to adiabaticity,” *Optics express*, vol. 25, no. 8, pp. 9160–9170, 2017.

[117] C.-P. Ho and S.-Y. Tseng, “Optimization of adiabaticity in coupled-waveguide devices using shortcuts to adiabaticity,” *Optics letters*, vol. 40, no. 21, pp. 4831–4834, 2015.

[118] T.-H. Pan and S.-Y. Tseng, “Short and robust silicon mode (de) multiplexers using shortcuts to adiabaticity,” *Optics express*, vol. 23, no. 8, pp. 10 405–10 412, 2015.

[119] C. Li and D. Dai, “Low-loss and low-crosstalk multi-channel mode (de) multiplexer with ultrathin silicon waveguides,” *Optics letters*, vol. 42, no. 12, pp. 2370–2373, 2017.

[120] C. Sun, Y. Yu, G. Chen, and X. Zhang, “Silicon mode multiplexer processing dual-path mode-division multiplexing signals,” *Optics letters*, vol. 41, no. 23, pp. 5511–5514, 2016.

[121] J. Xing, Z. Li, X. Xiao, J. Yu, and Y. Yu, “Two-mode multiplexer and demultiplexer based on adiabatic couplers,” *Optics letters*, vol. 38, no. 17, pp. 3468–3470, 2013.

[122] J. Wang, Y. Xuan, M. Qi, H. Huang, Y. Li, M. Li, X. Chen, Z. Sheng, A. Wu, W. Li *et al.*, “Broadband and fabrication-tolerant on-chip scalable mode-division multiplexing based on mode-evolution counter-tapered couplers,” *Optics letters*, vol. 40, no. 9, pp. 1956–1959, 2015.

[123] Z. Zhang, Y. Yu, and S. Fu, “Broadband on-chip mode-division multiplexer based on adiabatic couplers and symmetric y-junction,” *IEEE Photonics Journal*, vol. 9, no. 2, pp. 1–6, 2017.

[124] Z. Jafari, A. Zarifkar, and M. Miri, “Compact fabrication-tolerant subwavelength-grating-based two-mode division (de) multiplexer,” *Applied Optics*, vol. 56, no. 26, pp. 7311–7319, 2017.

[125] H. Xu and Y. Shi, “Ultra-broadband 16-channel mode division (de) multiplexer utilizing densely packed bent waveguide arrays,” *Optics letters*, vol. 41, no. 20, pp. 4815–4818, 2016.

[126] M. Yin, Q. Deng, Y. Li, X. Wang, and H. Li, “Compact and broadband mode multiplexer and demultiplexer based on asymmetric plasmonic–dielectric coupling,” *Applied optics*, vol. 53, no. 27, pp. 6175–6180, 2014.

[127] D. Chack, S. Hassan, and M. Qasim, “Broadband and low crosstalk silicon on-chip mode converter and demultiplexer for mode division multiplexing,” *Applied optics*, vol. 59, no. 12, pp. 3652–3659, 2020.

[128] J. P. Nath, N. Dhingra, G. J. Saxena, and E. K. Sharma, “Compact mode division (de) multiplexer based on collaterally coupled soi waveguides,” *IEEE Photonics Technology Letters*, vol. 32, no. 10, pp. 595–598, 2020.

[129] Y. Jiao, D. Dai, Y. Shi, and S. He, “Shortened polarization beam splitters with two cascaded multimode interference sections,” *IEEE Photonics Technology Letters*, vol. 21, no. 20, pp. 1538–1540, 2009.

[130] I. Kiyat, A. Aydinli, and N. Dagli, “A compact silicon-on-insulator polarization splitter,” *IEEE photonics technology letters*, vol. 17, no. 1, pp. 100–102, 2005.

[131] L. Augustin, R. Hanfoug, J. Van der Tol, W. De Laat, and M. Smit, “A compact integrated polarization splitter/converter in ingaasp–inp,” *IEEE Photonics Technology Letters*, vol. 19, no. 17, pp. 1286–1288, 2007.

[132] D. Dai, “Silicon polarization beam splitter based on an asymmetrical evanescent coupling system with three optical waveguides,” *Journal of Lightwave Technology*, vol. 30, no. 20, pp. 3281–3287, 2012.

[133] Y. Qin, Y. Yu, M. Ye, J. Zou, G. Chen, and X. Zhang, “High-order mode polarization rotator for all optical sdm-pdm signals processing,” in *2014 Asia Communications and Photonics Conference (ACP)*. IEEE, 2014, pp. 1–3.

[134] J. Wang, D. Zhao, J. Xu, X. Xue, and X. Zhang, "High-order mode rotator on the soi integrated platform," *IEEE Photonics Journal*, vol. 8, no. 2, pp. 1–8, 2016.

[135] K. Chen, S. Wang, S. Chen, S. Wang, C. Zhang, D. Dai, and L. Liu, "Experimental demonstration of simultaneous mode and polarization-division multiplexing based on silicon densely packed waveguide array," *Optics Letters*, vol. 40, no. 20, pp. 4655–4658, 2015.

[136] C. P. Chen, J. B. Driscoll, R. R. Grote, B. Souhan, R. M. Osgood, and K. Bergman, "Mode and polarization multiplexing in a si photonic chip at 40gb/s aggregate data bandwidth," *IEEE Photonics Technology Letters*, vol. 27, no. 1, pp. 22–25, 2015.

[137] J. Wang, S. He, and D. Dai, "On-chip silicon 8-channel hybrid (de) multiplexer enabling simultaneous mode-and polarization-division-multiplexing," *Laser & Photonics Reviews*, vol. 8, no. 2, pp. L18–L22, 2014.

[138] S. Pathak, M. Vanslembrouck, P. Dumon, D. Van Thourhout, and W. Bogaerts, "Compact soi-based polarization diversity wavelength de-multiplexer circuit using two symmetric awgs," *Optics Express*, vol. 20, no. 26, pp. B493–B500, 2012.

[139] D. Melati, A. Alippi, A. Annoni, N. Peserico, and A. Melloni, "Integrated all-optical mimo demultiplexer for mode-and wavelength-division-multiplexed transmission," *Optics letters*, vol. 42, no. 2, pp. 342–345, 2017.

[140] H. Jia, L. Zhang, J. Ding, L. Zheng, C. Yuan, and L. Yang, "Microring modulator matrix integrated with mode multiplexer and de-multiplexer for on-chip optical interconnect," *Optics express*, vol. 25, no. 1, pp. 422–430, 2017.

[141] D. Dai, J. Wang, S. Chen, S. Wang, and S. He, "Monolithically integrated 64-channel silicon hybrid demultiplexer enabling simultaneous wavelength-and mode-division-multiplexing," *Laser & Photonics Reviews*, vol. 9, no. 3, pp. 339–344, 2015.

[142] J. B. Driscoll, C. P. Chen, R. R. Grote, B. Souhan, J. I. Dadap, A. Stein, M. Lu, K. Bergman, and R. M. Osgood, "A 60 gb/s mdm-wdm si photonic link with< 0.7 db power penalty per channel," *Optics express*, vol. 22, no. 15, pp. 18 543–18 555, 2014.

[143] T. Mulugeta and M. Rasras, "Silicon hybrid (de) multiplexer enabling simultaneous mode and wavelength-division multiplexing," *Optics express*, vol. 23, no. 2, pp. 943–949, 2015.

[144] Y.-D. Yang, Y. Li, Y.-Z. Huang, and A. W. Poon, "Silicon nitride three-mode division multiplexing and wavelength-division multiplexing using asymmetrical directional couplers and microring resonators," *Optics express*, vol. 22, no. 18, pp. 22 172–22 183, 2014.

[145] Z. Zhang, Y. Yu, and S. Fu, "Broadband on-chip mode-division multiplexer based on adiabatic couplers and symmetric y-junction," *IEEE Photonics J*, vol. 9, no. 2, pp. 1–6, 2017.

[146] H. Li, P. Wang, T. Yang, T. Dai, G. Wang, S. Li, W. Chen, and J. Yang, "Experimental demonstration of a broadband two-mode multi/demultiplexer based on asymmetric y-junctions," *Optics & Laser Technology*, vol. 100, pp. 7–11, 2018.

[147] X. Wu, C. Huang, K. Xu, C. Shu, and H. K. Tsang, "Mode-division multiplexing for silicon photonic network-on-chip," *Journal of Lightwave Technology*, vol. 35, no. 15, pp. 3223–3228, 2017.

[148] H. Xu and Y. Shi, "Ultra-broadband 16-channel mode division (de) multiplexer utilizing densely packed bent waveguide arrays," *Optics letters*, vol. 41, no. 20, pp. 4815–4818, 2016.

[149] H. Qiu, H. Yu, T. Hu, G. Jiang, H. Shao, P. Yu, J. Yang, and X. Jiang, "Silicon mode multi/demultiplexer based on multimode grating-assisted couplers," *Optics express*, vol. 21, no. 15, pp. 17 904–17 911, 2013.

[150] S. G. Cloutier, P. A. Kossyrev, and J. Xu, "Optical gain and stimulated emission in periodic nanopatterned crystalline silicon," *Nature materials*, vol. 4, no. 12, pp. 887–891, 2005.

[151] L. Pavesi, L. Dal Negro, C. Mazzoleni, G. Franzo, and d. F. Priolo, "Optical gain in silicon nanocrystals," *Nature*, vol. 408, no. 6811, pp. 440–444, 2000.

[152] H. Rong, A. Liu, R. Jones, O. Cohen, D. Hak, R. Nicolaescu, A. Fang, and M. Paniccia, "An all-silicon raman laser," *Nature*, vol. 433, no. 7023, pp. 292–294, 2005.

[153] H. Rong, S. Xu, Y.-H. Kuo, V. Sih, O. Cohen, O. Raday, and M. Paniccia, "Low-threshold continuous-wave raman silicon laser," *Nature Photonics*, vol. 1, no. 4, pp. 232–237, 2007.

[154] M. Pralle, N. Moelders, M. McNeal, I. Puscasu, A. Greenwald, J. Daly, E. Johnson, T. George, D. Choi, I. El-Kady *et al.*, "Photonic crystal enhanced narrow-band infrared emitters," *Applied Physics Letters*, vol. 81, no. 25, pp. 4685–4687, 2002.

[155] R. Soref, "Toward silicon-based longwave integrated optoelectronics (lio)," in *Silicon Photonics III*, vol. 6898. SPIE, 2008, pp. 80–92.

[156] A. Y. Liu, C. Zhang, J. Norman, A. Snyder, D. Lubyshev, J. M. Fastenau, A. W. Liu, A. C. Gossard, and J. E. Bowers, "High performance continuous wave 1.3 μ m quantum dot lasers on silicon," *Applied Physics Letters*, vol. 104, no. 4, p. 041104, 2014.

[157] D. Jung, Z. Zhang, J. Norman, R. Herrick, M. Kennedy, P. Patel, K. Turnlund, C. Jan, Y. Wan, A. C. Gossard *et al.*, "Highly reliable low-threshold inas quantum dot lasers on on-axis (001) si with 87% injection efficiency," *ACS photonics*, vol. 5, no. 3, pp. 1094–1100, 2017.

[158] S. Chen, W. Li, J. Wu, Q. Jiang, M. Tang, S. Shutts, S. N. Elliott, A. Sobiesierski, A. J. Seeds, I. Ross *et al.*, "Electrically pumped continuous-wave iii–v quantum dot lasers on silicon," *Nature Photonics*, vol. 10, no. 5, pp. 307–311, 2016.

[159] J. E. Bowers, T. Komljenovic, M. Davenport, J. Hulme, A. Y. Liu, C. T. Santis, A. Spott, S. Srinivasan, E. J. Stanton, and C. Zhang, "Recent advances in silicon photonic integrated circuits," in *Next-Generation Optical Communication: Components, Sub-Systems, and Systems V*, vol. 9774. International Society for Optics and Photonics, 2016, p. 977402.

[160] R. Baets, A. Z. Subramanian, S. Clemmen, B. Kuyken, P. Bienstman, N. Le Thomas, G. Roelkens, D. Van Thourhout, P. Helin, and S. Severi, "Silicon photonics: silicon nitride versus silicon-on-insulator," in *Optical Fiber Communication Conference*. Optical Society of America, 2016, pp. Th3J–1.

[161] W. Bogaerts and L. Chrostowski, "Silicon photonics circuit design: methods, tools and challenges," *Laser & Photonics Reviews*, vol. 12, no. 4, p. 1700237, 2018.

[162] C.-l. Li, X.-h. Jiang, Y. Hsu, G.-h. Chen, C.-w. Chow, and D.-x. Dai, "Ten-channel mode-division-multiplexed silicon photonic integrated circuit with sharp bends," *Frontiers of Information Technology & Electronic Engineering*, vol. 20, no. 4, pp. 498–506, 2019.

[163] D. Dai, "Silicon photonic integrated devices for mode-division-multiplexing," in *2018 23rd Opto-Electronics and Communications Conference (OECC)*. IEEE, 2018, pp. 1–2.

[164] H. Wu, C. Li, L. Song, H.-K. Tsang, J. E. Bowers, and D. Dai, "Ultra-sharp multimode waveguide bends with subwavelength gratings," *Laser & Photonics Reviews*, vol. 13, no. 2, p. 1800119, 2019.

[165] W. Bogaerts, M. Fiers, and P. Dumon, "Design challenges in silicon photonics," *IEEE Journal of Selected Topics in Quantum Electronics*, vol. 20, no. 4, pp. 1–8, 2013.

[166] R. Kirchain and L. Kimerling, "A roadmap for nanophotonics," *Nature Photonics*, vol. 1, no. 6, p. 303, 2007.

[167] D. A. Miller, "Device requirements for optical interconnects to silicon chips," *Proceedings of the IEEE*, vol. 97, no. 7, pp. 1166–1185, 2009.

[168] D. Dai, "Silicon nanophotonic integrated devices for on-chip multiplexing and switching," *Journal of Lightwave Technology*, vol. 35, no. 4, pp. 572–587, 2017.

[169] G.-H. Chen, C.-W. Chow, C.-H. Yeh, C.-W. Peng, P.-C. Guo, J.-F. Tsai, M.-W. Cheng, Y. Tong, and H. K. Tsang, "Mode-division-multiplexing (mdm) of 9.4-tbit/s ofdm signals on silicon-on-insulator (soi) platform," *IEEE Access*, vol. 7, pp. 129 104–129 111, 2019.

[170] Y. Hsu, C.-Y. Chuang, X. Wu, G.-H. Chen, C.-W. Hsu, Y.-C. Chang, C.-W. Chow, J. Chen, Y.-C. Lai, C.-H. Yeh *et al.*, "2.6 tbit/s on-chip optical interconnect supporting mode-division-multiplexing and pam-4 signal," *IEEE Photonics Technology Letters*, vol. 30, no. 11, pp. 1052–1055, 2018.

[171] T. A. Tran, H. D. T. Nguyen, C. D. Truong, H. T. Nguyen, Y. Van Vu, and D. H. Tran, "Three-mode multiplexed device based on tilted-branch bus structure using silicon waveguide," *Photonics and Nanostructures-Fundamentals and Applications*, vol. 35, p. 100709, 2019.

[172] W. Jiang, F. Cheng, J. Xu, and H. Wan, "Compact and low-crosstalk mode (de) multiplexer using a triple plasmonic-dielectric waveguide-based directional coupler," *JOSA B*, vol. 35, no. 10, pp. 2532–2540, 2018.

[173] H. M. Shalaby, "Bi-directional coupler as a mode-division multiplexer/demultiplexer," *Journal of Lightwave Technology*, vol. 34, no. 15, pp. 3633–3640, 2016.

[174] O. M. Nawwar, H. M. Shalaby, and R. K. Pokharel, "Modeling, simulation, and fabrication of bi-directional mode-division multiplexing for silicon-on-insulator platform," *Applied optics*, vol. 57, no. 1, pp. 42–51, 2018.

[175] S. O. Kasap and R. K. Sinha, *Optoelectronics and photonics: principles and practices*. Prentice Hall New Jersey, 2001, vol. 340.

[176] C.-L. Chen, *Foundations for guided-wave optics*. John Wiley & Sons, 2006.

[177] H. M. Shalaby, "Bidirectional mode-division multiplexers with antireflection gratings," *Applied optics*, vol. 57, no. 3, pp. 476–484, 2018.

[178] N. Riesen and J. D. Love, "Tapered velocity mode-selective couplers," *Journal of Lightwave Technology*, vol. 31, no. 13, pp. 2163–2169, 2013.

[179] N. Hanzawa, K. Saitoh, T. Sakamoto, T. Matsui, K. Tsujikawa, T. Uematsu, and F. Yamamoto, "Plc-based four-mode multi/demultiplexer with lp 11 mode rotator on one chip," *Journal of Lightwave Technology*, vol. 33, no. 6, pp. 1161–1165, 2015.

[180] G. Lifante, *Integrated photonics: fundamentals*. John Wiley & Sons, 2003.

[181] C. R. Pollock and M. Lipson, *Integrated photonics*. Springer, 2003, vol. 20, no. 25.

[182] K. Safa, *Optoelectronics and Photonics: Principles and Practices*. Pearson Education India, 2009.

[183] H. Kogelnik and T. Tamir, "Guided-wave optoelectronics," *Springer Series in Electronics and Photonics*, vol. 26, pp. 57–58, 1988.

[184] W. Chang, L. Lu, X. Ren, D. Li, Z. Pan, M. Cheng, D. Liu, and M. Zhang, "Ultra-compact mode (de) multiplexer based on subwavelength asymmetric Y-junction," *Optics Express*, vol. 26, no. 7, pp. 8162–8170, 2018.

[185] K. Mehrabi and A. Zarifkar, "Ultracompact and broadband asymmetric directional-coupler-based mode division (de) multiplexer," *Journal of the Optical Society of America B*, vol. 36, no. 7, pp. 1907–1913, 2019.

[186] ——, "Ultracompact and ultrabroadband mode division multiplexer based on an Au nanocube array assisted directional coupler," *Applied Optics*, vol. 59, no. 5, pp. 1286–1292, 2020.

[187] C. P. Chen, J. B. Driscoll, R. R. Grote, B. Souhan, R. M. Osgood, and K. Bergman, "Mode and polarization multiplexing in a si photonic chip at 40gb/s aggregate data bandwidth," *IEEE Photonics Technology Letters*, vol. 27, no. 1, pp. 22–25, 2014.

[188] A. Yariv and P. Yeh, *Photonics: optical electronics in modern communications*. Oxford Univ., 2006.

[189] M. Minz and R. K. Sonkar, "Numerical design and analysis of a 3-channel grating assisted mode-division (de) multiplexer," *Optik*, vol. 187, pp. 272–277, 2019.

[190] Y. Tan, H. Wu, and D. Dai, "Silicon-based hybrid (de) multiplexer for wavelength-/polarization-division-multiplexing," *Journal of Lightwave Technology*, vol. 36, no. 11, pp. 2051–2058, 2018.

[191] K. Ji, H. Chen, and Y. Zhuang, "A hybrid multiplexer for wavelength/mode-division based on photonic crystals," in *International Conference on Optoelectronics and Microelectronics Technology and Application*, vol. 10244. International Society for Optics and Photonics, 2017, p. 102440B.

[192] L. Han, S. Liang, J. Xu, L. Qiao, H. Zhu, and W. Wang, "Simultaneous wavelength-and mode-division (de) multiplexing for high-capacity on-chip data transmission link," *IEEE Photonics Journal*, vol. 8, no. 2, pp. 1–10, 2016.

[193] O. M. Nawwar, H. M. Shalaby, and R. K. Pokharel, "Photonic crystal-based compact hybrid wdm/mdm (de) multiplexer for soi platforms," *Optics letters*, vol. 43, no. 17, pp. 4176–4179, 2018.

[194] M. Minz and R. K. Sonkar, "Design and analysis of a grating assisted hybrid mode and polarization division (de) multiplexer," *Applied Optics*, vol. 59, no. 3, pp. 785–794, 2020.

[195] ——, “Design of a hybrid mode and wavelength division (de) multiplexer based on contra-directional grating assisted couplers on the soi platform,” *Applied Optics*, vol. 60, no. 9, pp. 2640–2646, 2021.

[196] W. Jiang, J. Miao, and T. Li, “Compact silicon 10-mode multi/demultiplexer for hybrid mode-and polarisation-division multiplexing system,” *Scientific reports*, vol. 9, no. 1, pp. 1–15, 2019.